Measurement of the Inclusive Jet Cross Sections at $\sqrt{s} = 1.8\,TeV$ with the DØ Detector

by

Victor Daniel Elvira

A Dissertation to be presented

In Partial Fulfillment of the Requirements

For the Degree of

Doctor of Philosophy in Physics

Universidad de Buenos Aires
Argentina

1994

STATEMENT BY THE AUTHOR

This document is the English version of the PhD thesis "Medición de la Sección Eficaz Inclusiva de Jets a $\sqrt{s} = 1.8$ GeV con el Detector DØ" to be presented at the Universidad de Buenos Aires. Quotations from this dissertation are allowed, provided that accurate acknowledgement of the source is made.

Acknowledgements

I would not have come to DØ if it were not for my advisor in Buenos Aires, Ricardo Piegaia. I thank him for giving me this opportunity and for his tireless efforts to introduce high energy physics in Argentina.

I am very grateful to all the people without whose time and effort, this work would not have been possible. Thanks to all the members of the DØ collaboration including the physicists, graduate students, computer managers, secretaries, technicians and accelerator staff. I have been very happy during these years at Fermilab and I have gained a lot of experience working with all the DØ members. I thank Peter Grudberg who thoroughly answered each of my questions about the experiment and its software during my early times at DØ working for the vertex chamber group.

I would also like to thank the professors, post–docs and students of the QCD physics group which provided a very friendly and helpful environment for discussion. I am especially grateful to Rich Astur, from whom I have learnt most of what I know about jets; and Harry Weerts, who served as the group convener and always had time to talk about physics analysis. Especially, I want to thank Jerry Blazey who was an active part of the inclusive jet cross section analysis and with whom I shared long hours of work and discussion. His suggestions and advise were essential in the completion of this thesis.

I am also extremely grateful to my advisor at DØ, Gene Fisk, for his guidance and advise over the last years. Actually, he is one of the few DØ physicists who can still do physics without computers.

Finally, I would like to thank my wife Cecilia Gerber for her love and care. Life has been a beautiful experience since we are together.

I dedicate this work to my parents,

Gladys Ferrari and Hector L. Elvira;

to my wife,

Cecilia;

and to our child,

who will be born next year.

Contents

1 Introduction **1**
1.1 The Stuff of Matter . . . 1
1.2 The Standard Model . . . 4
1.3 Jets in Hadron Colliders . . . 7

2 Theoretical Motivation **9**
2.1 The Structure of the Proton . . . 9
2.2 Quantum Chromodynamics . . . 14
2.3 Jet Production in $p\overline{p}$ Collisions . . . 16
2.3.1 Perturbative QCD . . . 17
2.3.2 Non–Perturbative QCD . . . 18
2.4 Jet Cross Sections . . . 19
2.4.1 Jet Kinematics . . . 19
2.4.2 Contributing Processes . . . 20
2.4.3 Inclusive Differential Jet Cross Section . . . 26
2.4.4 Quark Compositeness . . . 28

3 Experimental Design **31**
3.1 The Fermilab Tevatron . . . 31
3.2 The DØ Detector . . . 34
3.2.1 Central Detectors . . . 36
3.2.2 Calorimeters . . . 38
3.2.3 Muon System . . . 45
3.2.4 Trigger and Data Acquisition Systems . . . 46

4 Data Reconstruction and Simulations **51**
4.1 Interaction Vertex Measurement . . . 52
4.2 Jet Reconstruction . . . 53
4.2.1 The Fixed Cone Jet Algorithm . . . 54
4.3 Determination of the Event $\not\!\!E_T$ . . . 58
4.4 Monte Carlo Simulations . . . 58

4.4.1 Event Generators . . . 59
4.4.2 Detector Simulation . . . 59
4.4.3 PJET reconstruction package . . . 61
4.5 Jet Reconstruction Efficiencies . . . 65

5 Sample Selection **69**
5.1 Introduction . . . 69
5.2 Jet Triggers . . . 70
5.3 Luminosity Measurement . . . 72
5.4 Jet Selection . . . 75
5.4.1 Useful Variables for Selecting Jets . . . 79
5.4.2 Distributions of Selection Variables . . . 79
5.4.3 Noisy Areas in $\eta_d - \varphi$ Space . . . 85
5.4.4 Standard Jet Cuts . . . 91
5.5 Noise Rejection . . . 97
5.6 Event Scanning Consistency Check . . . 102

6 Corrections to Jet Quantities **105**
6.1 Jet Trigger Efficiency Determination . . . 105
6.2 Cut Efficiencies . . . 109
6.3 Jet Energy Corrections . . . 120
6.3.1 Energy Scale . . . 121
6.3.2 Energy Resolution . . . 127
6.4 Jet Position Corrections . . . 134
6.4.1 Reconstructed η Bias . . . 134
6.4.2 η Resolution . . . 137
6.5 Smearing Correction to the Jet Cross Sections . . . 140
6.5.1 Smeared Distributions . . . 140
6.5.2 The Unsmearing Procedure . . . 143
6.5.3 Monte Carlo Simulation . . . 144
6.5.4 Results . . . 146

7 Results and Conclusion **151**
7.1 Inclusive Jet Cross Sections . . . 151
7.1.1 Experimental Determination of $< d^2\sigma/dE_T d\eta >$ . . . 151
7.1.2 Statistical and Systematic Uncertainties . . . 154
7.1.3 Results . . . 155
7.1.4 Comparison with QCD Predictions . . . 166
7.2 Conclusion . . . 169

List of Figures

2.1 Deep inelastic electron–proton scattering. 11
2.2 Examples of quark and gluon momentum probability densities as a function of x. 13
2.3 quark–quark–gluon vertex. 14
2.4 Three and four gluon vertices. 15
2.5 Description of the jet production process in a hadron collider. . . . 17
2.6 Examples of $2 \to 2$ subprocesses contributing to second order in α_s. 23
2.7 Two–jet event observed in the DØ calorimeter. 24
2.8 Examples of $2 \to 3$ subprocesses contributing to third order in α_s. 24
2.9 Three–jet event observed in the DØ calorimeter. 25
2.10 Inclusive differential jet cross section ($|\eta| < 0.9$) using the PAPAGENO generator (LO) with different values of Λ_c. 29

3.1 Overhead view of the Fermilab complex. 32
3.2 The DØ detector. 35
3.3 $r - z$ view of DØ Central Detectors. 36
3.4 General view of DØ calorimeters. 39
3.5 Calorimeters and muon system interaction lengths as a function of θ. 40
3.6 Diagram of a Calorimeter unit cell. 41
3.7 Side view of calorimeter modules, intercryostat detectors and massless gaps. 43
3.8 Elevation view of DØ Detector including the muon chambers . . . 45
3.9 Side view of calorimeter trigger towers. 48

4.1 Calorimeter energy distributions for monoenergetic incident electrons (Test Beam data). 63
4.2 Calorimeter energy distributions for monoenergetic incident hadrons (Test Beam data). 64
4.3 Jet finding efficiency for the $R = 0.7$ fixed cone algorithm with (HERWIG simulation). 66
4.4 Biases in the reconstructed η and φ as a function of the jet pseudo–rapidity (HERWIG events). 68

5.1 Integrated luminosity delivered and recorded by DØ during run 1A. 74
5.2 Highest E_T three–jet event observed at DØduring run $1A$. The two leading jets have E_T's of the order of 450 GeV. 77
5.3 Cosmic showers penetrate the detector and deposit large amounts of energy in the calorimeters. 77
5.4 The main ring accelerator passes through the CH modules of the DØ calorimeters. Energy is deposited in the whole area during a main ring event. 78
5.5 The signature of a main ring event is clearly represented in this event display. Large amounts of hadronic energy is deposited along the main ring direction. 78
5.6 Jet EMF distributions for different E_T and η_d bins. 82
5.7 Jet HCF distributions for different E_T and η_d bins. 83
5.8 Jet CHF distributions for different E_T and η_d bins. 84
5.9 Fake jet distributions from noise runs. 85
5.10 $\eta - \varphi$ distributions of jets with $E_T \in [25, 35]$ GeV and $E_T \in [35, 50]$ GeV. 87
5.11 $\eta - \varphi$ distributions of jets with $E_T \in [50, 75]$ GeV and $E_T \in [75, 100]$ GeV. 88
5.12 $\eta - \varphi$ distributions of jets with $E_T \in [100, 150]$ GeV and $E_T \in [150, 200]$ GeV. 89
5.13 $\eta - \varphi$ distributions of jets with $E_T \in [200, 250]$ GeV and $E_T > 250$ GeV. 90
5.14 $\eta_d - \varphi$ scatter plot of jets with $E_T \in [200, 250]$ GeV after the standard cuts are applied. A group of fake jets survives the cuts in regions 8 and 9. 92
5.15 Typical multijet event that populates regions 8 and 9. Two neighbor noisy cells in the massless gaps overlap with a real low E_T jet. Sometimes, the object passes the three standard cuts. A group of noisy EMF cells fakes another jet that populates region 9. The tallest column represents the event $\not\!\!E_T$ 93
5.16 A fine hadronic noisy cell superimposed on a low E_T jet forms a jet type object that populates region 4. 95
5.17 (a)–E_T of the leading jet as a function of $1/R_{MTE}$. (b)– $1/R_{MTE}$ distribution for $E_T^{jet} \in [45, 50]$ GeV. (c)– $\eta_d - \varphi$ distribution for jets in the range $E_T \in [200, 250]$ after the R_{MTE} cut is applied. 96
5.18 (a),(b),(c)–Jet occupancy, x_8, and significant deviation, λ_8, in region 8. Plots (d),(e),(f) correspond to a clean control region $8C$ with the same average x. 100

5.19 Inclusive jet cross section ratios R for the CT, IC and FW pseudo-rapidity regions. The cross section in the numerator is calculated with a reduced sample of clean runs. The denominator uses the whole sample. The jet quality cuts are applied in both cases. . . . 101

6.1 Efficiencies of the jet triggers as a function of E_T and η_d for the central, intercryostat and forward regions. 108

6.2 Illustration of the method used to calculate the EMF cut efficiency. The histograms in dashed line correspond to a sample deprived from the noisy regions. The R_{MTE} cut is added to obtain the distributions in solid line. The arrows point to the cut thresholds and the dots in the bottom plots indicate the limit between the gaussian fit and the linear parametrization. 112

6.3 Illustration of the method used to calculate the HCF and R_{MTE} cut efficiencies. The histograms in dashed line correspond to a sample deprived from the noisy regions. The R_{MTE} cut is added to obtain the HCF distribution in solid line. A quadratic function is selected to fit the true HCF distribution and a gaussian is chosen in the case of the $1/R_{MTE}$ distribution. 114

6.4 Combined Efficiencies of the standard jet cuts, ε_{STD} as a function of jet E_T for the three detector regions. CT: $0 < |\eta_d| < 1$, IC: $1 < |\eta_d| < 1.6$ and FW: $1.6 < |\eta_d| < 3$. 119

6.5 Dependence of the energy scale on the jet electromagnetic fraction (EMF) and η_d. The response is better for jets with high and low EMF and gets worse in the forward η_d region due to out of cone effects. The band within dashed lines represents the energy scale uncertainty. 125

6.6 Energy Scale correction factor as a function of E_T for jets with $\eta_d = 0$ and $\eta_d = 2.5$. The band within dashed lines represents the energy scale uncertainty. 126

6.7 Parametrization of the fractional transverse energy resolution as a function of the scale corrected jet energy. 131

6.8 Parametrization of the fractional transverse energy resolution in the CT and IC regions as a function of the scale corrected jet E_T . The dark circles are obtained from the $jet - jet$ sample and the open circles are associated with $\gamma - jet$ events. The fit includes both sets of measurements. 132

6.9 Parametrization of the fractional transverse energy resolution in the forward regions as a function of the scale corrected jet E_T . The dark circles are obtained from the $jet - jet$ sample and the open circles are associated with $\gamma - jet$ events. The fit includes both sets of measurements. 133

6.10 HERWIG monte carlo simulation of the η bias as a function of the jet η_d^{reco} and energy (in GeV). $< \rho(E, \eta_d) >$ is plotted in solid line. As a consistency check, $< \eta_d^{parton} - \eta_d^{cor} >$ is plotted in dashed line after the bias correction is applied. 138

6.11 HERWIG simulation of the jet η resolution. $\eta_d^{parton} - \eta_d^{cor}$ distributions are shown in solid line and $\eta_d^{parton} - \eta_d^{reco}$ in dashed line. . . . 139

6.12 $\sigma_\eta(E, \eta_d)$ as a function of the parton jet energy using a HERWIG simulation. 139

6.13 R_{sme} is the ratio between the jet cross section smeared both in η and E_T and the jet cross section smeared in E_T only. The smearing effect due to η resolution is less than 2.5% in the very forward region ($2.5 < |\eta| < 3$). The plot corresponds to a Monte Carlo simulation based on JETRAD. The effect is negligible in lower pseudo–rapidity regions since the η resolution is better there. 142

6.14 The histograms correspond to jet E_T distributions in photon–jet events. The photon is required to have E_T within a narrow bin to simulate monoenergetic photons. The jet distribution is well described by a gaussian function which is used as an approximation to the smearing function. 142

6.15 Monte Carlo simulation study using JETRAD. Top: comparison between the true smearing effect R_{res}^{true} and the correction R_{res}^{uns} to the cross section obtained with the unsmearing procedure. Bottom: hypothetical change in the smearing correction due to statistical fluctuations of the data. 147

6.16 Solid lines: smeared hypothesis, $f(E_T', A, B, C, D)$, fit to the corrected jet cross sections measured in different η regions. The data points are plotted in circles 149

6.17 Corrections, R_{sme}, for E_T resolution smearing applied to jet cross sections measured in different η regions. 150

7.1 DØ inclusive double differential jet cross section as a function of jet E_T in the CT1 and CT2 regions ($|\eta| < 0.5$ and $0.5 < |\eta| < 1$). The solid bars are the statistical errors and the dashed bars are the total systematic errors. 163

7.2 DØ inclusive double differential jet cross section as a function of jet E_T in the IC1 and IC2 regions ($1 < |\eta| < 1.5$ and $1.5 < |\eta| < 2$). The solid bars are the statistical errors and the dashed bars are the total systematic errors. 164
7.3 DØ inclusive double differential jet cross section as a function of jet E_T in the FW1 and FW2 regions ($2 < |\eta| < 2.5$ and $2.5 < |\eta| < 3$). The solid bars are the statistical errors and the dashed bars are the total systematic errors. 165
7.4 Dependence of the EKS QCD prediction of the inclusive jet cross sections in the LO and NLO approximations on the renormalization scale μ. 167
7.5 Ratios of the EKS predictions of the inclusive jet cross sections in the NLO approximation using different PDF sets. All the sets are compared to the best CTEQ fit, CTEQ2M. 168
7.6 DØ inclusive jet cross sections as a function of the jet E_T compared with EKS QCD(NLO) predictions using CTEQ2M distribution functions. 171
7.7 DØ inclusive jet cross sections as a function of the jet E_T compared with EKS QCD(NLO) predictions using CTEQ2M distribution functions. 172
7.8 DØ inclusive jet cross sections as a function of the jet E_T compared with EKS QCD(NLO) predictions using CTEQ2M distribution functions. 173
7.9 Ratios between DØ inclusive jet cross sections and EKS QCD(NLO) predictions using CTEQ2M distribution functions. 174
7.10 Ratios between DØ inclusive jet cross sections and EKS QCD(NLO) predictions using CTEQ2M distribution functions. 175
7.11 Ratios between DØ inclusive jet cross sections and EKS QCD(NLO) predictions using CTEQ2M distribution functions. 176

List of Tables

1.1 The three generations of quarks and leptons according to the Standard Model 5
1.2 Gauge bosons associated to the fundamental interactions 6

2.1 List of all possible $2 \to 2$ subprocesses in QCD. q and $q\prime$ denote different quark flavors. 21
2.2 List of all possible $2 \to 3$ subprocesses in QCD. q and $q\prime$ denote different flavors of quark. 21

5.1 Description of the jet triggers. The z–vertex position is given in cm and E_T thresholds in GeV. The z–vertex cut is not always applied for JET_HIGH. 72
5.2 Total trigger effective luminosities of the sample used in the cross section measurement. 75
5.3 Noisy calorimeter regions and their positions in $\eta_d - \varphi$ space. . . . 86
5.4 Events with jets that passed the standard cuts, with E_T's above a threshold ε, were scanned as a consistency check for the noise rejection and good jet efficiency studies. One good event failed the R_{MTE} cut and two bad events passed the cut. 102

6.1 Standard cuts efficiencies as a function of jet E_T for the CT region ($0 < |\eta_d| < 1$). The bins at high E_T were manipulated to study statistical fluctuations. 116
6.2 Standard cuts efficiencies as a function of the jet E_T for the IC region ($1 < |\eta_d| < 1.6$). The bins at high E_T were manipulated to study statistical fluctuations. 117
6.3 Standard cuts percent efficiencies as a function of the jet E_T for the FW region ($1.6 < |\eta_d| < 3$). The bins at high E_T were manipulated to study statistical fluctuations. 117
6.4 R_{MTE} cut efficiencies as a function of the leading jet E_T. 118
6.5 combined efficiencies of the standard jet cuts, as a function of jet E_T for the three detector regions. 118

6.6 Parametrization of the fractional transverse energy resolution as a function of the scale corrected jet energy. 129
6.7 Parametrization of the fractional transverse energy resolution as a function of the scale corrected jet E_T . It includes low E_T $\gamma - jet$ data points. 130
6.8 Parametrization of the η bias as a function of reconstructed η_d for different energy bins. 136
6.9 Parametrization of the jet η resolution as a function of parton jet energy for different η_d bins. 139
6.10 Parametrizations of the inclusive jet cross section hypotheses as a function of the corrected jet E_T for different η_d regions. 148

7.1 Kinematic range covered by the DØ measurement of the inclusive jet cross section. 152
7.2 DØ inclusive double differential jet cross section as a function of jet E_T in the CT1 region ($|\eta| < 0.5$). The jet E_T is in GeV and the cross section in (nb/GeV). The E_T spectrum was divided into 5, 10, 20 and 40 GeV bins as E_T increases. 157
7.3 DØ inclusive double differential jet cross section as a function of jet E_T in the CT2 η region ($0.5 < |\eta| < 1$).The jet E_T is in GeV and the cross section in (nb/GeV). The E_T spectrum was divided into 5, 10, 20 and 40 GeV bins as E_T increases. 158
7.4 DØ inclusive double differential jet cross section as a function of jet E_T in the IC1 η region ($1 < |\eta| < 1.5$). The jet E_T is in GeV and the cross section in (nb/GeV). The E_T spectrum was divided into 5, 10, 20 and 40 GeV bins as E_T increases. 159
7.5 DØ inclusive double differential jet cross section as a function of jet E_T in the IC2 η region ($1.5 < |\eta| < 2$). The jet E_T is in GeV and the cross section in (nb/GeV). The E_T spectrum was divided into 5, 10, 20 and 40 GeV bins as E_T increases. 160
7.6 DØ inclusive double differential jet cross section as a function of jet E_T in the FW1 η region ($2 < |\eta| < 2.5$). The jet E_T is in GeV and the cross section in (nb/GeV). The E_T spectrum was divided into 5, 10 and 20 GeV bins as E_T increases. 161
7.7 DØ inclusive double differential jet cross section as a function of jet E_T in the FW2 η region ($2.5 < |\eta| < 3$). The jet E_T is in GeV and the cross section in (nb/GeV). The E_T spectrum was divided into 5 and 10 GeV bins as E_T increases. 162

Chapter 1

Introduction

1.1 The Stuff of Matter

"The world is made of earth, water, fire and air. All forms of matter are obtained by condensing or rarefying air". This is the theory that Anaximenes of Miletus came up with 26 centuries ago to explain the nature of matter. It was also in the Ancient Greece where Democritus suggested that matter was composed of very small, identical and indivisible particles he called **atoms.**These ideas are usually taken as the first rudimentary attempts to address the elusive question of the nature of matter before mankind had given birth to the concept of experimental science.

With the advent of modern science, elementary particle physics has made dramatic progress in the search for new particles and the understanding of the interaction processes involved. The discovery of the **electron** by J. J.Thompson in 1897 triggered the first atomic models. Thompson suggested that atoms, which were known to be heavy and electrically neutral, were made of electrons suspended in a heavy, positively charged paste. Rutherford, by means of his famous scattering experiment with α particles, demonstrated later that the positive charge was

concentrated in a very small, heavy nucleus in the center of the atom. He called it **proton** in the case of hydrogen. In 1914, Niels Bohr proposed a scheme for the hydrogen atom which consisted of a single electron moving around the proton in a circular orbit. This model predicted correctly the spectrum of emission of hydrogen, but could not explain why heavy atoms weighed so much or the fact that the electron did not collapse onto the proton due to electromagnetic radiation. The problem of the stability of the electron orbit motivated the development of the quantum theory. The lack of understanding regarding the weight of heavy atoms was removed when Chadwick discovered the **neutron** in 1932.

During the same period of time, Planck and Einstein introduced the idea of the quantization of the electromagnetic field: Planck with his explanation of the black body spectrum in 1900 and Einstein with his photoelectric effect model in 1906. The light quanta, later called the **photon,** would be the mediator for all electromagnetic interactions. The union of Einstein's special relativity and the quantum theory lead to the Dirac equation (1927) which predicted the existence of the antiparticles. In 1931, Anderson discovered the **positron,** the electron's antiparticle.

In the early 1930's, physicists had simple and satisfying answers to the problem of the nature of matter. However, there were some problems the existing models could not explain. The only known forces in nature were the gravitational force and the electromagnetic force. This raised an uncomfortable question: what held the nucleus together? The answer involved the discovery of a third fundamental interaction called the strong force.

Yukawa proposed the first significant theory of the strong force in 1934. Protons and neutrons were attracted to each other by a short range field whose

associated quanta were known as the **mesons** (middle-weight). Cosmic rays experiments carried out in 1937 and 1946 identified Yukawa's particle, called the **pion,** and a light impostor, the **muon.** The muon was incorporated to the **lepton** family (light-weight) as it behaved in all ways like a heavier version of the electron. In the mid-fifties, Cowan and Reines found the **neutrino,** a very light and weakly interacting particle predicted by Pauli two decades before to rescue the energy conservation law in the case of beta decays. During the period between 1947 and 1960, a large number of new mesons and **baryons** (heavy-weight) were discovered as the first modern particle accelerators were built in Berkeley and Brookhaven.

In 1961, Murray Gell–Mann introduced the "eightfold way"[1], the elementary particle analog to Mendeleev's periodic table. Baryons and mesons were arranged into weird geometrical patterns, according to their charge and strangeness, a new quantum number conserved in every case but in weak interactions. Even though the eightfold way was very successful classifying and predicting particles, the underlying reason for these curious patterns was not known. But soon after, in 1964, Gell–Mann and Zweig[2] proposed that all **hadrons** (baryons and mesons) were in fact composed of even more elementary constituents they called quarks. The existence of three lumps inside the proton was determined at SLAC[1] and CERN[2] during the late sixties and early seventies. In 1974, S.Ting (Brookhaven) and B.Richter (SLAC) observed a very heavy and longlived meson they called J/ψ[3, 4]. Three years later at FNAL, a group lead by Leon Lederman discovered the Upsilon meson (Υ)[5], ten times heavier than the J/ψ. The best explanation

[1]Stanford Linear Accelerator Center.
[2]European Nuclear Research Center, Geneva, Switzerland.

to the existence of these two new particles was provided by the quark model.

During the sixties, Glashow, Weinberg and Salam presented the electroweak theory and predicted the existence of three mediators ($W^{\pm}$ and Z) for the forth force, the weak interaction[6]. In 1983, Carlo Rubbia's group announced the discovery of these three intermediate vector bosons from evidence obtained in experiments at CERN's $p\overline{p}$ collider[7, 8].

The twentieth century has brought a succession of brilliant insights and major achievements in the understanding of the world of elementary particles and their interactions. Once again: what is the world made of?

1.2 The Standard Model

The **Standard Model** [9, 10, 11, 12] is the best attempt to answer the question. All matter is composed of **quarks** (q) and **leptons** (l). Quarks are spin $\frac{1}{2}$ fermions with fractional electric charge $+\frac{2}{3}$e or $-\frac{1}{3}$e. All baryons, like protons and neutrons are made of three quarks. Mesons are built from a quark–antiquark pair ($q\overline{q}$). Leptons, like the electron and the neutrino carry integral electric charge. There are six flavors of quarks: up (u), down (d), strange (s), charm (c), bottom (b), and top (t); and six types of leptons: electron (e^-), muon (μ^-), tau (τ^-), and their associated neutrinos (ν_e, ν_μ, ν_τ). For example, the proton and the neutron consist of a combination of quarks like:

$$p = (uud), \quad n = (ddu)$$

and the pions are $q\overline{q}$ pairs such as:

$$\pi^+ = (u\overline{d}), \quad \pi^- = (d\overline{u}), \quad \pi^\circ = (\tfrac{u\overline{u}-d\overline{d}}{\sqrt{2}}) \quad .$$

Quarks and leptons are grouped into three generations or families according to their properties as shown in Table 1.1.

Table 1.1: The three generations of quarks and leptons according to the Standard Model

	Name (Type)	Symbol	Charge (e)	Mass (GeV)
First Generation	up (q)	u	$\frac{2}{3}$	4×10^{-3}
	down (q)	d	$-\frac{1}{3}$	7×10^{-3}
	e–neutrino (l)	ν_e	0	$< 1.7 \times 10^{-8}$
	electron (l)	e	-1	5.1×10^{-4}
Second Generation	charm (q)	c	$\frac{2}{3}$	1.5
	strange (q)	s	$-\frac{1}{3}$	0.2
	μ–neutrino (l)	ν_μ	0	$< 2.7 \times 10^{-4}$
	muon (l)	μ	-1	1.06×10^{-1}
Third Generation	Top (q)	t	$\frac{2}{3}$	> 131
	Bottom (q)	b	$-\frac{1}{3}$	5
	τ–neutrino (l)	ν_τ	0	$< 3.5 \times 10^{-2}$
	Tau (l)	τ	-1	1.78

The universe appears to be governed by four kinds of forces: electromagnetic, weak, strong and gravitational. The electric charge is the source of the electromagnetic interaction which generates long range attractive or repulsive forces between electrically charged particles. Weak interactions account for processes involving change of flavor. Strong forces act within a very short distance range and are responsible for binding quarks together to make hadrons. Each quark carries color, the strong analog of the electric charge. Color is a figurative description that stands for strong charge. Quarks may carry three different strong charges; they come in blue, red or green. Gravitational forces appear between massive particles. Typical time scales for the different processes are 10^{-23}s (strong), 10^{-20}s (electromagnetic), 10^{-8}s (weak). Gravitational effects are negligible for nuclear and sub–nuclear particles and they are by far the weakest forces.

The mediators or **gauge bosons** complete the elementary particle picture

drawn by the Standard Model. The forces are transmitted by fields or particles which are equivalent concepts in relativistic quantum theory. Quantum Electrodynamics (QED) is a renormalizable $U(1)$ local gauge invariant theory for electromagnetic interactions. The gauge boson associated with QED is the spin 1, massless photon. Weak forces are transmitted by massive spin 1 $W^{\pm}$ and Z bosons according to the $SU(2)_L \times U(1)$ invariant gauge theory proposed by Glashow, Weinberg and Salam for electroweak interactions. Gravity might be transmitted by spin 2 gravitons. Quantum Chromodynamics (QCD) is based on the SU(3) symmetry group and describes the strong interactions. The associated mediators are eight spin 1 gauge bosons called gluons. The fundamental forces and mediator bosons are displayed in Table 1.2.

Table 1.2: Gauge bosons associated to the fundamental interactions

Force	Boson	Symbol	charge (e)	spin	Mass (GeV)
Strong	gluon	g	0	1	0
Electromagnetic	photon	γ	0	1	$< 3 \times 10^{-36}$
Weak	W–boson	$W^{\pm}$	± 1	1	81
	Z–boson	Z°	0	1	91
Gravitational	graviton	G	0	2	0

The set of elementary particles predicted by the Standard Model is completed with the anti–particles associated with each type of quark and lepton. In addition, there is at least one Higgs scalar boson predicted by the electroweak theory. All these particles except the top quark and the Higgs boson have been observed experimentally. Recently, the CDF collaboration at Fermilab announced evidence of top production[13].

The Standard Model is a gauge theory based on an $SU(3) \times SU(2) \times U(1)$

symmetry, constructed as a combination of QCD and the Electroweak theory. It is today's best approach to the description of the nature of matter. New different theories are currently under consideration in an attempt to answer the open questions. The Grand Unified Theories (GUTS) postulate a larger symmetry group G to describe the 4 interactions which would be the same at energies of the order of 10^{15} eV. GUT models predict larger families of quarks and leptons and also more gauge bosons. Supersymmetry (SUSY) is a theory that goes beyond the GUT unification scheme and postulates that each particle has its associated superpartner. It also promises to include gravity into the unified model. Other theories suggest that the elementary particles described by the Standard Model may be composites, made of more basic particles called preons.

1.3 Jets in Hadron Colliders

The search for jets in hadron colliders during the seventies and early eighties is described in detail in reference[14]. Soft interactions represent the largest fraction of the total inelastic cross section in hadron colliders. Hard collision processes, which involve an elastic interaction between the underlying partons (q, $\overline{q}$ or g), occur at a lower rate and are described by perturbative QCD. In leading order QCD, these kind of events result in the production of two highly collimated collections of hadrons, each having a total four–momentum equal to that of the parent parton. These jets of hadrons were first observed in 1972 at the CERN Intersecting Storage Rings (ISR) in pp interactions at a center of mass energy (CM energy) between 30 and 62 GeV [15, 16, 17]. However, it was not clear during the seventies whether the final state hadrons experimentally observed in hadron collisions were to be associated with jets. In fact, several experiments carried out at CERN and

FNAL in 1981 – 1982 using a full azimuthal calorimeter coverage concluded that these final states consisted mostly of many low energy particles with a symmetric azimuthal distribution[18, 19]. The results were in sharp contrast with the case of e^-e^+ annihilation into hadrons, where jets were obvious at CM energies above 10 GeV.

It was not until 1982 that jets were produced copiously in the $p\overline{p}$ accelerator at CERN as the CM energy increased up to 630 GeV [20]. The first hadron collider experimental studies on jet properties and tests of QCD were done by the UA1 and UA2 collaborations at CERN[21, 22, 23]. Since the Tevatron started to operate at FNAL in 1985, the Collider Detector at Fermilab (CDF) has produced new and more accurate jet measurements by taking advantage of the 1.8 GeV available at the center of mass. CDF has measured the inclusive jet cross section for jet transverse energies as large as 400 GeV and has established a lower limit to the scale of quark compositeness of 1.4 GeV [24, 25].

DØ is a collider detector constructed at Fermilab. It is especially suited to jet measurements due to its excellent calorimetry, which is finely segmented and provides good containment and hermeticity. The ability to trigger jets as close to the beam pipe as 5° enables DØ to obtain, for the first time, a measurement of the jet cross section at low angles. The succeeding pages contain a brief introduction to the underlying theory involved in the jet cross section measurement. A description of the Tevatron and the DØ detector is followed by a detailed discussion on the process of data selection and jet measurement. At the end, the results are presented and compared to theoretical predictions.

Chapter 2

Theoretical Motivation

The experimental determination of the jet cross section is one of the most important tests of QCD. In addition to verification of the existing QCD predictions, it is used to test the validity of different sets of parton distribution functions and search for quark compositeness. At the Fermilab Tevatron, the DØ detector is able to perform a large variety of measurements involving jets produced in $p\overline{p}$ collisions at a CM energy of 1.8 GeV. Recently, the next–to–leading order (NLO) theoretical calculation of the inclusive jet cross section, $\sigma(p\overline{p}) \rightarrow jet + X$, have become available, which adds particular interest to this measurement at the Tevatron.

This chapter is based on references[9, 10, 11, 12]. It begins with a description of the structure of the proton and a brief introduction to QCD. The rest is a discussion of jet production resulting from a hard parton–parton elastic scattering. Theoretical calculations of the Inclusive Jet Cross Section are also discussed.

2.1 The Structure of the Proton

The simplest picture of the proton is a composite structure made of two u quarks and one d quark which are tightly bound by the strong force. The constituents of the proton are generically called partons. Evidence for partons was first observed

in deep inelastic electron–proton scattering experiments. In the $ep \to eX$ process, illustrated in Figure 2.1, the exchange of an energetic virtual photon or Z° with a target parton causes a large momentum transfer collision which results in an outgoing quark. In a frame where the momentum of the proton is very large compared to the masses of the interacting particles, the relativistic time dilation slows down the rate at which partons interact with one another. As a consequence, the quark is essentially a free particle during the short time of the interaction. This statement is the basis of **the parton model** and only applies when the four momentum transfer (q) is very large. In this limit, the proton structure functions W_1 and W_2 are independent of $Q^2 = -q^2$ at a given value of the energy transfer $\nu = E_e - E'_e$. Then,

$$\begin{aligned} MW_1(\nu, Q^2) &\to F_1(\omega) \\ \nu W_2(\nu, Q^2) &\to F_2(\omega)\,, \end{aligned} \tag{2.1}$$

where M is the mass of the proton, p its momentum and

$$\omega \equiv \frac{2q \cdot p}{Q^2} = \frac{2M\nu}{Q^2}\,.$$

The equations above may be rewritten as a function of $x = 1/\omega$, the fraction of the proton momentum carried by the interacting parton. Then,

$$\begin{aligned} F_2(x) &= \sum_i e_i^2 x f_i(x) \\ F_1(x) &= \frac{1}{2x} F_2(x)\,, \end{aligned} \tag{2.2}$$

where $f_i(x)$ are the **parton distribution functions,** defined as the probability density associated with a struck parton i which carries a fraction x of the proton's momentum and the sum is over all the different types of quarks. The inelastic

structure functions $F_{1,2}$ in equations 2.2 depend only on x and satisfy **Bjorken scaling,** i.e. Q^2 independence.

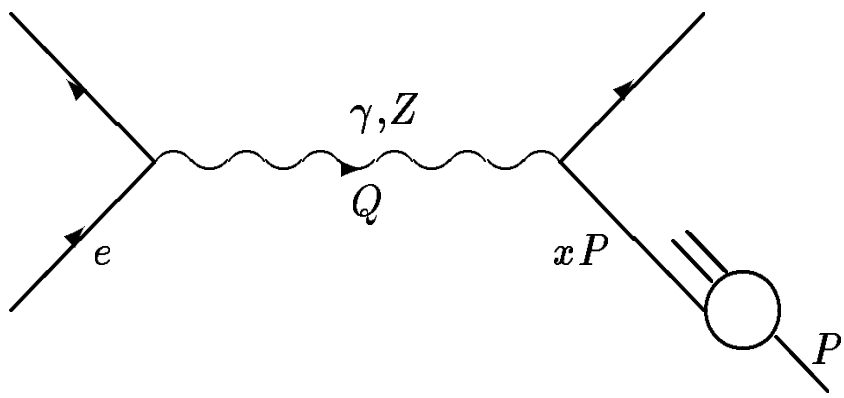

Figure 2.1: Deep inelastic electron–proton scattering.

The quarks interact strongly inside the proton exchanging gluons which may create $q\overline{q}$ pairs. Three valence quarks u_v, u_v and d_v form the proton together with many $q\overline{q}$ pairs known as sea quarks and numerous gluons. The net number of each kind of quark must satisfy:

$$\begin{aligned}
\int_0^1 [u(x) - \overline{u}(x)]dx &= 2 \\
\int_0^1 [d(x) - \overline{d}(x)]dx &= 1 \\
\int_0^1 [h(x) - \overline{h}(x)]dx &= 0\,,
\end{aligned} \tag{2.3}$$

where $u(x)$ and $d(x)$ are the parton distribution functions for quarks u and d, and $h(x)$ is a generic name for the functions associated with the sea quarks c, s, t or b. Charge and quark number conservation within the proton is described in Equations 2.3. The quark distributions are empirically determined from data on

electron and neutrino deep inelastic scattering (DIS) in the Q^2 range $5 < Q^2 < 800$ (GeV/c)^2. The total fraction of the proton momentum carried by the quarks and anti–quarks, as determined by comparison of deep inelastic scattering cross sections from muon and neutrino scattering show:

$$\int_0^1 dx \;\; x[u(x) + \overline{u}(x) + d(x) + \overline{d}(x) + s(x) + \overline{s}(x)] \approx 0.5\,.$$

Since contributions from other flavors are small, the remaining 50% must be carried by neutral constituents, the gluons. The gluon distribution functions can be experimentally obtained from processes such as $pp \to \gamma + X$ and $pp \to \psi X$ or by considering higher order QCD processes in which virtual gluons contribute to DIS. Figure 2.2 shows some examples of quark and gluon distributions as a function of x for two different values of Q [26, 27, 28].

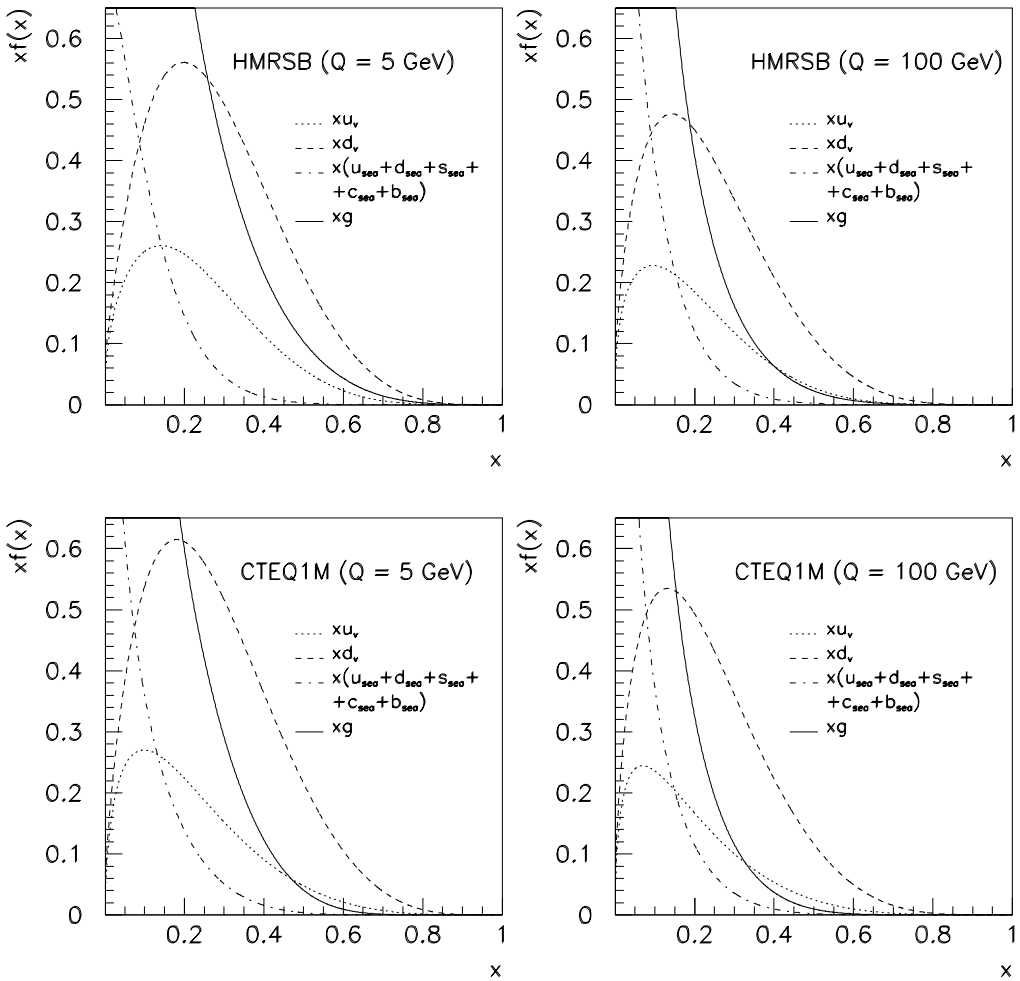

Figure 2.2: Examples of quark and gluon momentum probability densities as a function of x.

2.2 Quantum Chromodynamics

Quantum Chromodynamics (QCD) describes the interactions of colored particles. Quarks and gluons carry color. Therefore, they experience and transmit strong forces. The strength of the chromodynamic interaction is set by the strong coupling constant α_s. Each quark has one of three possible colors, red (r), blue (b) or green (g). Anti–quarks come in anti–red ($\overline{r}$), anti–blue ($\overline{b}$) and anti–green ($\overline{g}$). The gluon, boson mediator in QCD, also carries color charge unlike its analog in Quantum Electrodynamics, the photon, which does not carry electric charge. In fact, the gluon carries two color labels, one color and one anti–color. Thus, color is conserved in a typical quark–quark–gluon vertex such as the one in Figure 2.3.

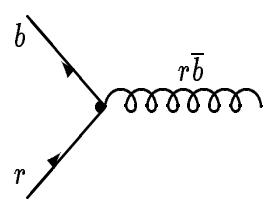

Figure 2.3: quark–quark–gluon vertex.

In terms of color $SU(3)$ symmetry, there are nine possible states for gluons. These states constitute a "color octet":

$$\begin{array}{rr}
(r\overline{b}+b\overline{r})/\sqrt{2} & -i(r\overline{g}-g\overline{r})/\sqrt{2} \\
-i(r\overline{b}-b\overline{r})/\sqrt{2} & (b\overline{g}+b\overline{g})/\sqrt{2} \\
(r\overline{r}-b\overline{b})/\sqrt{2} & -i(b\overline{g}-g\overline{b})/\sqrt{2} \\
(r\overline{g}+g\overline{r})/\sqrt{2} & (r\overline{r}+b\overline{b}-2g\overline{g})/\sqrt{6}
\end{array}$$

and a "color singlet":

$$(r\overline{r}+b\overline{b}+g\overline{g})/\sqrt{3}\,.$$

The color singlet gluon, which would occur as a free particle, does not exist. The other eight types can couple directly to each other forming three or four gluon vertices like those shown in Figure 2.4.

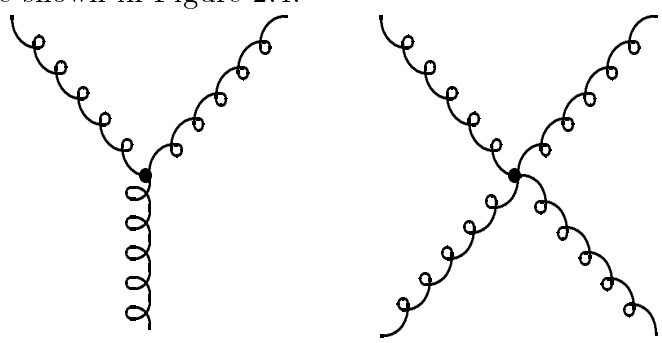

Figure 2.4: Three and four gluon vertices.

As a consequence of these couplings neither quarks nor gluons can appear as free particles. In other words, the potential energy required to separate two quarks increases linearly with their distance, making the color ionization potential infinite. This principle is known as **color confinement** and establishes that only color singlet (colorless) states are allowed as physical hadrons.

Due to vacuum polarization, the QED coupling constant α depends on the Q^2 of the boson mediator. The more energetic the virtual photon is, the stronger the interaction as the effective charge increases. The opposite behaviour is observed in QCD interactions. The QCD coupling constant is also a "running constant" or **coupling function** $\alpha_s(Q^2)$**.** However, the strength of the strong interaction increases at large distances. Moreover, $\alpha_s(Q^2)$ decreases with increasing Q^2 and becomes small for short–distance interactions. This behavior is known as **asymptotic freedom** and makes QCD a perturbative theory at large values of Q^2. The theory is also renormalizable meaning that the observables can be calculated in terms of measured quantities to avoid divergencies in the calculations. Then, in

the one loop approximation, $\alpha_s(Q)$ becomes:

$$\alpha_s(Q) = \frac{12\pi}{(33 - 2n_f)log(Q^2/\Lambda^2)}$$

with:

$$\Lambda^2 = \mu^2 exp\left[\frac{-12\pi}{(33 - 2n_f)\alpha_s(\mu^2)}\right],$$

where n_f is the number of existing quark flavors and μ is the renormalization scale.

In the previous section, a very simple picture of the proton structure was presented. Within the parton model, the parton distribution functions satisfy Bjorken scaling, i.e. Q^2 independence. However, when gluon emission is included in the theory, Bjorken scaling is violated. The reason is that the probability of finding a quark at high x decreases with increasing Q^2 because high momentum quarks lose momentum by radiating gluons. The evolution of the quark distribution functions with Q^2 for a fixed x is described by the **Altarelli–Parisi** equations[9]. It was experimentally determined that the distribution functions increase with increasing Q^2 below $x \approx 0.2$ and decrease above that threshold.

2.3 Jet Production in $p\overline{p}$ Collisions

Jet production is a common process in hadron collisions with a CM energy greater than 10 GeV. The Tevatron produces deep inelastic $p\overline{p}$ collisions which uncover the composite structure of the proton/anti–proton. In other words, the interaction is an elastic parton–parton scattering. The whole process from the hard scattering to jet production is described by QCD.

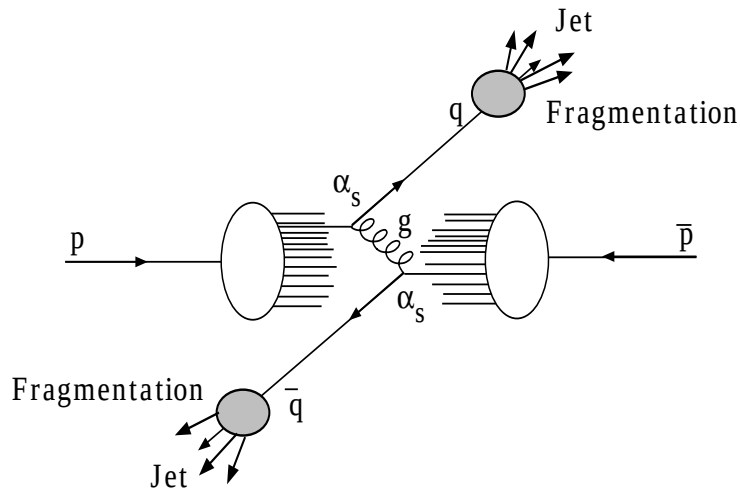

Figure 2.5: Description of the jet production process in a hadron collider.

2.3.1 Perturbative QCD

Colored quarks and gluons can be regarded as free during a **hard collision.** Therefore, α_s is small and QCD becomes a perturbative theory. At early times after the hard collision, which correspond to distances much shorter than the typical size of a hadron, α_s increases and the outgoing partons emit gluons and gluons split into $q\overline{q}$ pairs. This process is known as **parton showering.**

The perturbative part of the hard scattering process, which was described in the preceding paragraph, can be calculated analytically. Different Next–To–Leading order (NLO) theoretical predictions of the Inclusive Jet Cross-Section will be discussed later in this chapter. They are based on a jet definition at the parton level and include all the Feynman diagrams contributing terms of order $(\alpha_s)^n$ with $n \leq 3$. Chapter 4 introduces several Monte Carlo generators which are based on Leading Order (LO) calculations. The contributions of higher order are partially included by means of the Leading Log Perturbation Theory that keeps all leading–log terms like $\left[\alpha_s lnQ^2\right]^n$ for all n.

2.3.2 Non–Perturbative QCD

Color confinement states that free particles can only exist as color singlets. During the hard scattering interaction, the colliding hadrons break into their components. Typically, only two partons participate in the hard interaction. The remaining of the colliding hadrons, or "spectator" partons, form the recoil system which is not involved in the hard collision. The scattered parton and the recoiling system move apart but are still joined by color flux lines. These lines stretch and break, materializing $q\overline{q}$ pairs which, together with the quarks and gluons resulting from the parton showering, re–group into colorless hadrons. The process of creation of additional $q\overline{q}$ pairs by the color force field and the subsequent reorganization of quark and gluons into hadrons is called **fragmentation or hadronization .** Hadronization is a non–perturbative process that follows parton showering and yields to the production of collimated beams of particles called **jets.** These colorless objects, which move away from the interaction point in the direction of their parent partons, are the experimental signature of the hard collision.

The non–perturbative part of jet production cannot be calculated from scratch. It has to be described semi–empirically guided by general principles and physical ideas. As a first approximation, each parton fragments independently. Then, the probability of finding a hadron h with a fraction z of the energy of the parent parton i is represented by the fragmentation function $D_{h/i}(z)$ which depends on z alone. These functions are related to the cross section for hadron production and can be obtained experimentally. Some Monte Carlo generators use independent fragmentation while others use more sophisticated models.

2.4 Jet Cross Sections

Most of the jet cross section in hadron–hadron collisions is due to soft processes that cannot be calculated from first principles. The interest here is only focused on the hard parton–parton scattering cross section which can be calculated using perturbative QCD and becomes predominant at high energies.

2.4.1 Jet Kinematics

The fractions of proton/anti–proton momentum x_1/x_2 carried by the initial state partons are not known in hadron collisions. When this fractions are not equal, the CM system is boosted along the direction of the beam. The usual quantities E and $\overline{p}$ are not convenient to describe the hard collision. The resulting jets can be described in a more clearly relativistically invariant way using the variables p_T (transverse momentum), φ (azimuth angle), y (rapidity), and m (mass). The rapidity is defined as:

$$y = \frac{1}{2} ln \frac{E + p_z}{E - p_z} = \frac{1}{2} ln \frac{1 + \beta cos\,\theta}{1 - \beta cos\,\theta}\,,$$

where z is the beam direction and β is the boost along z. The transverse energy of the jet is defined as its energy in the rest frame. Then,

$$E = E_T cosh\, y$$

$$p_T = p sin\,\theta\,.$$

In the case of jets with zero mass ($\beta = 1$) the pseudo–rapidity is defined as $\eta \equiv y|_{m=0}$ or:

$$\eta = -ln\left[tan\left(\frac{\theta}{2}\right)\right].$$

Within the zero mass approximation, $y = \eta$ and $p_T = E_T$.

The advantage of replacing the observables E, $\overline{p}$ by E_T, φ, η, m is that the effect of a boost along the z–axis changes only η, and only by a β dependent additive constant. In this way, properties which only depend on differences in η are independent of the initial conditions. These topics are discussed in detail in reference[29].

2.4.2 Contributing Processes

In perturbation theory, the jet cross section is expanded to all orders in α_s. A number of Feynman diagrams are associated with different parton–parton scattering subprocesses which contribute to α_s^n.

The lowest order diagrams contribute terms of second order in α_s and they describe $2 \rightarrow 2$ subprocesses which lead to two–jet or dijet events. Table 2.1 summarizes all possible $2 \rightarrow 2$ subprocesses in QCD and Figure 2.6 shows some examples of the associated diagrams. The picture in Figure 2.7 is a picture of a real two–jet event observed with the DØ detector. The total cross section for dijet production in $p\overline{p}$ collisions is described by the following formula:

$$\sigma(p\overline{p} \rightarrow 2jets) = \sum_{abcd} \int \int dx_p dx_{\overline{p}} f_{a/p}(x_p) f_{b/\overline{p}}(x_{\overline{p}}) \sigma(ab \rightarrow cd)\,,$$

where a, b are the initial state partons, c, d are the final state partons and $\sigma(ab \rightarrow cd)$ is the cross section of the subprocess $ab \rightarrow cd$.

All possible $2 \rightarrow 3$ subprocesses are included in Table 2.2. The third jet may be emitted from the incoming parton lines (initial state radiation) or the outgoing scattered lines (final state radiation). Some of the Feynman diagrams which describe $2 \rightarrow 3$ subprocesses are shown in Figure 2.8. A picture of a three–jet event observed with the DØ detector is included in Figure 2.9.

Table 2.1: List of all possible $2 \to 2$ subprocesses in QCD. q and $q\prime$ denote different quark flavors.

Subprocess	$\lvert M(90)^\circ \rvert^2 / 16\pi^2 \alpha_s^2$
$qq\prime \to qq\prime$	2.2
$q\overline{q}\prime \to q\overline{q}\prime$	2.2
$qq \to qq$	3.3
$q\overline{q} \to q\prime\overline{q}\prime$	0.2
$q\overline{q} \to q\overline{q}$	2.6
$q\overline{q} \to gg$	1.0
$gg \to q\overline{q}$	0.1
$qg \to qg$	6.1
$gg \to gg$	30.4

Table 2.2: List of all possible $2 \to 3$ subprocesses in QCD. q and $q\prime$ denote different flavors of quark.

Subprocess	Subprocess
$qq\prime \to qq\prime g$	$q\overline{q} \to q\overline{q}g$
$qg \to qq\prime\overline{q}\prime$	$q\overline{q} \to ggg$
$q\overline{q}\prime \to q\overline{q}\prime g$	$qg \to qgg$
$q\overline{q} \to \overline{q}\prime q\prime g$	$gg \to q\overline{q}g$
$qq \to qqg$	$gg \to ggg$
$qg \to qq\overline{q}$	

The cross section for this kind of events is:

$$\sigma(p\overline{p} \to 3jets) = \sum_{abcde} \int \int dx_p dx_{\overline{p}} f_{a/p}(x_p) f_{b/\overline{p}}(x_{\overline{p}}) \sigma(ab \to cde) \, .$$

Higher order QCD subprocesses give more elaborate configurations which mostly account for very collimated gluons or $q\overline{q}$ pairs radiated by the incident or scattered partons. The total inclusive jet cross section is given by:

$$\sigma(p\overline{p} \to jet + X) = \sum_{abc} \int \int dx_p dx_{\overline{p}} f_{a/p}(x_p) f_{b/\overline{p}}(x_{\overline{p}}) \sigma(ab \to c + X) \, ,$$

where X accounts for any number and type of objects, including jets, that could be produced together with the scattered parton c. A Leading Order (LO) calculation of the inclusive jet cross section includes all terms of second order in α_s. The Next–To–Leading Order calculation also includes the α_s^3 terms. Higher order predictions are not currently available.

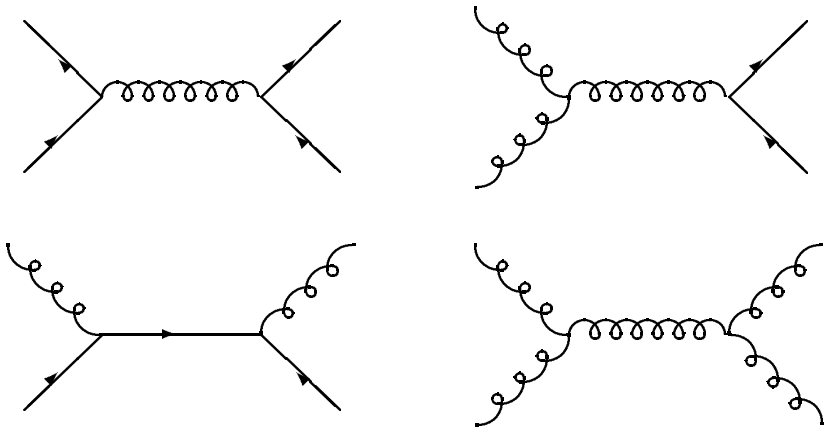

Figure 2.6: Examples of $2 \to 2$ subprocesses contributing to second order in α_s.

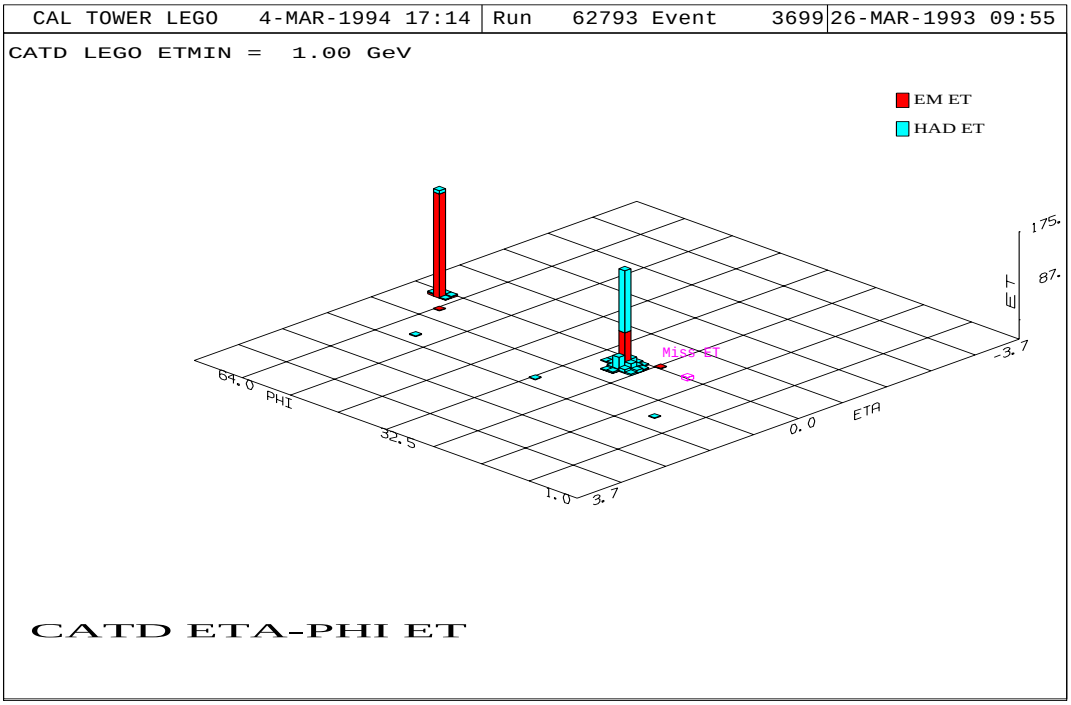

Figure 2.7: Two–jet event observed in the DØ calorimeter.

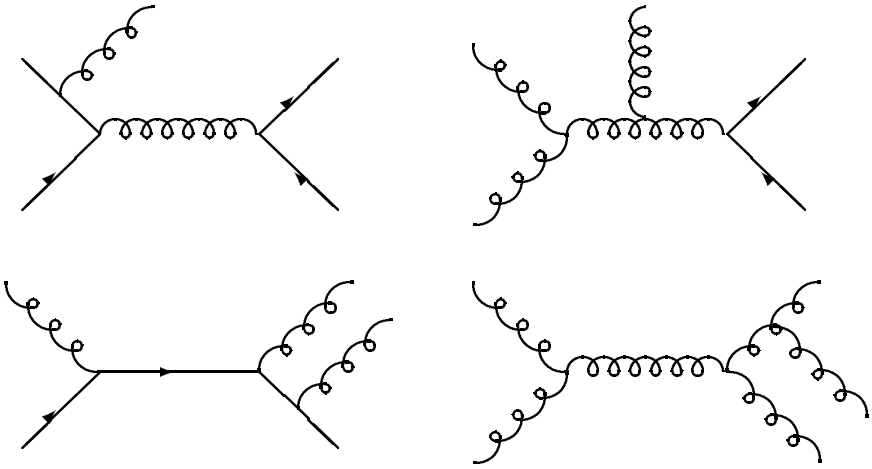

Figure 2.8: Examples of $2 \to 3$ subprocesses contributing to third order in α_s.

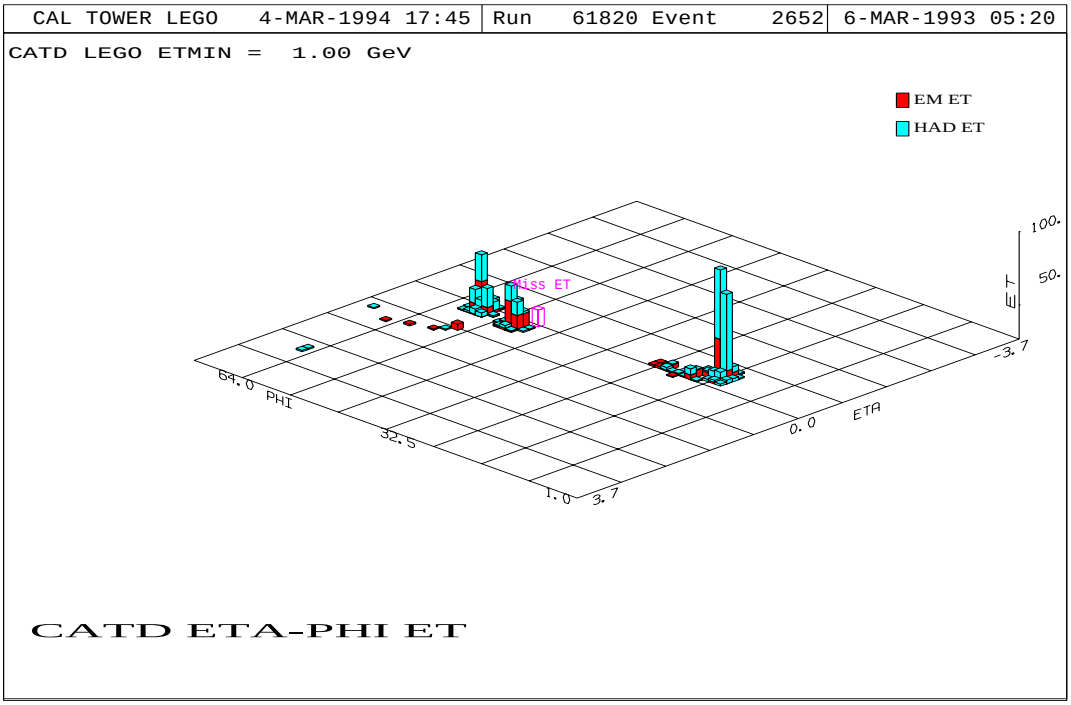

Figure 2.9: Three–jet event observed in the DØ calorimeter.

2.4.3 Inclusive Differential Jet Cross Section

It is difficult to measure the total jet cross section. Part of the cross section is inaccessible due to the limited solid angle subtended by the detectors. Although DØ's angular coverage is excellent, many jets produced near the beam pipe are not fully detected. Furthermore, the total cross section falls very rapidly as the jet E_T increases. Thus, a large contribution to the cross section comes from low E_T jets in a region which is very difficult to measure due to trigger and reconstruction inefficiencies, and contamination coming from other soft processes.

One way to sort out most of the problems mentioned in the preceeding paragraph is to measure the differential cross sections with respect to the jet transverse energy and pseudo–rapidity. This measurement is experimentally attainable and the associated QCD predictions are also available. The inclusive differential jet cross section measured at DØ is defined as:

$$\frac{d^2\sigma}{dE_T d\eta}\left(p\overline{p} \rightarrow jet + X\right) .$$

Both the measurement and the theory are binned in terms of the jet E_T and η.

EKS (NLO) Prediction. Ellis, Kunszt and Soper (EKS)[49] use the full 3rd order matrix elements calculated by Ellis and Sexton[30] to obtain the inclusive jet cross section in NLO, including both quarks and gluons. Jet definition becomes a fundamental and controversial issue in high order calculations when more than two partons are produced in the final state. The jet definition issue both at theoretical and experimental level will be addressed in chapter 4 since it is strongly correlated to detector features and reconstruction algorithms. For now, it is enough to say that the EKS calculation is done at the parton level including all terms of 3rd order in α_s. In other words, there are, at most, three partons in the final state.

Each parton is related to a parton jet by itself or merged with others into one single parton jet if the partons satisfy an E_T weighted distance condition in $\eta - \varphi$ space. In any case, the kinematic variables of the parton jet take their values from those of the parent parton or partons.

The sensitivity of EKS's calculation to the value of the renormalization scale μ^2 is less than 10%. The uncertainty in the cross section due to the choice of the parton distribution functions is of the order of 20%.

JETRAD. Giele, Glover and Kosower[31, 32] created JETRAD, a program to perform NLO calculations in jet physics. Like EKS, it includes all terms of third order in α_s. The jet cross section calculation is done at the parton level and includes initial state radiation. The phase space integrals are performed numerically, via a Monte Carlo integration technique. Unlike EKS, JETRAD does not need to introduce a cone around the partons to deal with soft radiation and collinear singularities. Instead, the method is based on the Lorentz invariant minimal invariant mass s_{min} as a theoretical resolution parameter[33]. If the invariant mass of a parton pair is smaller than the minimal invariant mass, only one parton is resolved; if $s_{ij} > s_{min}$ both partons are resolved. This allows the integration over the singular parts of phase space without calculating the hard matrix element explicitly. Any jet algorithm may be applied later to the final state partons.

2.4.4 Quark Compositeness

More than sixty years after the atomic structure experiments, a very similar phenomenon was observed in hadron colliders. These new experiments are exact analogues of Rutherford scattering. In fact, the quarks involved in a hard scattering interaction follow the Rutherford formula :

$$\frac{d\sigma_R}{d\Omega} \approx \frac{\alpha_s^2}{4E^2} \frac{1}{sin^4(\theta/2)} \, .$$

The proliferation of quarks and leptons has led to the speculation that they are composite structures, bound states of more fundamental constituents which are often called preons. In the same way that Rutherford established the presence of the nucleus within the atom and modern experiments discovered that hadrons were made of quarks and gluons, the measurement of high E_T jet cross sections offers a way to search for quark compositeness. If quarks and leptons were actually composites of more basic preons, there would be a modification of the parton – parton scattering amplitudes given by QCD. In the simple case of the coupling of two left–handed quarks, Eichten et al.[34] proposed an empirical contact term to account for the new interaction:

$$\mathcal{L} = \frac{\pm 1}{2\Lambda_c^2} (\overline{u}_L \gamma^\mu u_L + \overline{d}_L \gamma^\mu d_L)(\overline{u}_L \gamma_\mu u_L + \overline{d}_L \gamma_\mu d_L) \, .$$

The addition of this term leads to an enhancement in the low η inclusive jet cross section when the CM energy of the interacting partons approaches the energy scale Λ_c associated with preon point–like interactions. Figure 2.10 shows LO predictions of the inclusive jet cross section using **PAPAGENO,** a monte generator which includes the compositeness contact term. The sensitivity of the high E_T jet cross section to the value of Λ_c is clear.

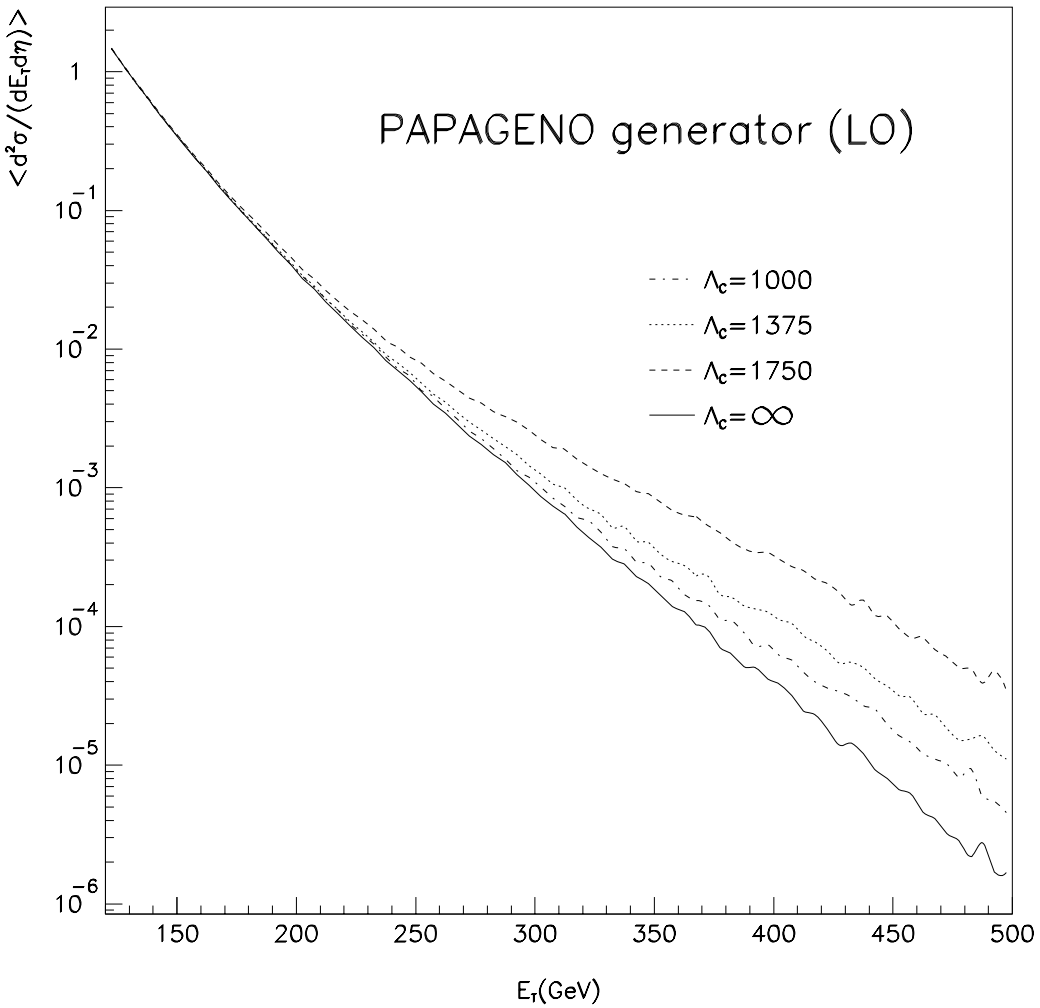

Figure 2.10: Inclusive differential jet cross section ($|\eta| < 0.9$) using the PAPAGENO generator (LO) with different values of Λ_c.

Chapter 3

Experimental Design

3.1 The Fermilab Tevatron

In 1985, the Tevatron $p\overline{p}$ collider started to operate at the Fermi National Accelerator Laboratory (Fermilab–USA) and opened new frontiers in high energy physics research. The Fermilab complex, shown in Figure 3.1, includes a set of five separate accelerators working in concert to produce $p\overline{p}$ collisions with an energy of 1.8 Tev in the center of mass. The Tevatron itself is the last accelerator in the chain. This section describes the different steps in the acceleration process [35, 36].

A **Cockroft–Walton** electrostatic accelerator provides the first stage of acceleration generating a beam of 750 keV negative hydrogen ions which then enter a linear accelerator. The **Linac** is approximately 150 m long and accelerates the H^- ions to 400 Mev. Upon entering the third stage, the **Booster ,** the ions pass through a carbon foil which removes the electrons leaving only a beam of protons. The Booster accelerates the protons to 8 GeV and loads them into the **Main Ring ,** the second proton synchrotron 2 km in diameter that consists of $1,000$ conventional copper–coil iron yoke magnets which continually bend and focus the protons. When the protons reach 150 GeV, they are injected into the **Tevatron** ,

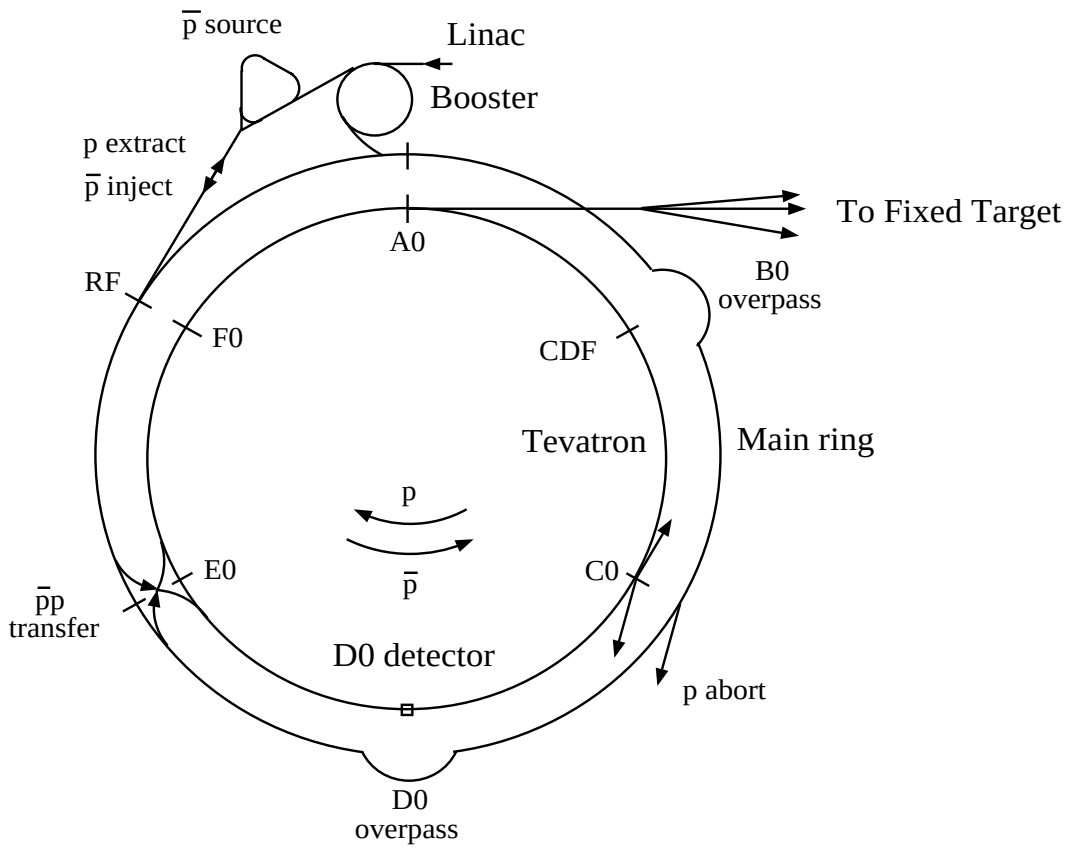

Figure 3.1: Overhead view of the Fermilab complex.

the third synchrotron that $1,000$ superconducting magnets to guide and accelerate charge particles. The Tevatron ring is located directly 65 cm below the Main Ring magnets, except where the Main Ring bypasses the colliding beam experiments. Six bunches of protons are injected into the Tevatron.

The anti–proton beam is produced in a multi–stage process starting in the Main Ring and involving several different machines. Production starts when a proton bunch is extracted from the Main Ring at 120 GeV. The bunch is directed onto a tungsten target producing $\overline{p}$'s with wide momentum spread. A strong focusing magnet, the lithium lens, selects $\overline{p}$'s with a momentum spread of 3% around 8.9 GeV. Then, the $\overline{p}$'s are injected into a small synchrotron, called the

Debuncher, where they circulate for 2 sec while the momentum spread is reduced and transverse betatron emittance is reduced via stochastic cooling [12]. This cooling process is then continued in the accumulator, a storage ring where the $\overline{p}$'s are accumulated for several hours (stacking) until there are enough of them to transfer to the Main Ring. When that happens, six bunches of $\overline{p}$'s are extracted from the core of the beam where the energy spread is only 0.05%. Then, they are injected into the Main Ring where they are accelerated to 150 GeV.

When the $\overline{p}$ bunches are transferred to the Tevatron, there are already 6 bunches of protons circulating in the opposite direction. A radio frequency process called cogging is used to adjust the 12 intersection points so that a bunch crossing occurs at each intersection point every 3.5 μs. Then, all bunches are accelerated to 900 GeV to provide a CM energy of 1.8 TeV.

The instantaneous luminosity, $\mathcal{L}$, is a measurement of the interaction rate. It is given by:

$$\mathcal{L} = \frac{f N_b N_p N_{\overline{p}}}{4\pi\sigma^2}$$

where f is the crossing frequency, N_b the number of bunches, N_p, $N_{\overline{p}}$ the number of p's and $\overline{p}$'s and $\pi\sigma^2$ the area or section of the beam. One way to increase the instantaneous luminosity at the collision point is to reduce the transverse beam size in that region. This is done by strong quadrupole magnets located near each interaction point.

During the $1992-1993$ collider run (run $1A$), the Tevatron established a peak luminosity record of 9.22×10^{30} cm^{-2} sec^{-1}. A new record was established again in 1994 with a peak luminosity of 16.5×10^{30} cm^{-2} sec^{-1}

3.2 The DØ Detector

The DØ detector is a multipurpose apparatus designed to study the physics processes resulting from $p\overline{p}$ collisions with an energy of 2 TeV in the center of mass. The description presented here is based on reference [37].

The detector was built to cover a wide spectrum of physics topics by providing accurate measurements to test the Standard Model predictions and search for new phenomena. This includes the search for the top quark, various jets and photon cross section measurements, b–quark production and W, Z bosons studies. To accomplish this, DØ was designed for:

- identification and measurement of electrons and muons,
- measurement of parton jets at large p_T through highly segmented calorimetry with good energy resolution,
- determination of the missing transverse energy ($\not{E}_T$) as a way of detecting neutrinos and possibly other non–interacting particles.

A general view of the DØ detector is shown in Figure 3.2. A right–handed coordinate system is adopted, in which the z–axis is along the proton direction and the y–axis is upward. The angles φ and θ are the azimuthal and polar angles, respectively. The r coordinate is the distance from the beam axis.

In the following sections, the different components of the DØ detector are described. From the inside to the outside, the detector consists of three main systems: the central detectors, the calorimeters and the muon system. The calorimeters deserve a more detailed description as they are the main instrument for the measurement of jets.

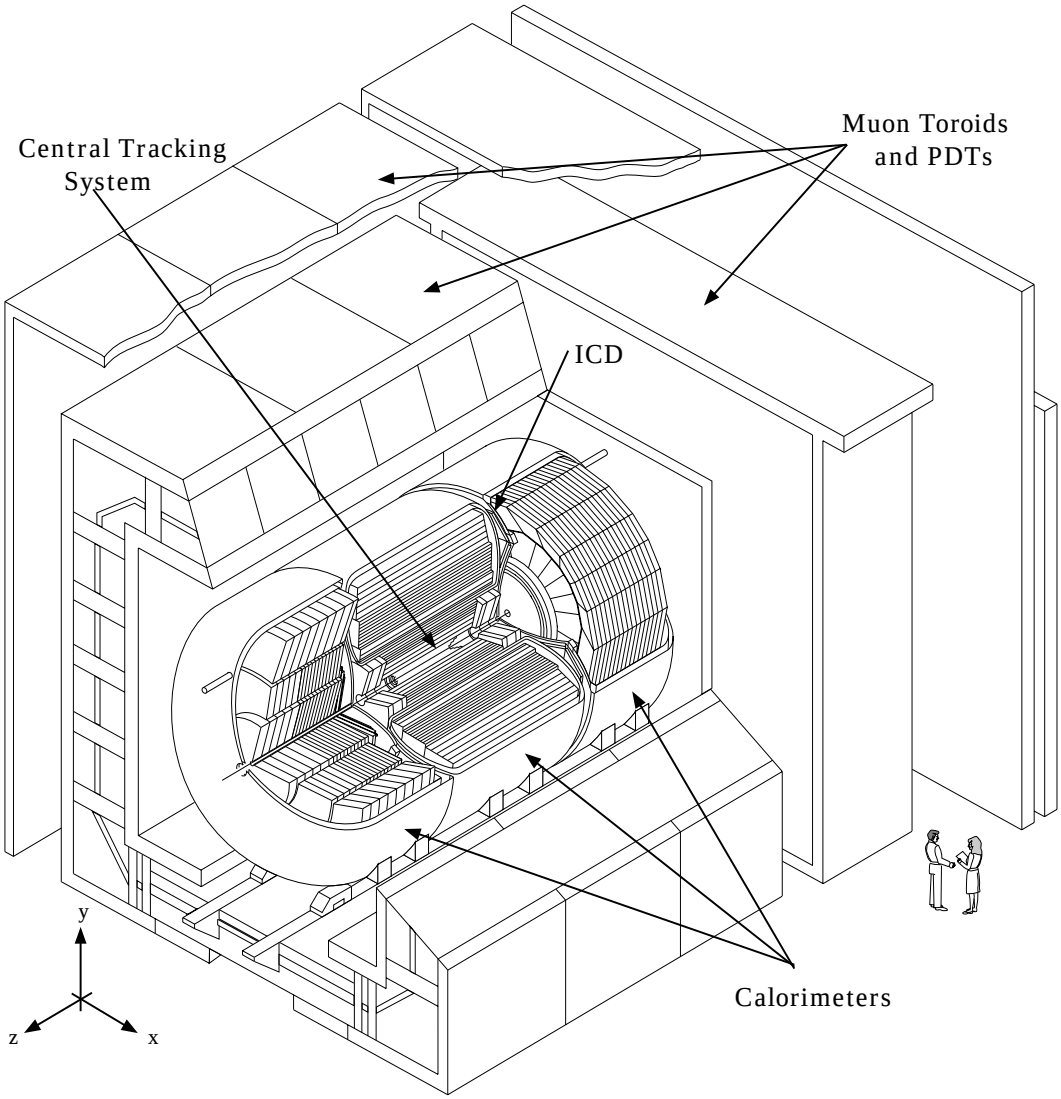

Figure 3.2: The DØ detector.

Figure 3.3: $r - z$ view of DØ Central Detectors.

3.2.1 Central Detectors

The Central Detectors system, illustrated in Figure 3.3, is a set of concentric tracking and transition radiation chambers. Drift chambers consist of an array of wires set to a high electrostatic potential. When an energetic charged particle crosses the chamber, the charge resulting from the gas ionization is collected by the wires. The time of flight of that charge is translated into coordinates in space. The track is finally reconstructed from the 'hit' positions associated with each wire. The detector is very compact, fitting within the inner cylindrical aperture of the calorimeters in a volume bounded by $r = 78$ cm and $z = \pm 135$ cm. The system was designed for good spatial resolution of individual particles, good two track resolving power, high efficiency, and good ionization energy determination.

From the inside to the outside the sub–detectors are:

- The **Vertex Chamber** (VTX) is the innermost drift chamber and surrounds the beam pipe. It was designed to reconstruct tracks around the interaction point and measure the vertex position. The vertex and tracking information is essential for non–inclusive jet analysis and for an accurate determination of the jet E_T . The chamber is divided into three independent concentric layers of cells. In each cell, 8 staggered sense wires parallel to the beam direction provide a measurement in the $r - \varphi$ plane. The z coordinate is determined by charge division. A slow gas gives an average drift velocity of 7.3 μm/ns. The typical hit resolution is 50 μm in the drift plane. Two hit resolution with 90% efficiency is achieved for tracks that are separated by 0.63 mm in the $r - \varphi$ plane.

- The **Transition Radiation Detector** (TRD) surrounds the Vertex Chamber and its function is to distinguish between electrons and charged pions. This is accomplished by measuring transition radiation X–rays produced when highly relativistic charged particles pass through the interface between two materials with different dielectric constants. The TRD consists of three separate layers each containing a radiator and an X–ray detection chamber. The radiator is made of polypropylene foils in a volume filled with nitrogen gas. The X–ray detection is done by a drift chamber mounted just after the radiator. Pion rejection factors of approximately 50 are found for 90% efficiency detecting electrons.

- The **Central Drift Chamber** (CDC) is the outermost tracking chamber. It consists of four independent layers of cells with seven staggered sense wires

each providing coverage for tracks at large angles just prior to their entrance into the Central Calorimeter. A fast gas fills the volume of the chamber, in which the inner and outer radii are 49.5 and 74.5 cm respectively, giving a drift velocity of 34 μm/sec. The hit resolution is $150 - 200$ μm and 90% efficiency for 2 hit resolution is achieved for a ≈ 2 mm separation.

- The **Forward Drift Chambers** (FDC) are located upstream and downstream of the concentric barrels of the VTX, TRD and CDC and before the end calorimeters. They provide charged particle tracking coverage down to 5°. The high occupancy of the chamber is a consequence of its proximity to the beam line and this makes track reconstruction difficult, especially at low angles. Each FDC package consists of three separate chambers: the Φ module with radial wires which measures the φ coordinate; two Θ modules offset in φ by 45° with azimuthal wires which measure the θ coordinate. The Φ module is sandwiched between the two Θ modules. The FDC uses the same gas as the CDC and obtains similar resolution and efficiency values.

3.2.2 Calorimeters

The Calorimeters are the most important tool for jet detection. They provide energy measurement for electrons, photons and jets. Other important roles of DØ calorimetry are particle identification and the determination of the Missing Transverse Energy ($\not{E}_T$).

A general view of the DØ liquid argon calorimeters is displayed in Figure 3.4. Three double–walled stainless steel cryostats enclose and support the DØ calorimeters. Excellent containment and hermeticity are achieved with a **Central Calorimeter** (CC) covering roughly $|\eta| < 1$ and two **End Calorimeters** (EC) which extend

the coverage out to $|\eta| \approx 4$. The number of nuclear absorption lengths (λ_A) is typically 7 for the CC and 9 for the EC. Figure 3.5 shows a plot of the number of interaction lengths as a function of θ.

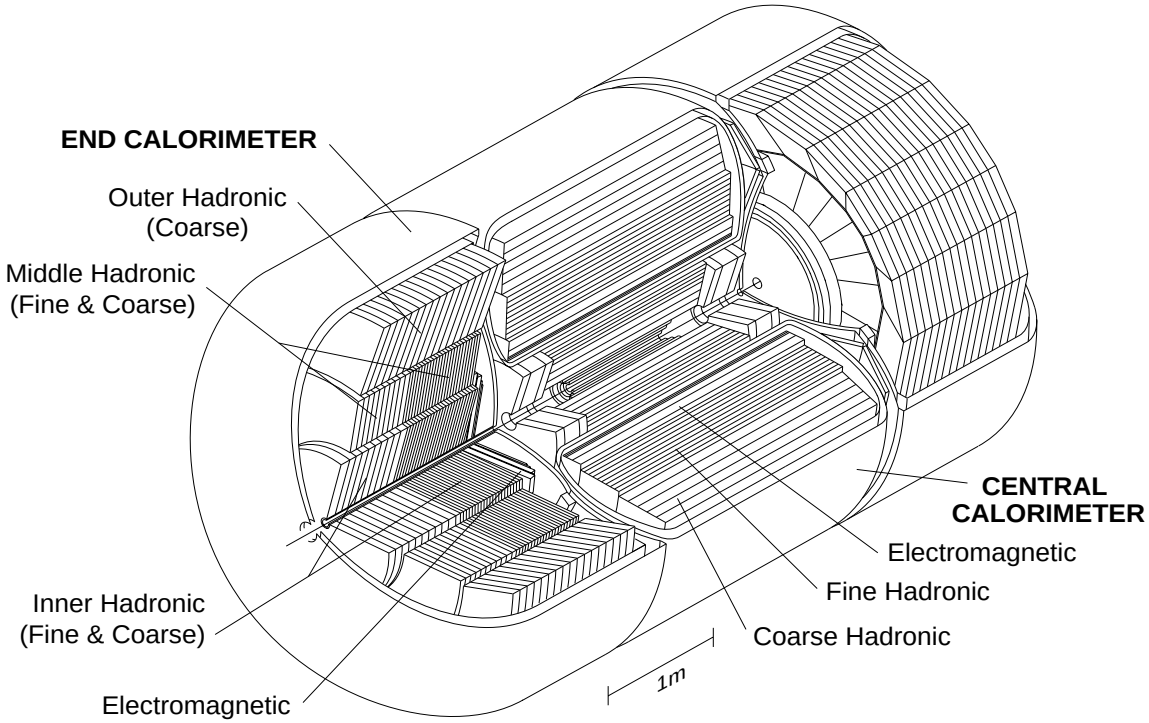

Figure 3.4: General view of DØ calorimeters.

The basic detection principle of these sampling detectors is illustrated in Figure 3.6. A calorimeter unit cell consists of a metal absorber plate and a signal board which is plated with a coat of resistive epoxy on each surface and has a copper plane on the inner side. These two elements are separated by a gap filled with liquid argon as an active material. The metal plate is connected to ground and the resistive surface to a positive high voltage $2 - 2.5$ keV establishing an electrostatic field in the argon gap. As the particles enter the calorimeter, they interact with the array of absorber plates producing a shower of particles and los-

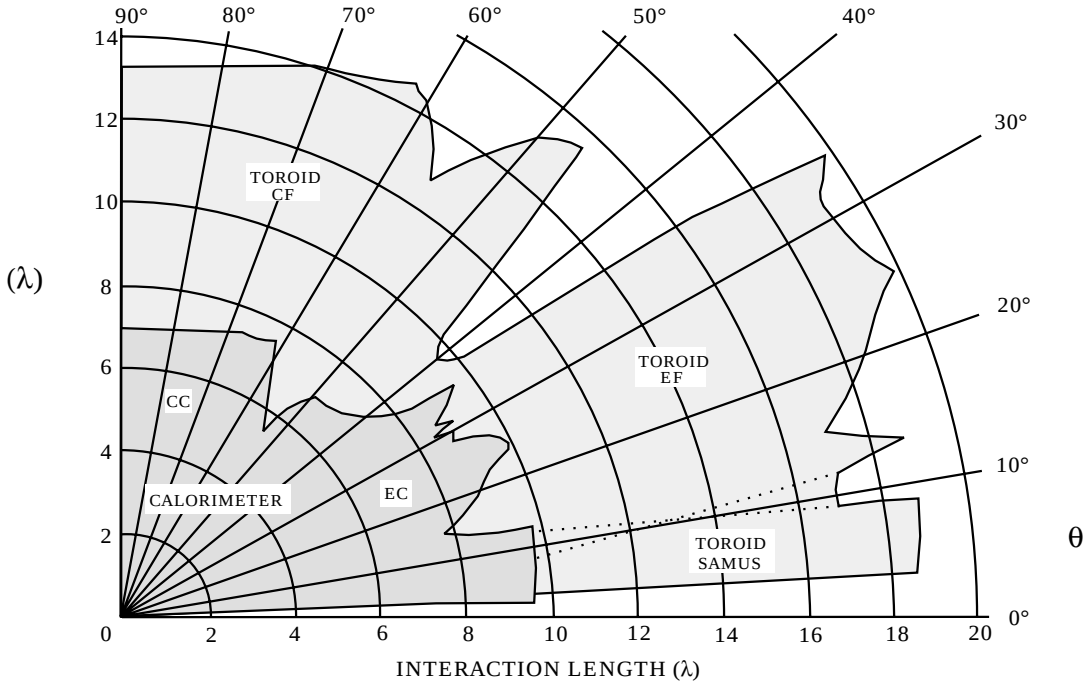

Figure 3.5: Calorimeters and muon system interaction lengths as a function of θ.

ing most of their energy. A small fraction of the total energy is deposited in the gaps as the particles ionize argon atoms. The charge drifts to the sampling plate inducing a signal in the copper readout pads which is transmitted to preamplifiers located on top of the cryostat walls. Then, the signal is shaped and amplified before it is digitized and passed to the data acquisition system. In addition, the zero–suppression process eliminates the cells with no energy deposited in them. This process minimizes the readout time and reduces the size of the data.

One distinct characteristic of DØ calorimetry is the pseudo–projective geometry. This means that straight lines can be drawn from the interaction point through the centers of an array of cells forming a 'tower'. Typical transverse sizes

of towers are $\Delta\phi \times \Delta\eta = 0.1 \times 0.1$, providing excellent shower position resolution.

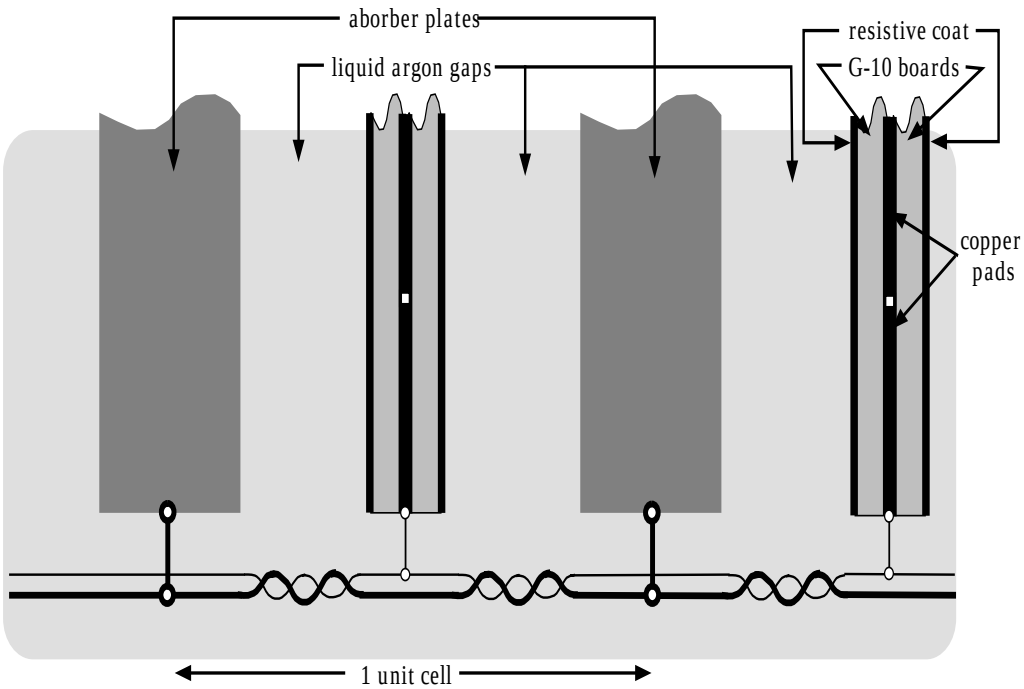

Figure 3.6: Diagram of a Calorimeter unit cell.

Central Calorimeters

The three types of concentric cylindrical modules in DØ calorimeters are illustrated in Figure 3.7.

- The **Electromagnetic Modules (EM)** are made of 3 mm thick uranium plates and the read out is done in four longitudinal read out layers which have 2, 2, 7 and 10 radiation lengths in depth. The third layer is more finely segmented than the other three. Its segmentation is $\Delta\phi \times \Delta\eta = 0.05 \times 0.05$ to provide better transverse measurement at electron shower maximum. The full EM coverage is approximately 20 radiation lengths (X_0).[1]

- The **Fine Hadronic Modules (FH)** consist of 6 mm thick uranium–niobium alloy absorber plates segmented into three longitudinal layers with a total width of 3.2 nuclear absorption lengths (λ_A).

- The **Coarse Hadronic Modules (CH)** consist of one readout layer made of 46.5 mm copper absorber plates with a total depth of 3.2 λ_A.

The cylindrical shells are also segmented in φ. The cracks between modules arrays are offset so that there are no completely projective intermodule cracks. There are 32 EM modules in the inner ring, 16 fine FH and 16 CH in the outer ring.

End Calorimeter

The EC's are quite similar to the CC. There are two mirror–image End Calorimeters containing four types of modules as shown in Figure 3.7. The single EM module is divided into four read out layers with 4 mm absorber plates with a total length of $\approx 20X_0$. There is also only one Inner Hadronic Module (IH) with a four layers FH section and a single read out layer CH section. Outside the EM and IH, there are concentric rings of 16 Middle (MH) and Outer (OH) modules with four and one read out sections, respectively. In the OH modules of the End Calorimeters, absorber plates are made of stainless steel instead of cooper. The EC has a total depth of $7 - 9\lambda_A$.

Intercryostat Detectors and Massless Gaps

Between the CC and the EC calorimeters, the region defined by $0.8 < |\eta| < 1.4$, shown in Figure 3.7, presents a large amount of uninstrumented material. A substantial amount of energy is lost in the cryostat walls, module endplates

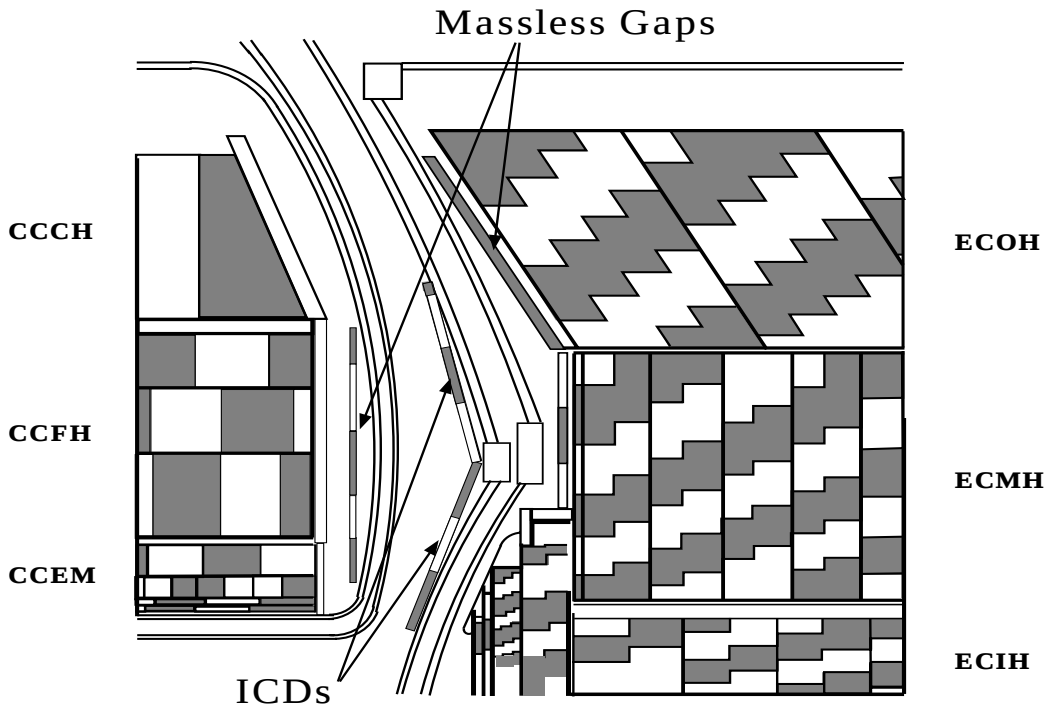

Figure 3.7: Side view of calorimeter modules, intercryostat detectors and massless gaps.

and support structures. Two types of detection systems were added to improve calorimetric sampling without causing additional shower multiplication:

- The **intercryostat detectors** (ICD) are a set of scintillation counters[1] mounted on the front surface of the EC's. Each ICD consists of 385 scintillator tiles of size $\Delta\eta = \Delta\phi = 0.1$ matching the liquid argon calorimeter cells.

- The **Massless Gaps** (MG) are separate single – cell structures installed in both CC and EC calorimeters between the module endplates and the cryostat walls.

Calorimeter Performance

The Calorimeter performance has been studied in many different ways. In a sampling calorimeter, the energy is measured on a statistical basis[61]. Therefore, fluctuations are expected about the mean response. In addition, the calorimeter energy resolution is affected by electronic noise, background radiation and the nature of the incident particles. The fractional energy resolution is defined as the ratio of the resolution to the mean response:

$$\left(\frac{\sigma_E}{E}\right)^2 = \frac{N^2}{E^2} + \frac{S^2}{E} + C^2 \,,$$

where N is the noise term, S the sampling term and C is a constant offset term. Test beam studies show that the calorimeter energy resolution is approximately $15\%/\sqrt{E}$ for electrons and $50\%/\sqrt{E}$ for pions. The calorimeter energy resolution for jets is obtained from real collider data. Its effect on the jet cross section measurement will be discussed in chapter 6.

During test beam studies [38], beams of electrons and pions at different energies were used to analyze the calorimeter energy response and resolution. A minimum ionizing particle crossing the central calorimeter would liberate approximately 10^4 electrons in each gap and lose a total energy of ≈ 2 GeV. The energy response to both electrons and pions is linear to within 0.5% for electrons with energy above 10 GeV and pions with energy above 20 GeV. The e/π response ratio falls from about 1.11 at 10 GeV to 1.04 at 150 GeV.

3.2.3 Muon System

The muon system is a set of magnets and proportional drift tube (PDT) chambers located outside the calorimeters with a θ coverage that goes down to approximately 3°. The purpose of the system is the identification of muons produced in $p\overline{p}$ collisions and the determination of their trajectories and momenta. As shown in Figure 3.8, there are of two main sets of chambers:

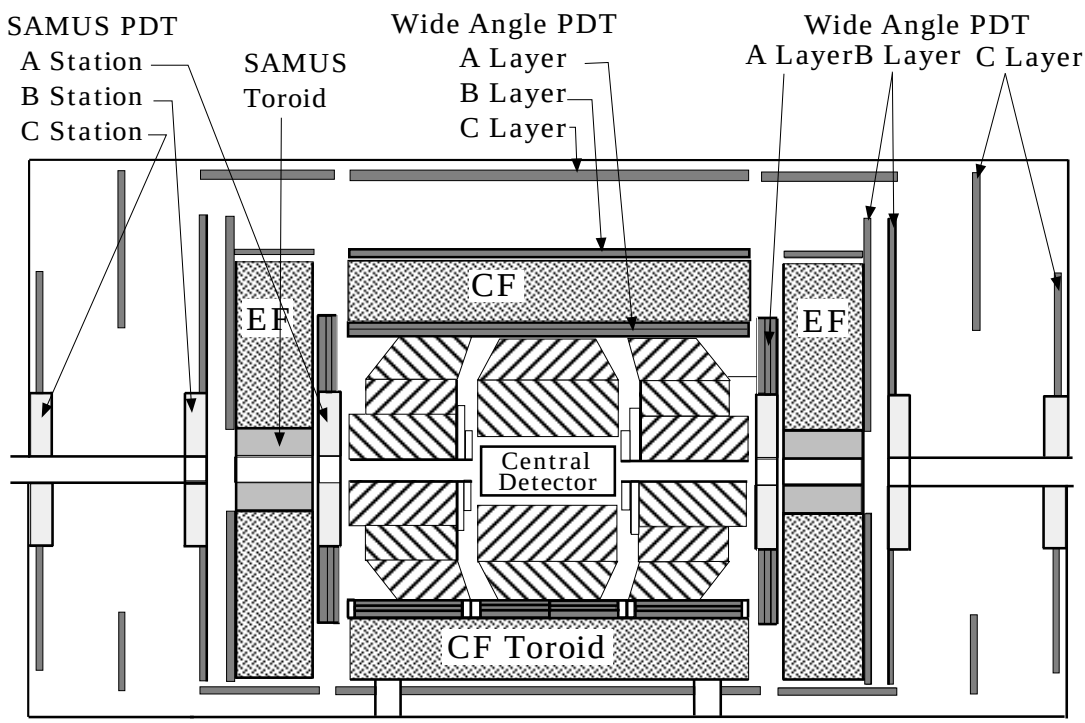

Figure 3.8: Elevation view of DØ Detector including the muon chambers

- The **Wide Angle Muon Chambers** (WAMUS) provide coverage at large angles ($|\eta| < 1.7$). A total of 164 individual chambers are deployed in three layers: the A layer before the iron toroids and the B and C layers after the magnets. There are 4 PDT planes of cells in an A layer chamber and 3 in

a B or C chamber. One wire per cell runs along the x direction in the top and bottom chambers and along the y direction in the side chambers. As a consequence, the magnetic field $\vec{B} = 1.9$ T $\hat{\varphi}$ bends the muons in the $r - z$ plane. The muon direction is measured before and after the magnets and the momenta is obtained from the bending angle. The hit resolution is 3 mm along the wire direction and $700 - 900$ μm along the drift plane.. The muon p_T resolution is $\Delta p/p \approx 20\%$ due to multiple scattering at low momenta and is limited by the bend coordinate resolution at higher momenta.

- The **Small Angle Muon Chambers** (SAMUS) was designed to provide coverage at small θ angles. SAMUS is composed of three stations: A, before the magnets, and B, C after the magnets. Each station consists of three doubled planes of cylindrical proportional drift tube chambers. They are oriented in x, y and u directions (u is at 45° with respect to x, y). The hit resolution is approximately $400 - 500$ μm. The p_T resolution is mainly determined by multiple scattering and equal to 20% for p_T less than $10 - 15$ GeV.

The muon system may be used in jet analysis to detect cosmic shower contamination and energy leakage outside the calorimeters in the case of high E_T jets.

3.2.4 Trigger and Data Acquisition Systems

The event selection and recording process is not trivial at a luminosity of $(5 - 10)$ $\times 10^{30}$ cm^{-2} s^{-1}. Each second, 215 to 430 thousand $p\overline{p}$ inelastic scattering interactions occur at the center of the DØ detector. The probability of single

and multiple interaction is $35-33\%$ and $17-44\%$ for each crossing, respectively. Since it is not possible to log and handle each interaction, a selection process is implemented to keep only those events of physics interest. Three trigger levels [37] involving hardware and software decisions, are able to reduce the event rate from $200-400$ KHz to 2 Hz before passing them on to the host computer for monitoring and recording. The following description puts particular emphasis on calorimeter triggering [41]. Jet triggers will be discussed in detail in chapter 5.

Hardware Triggers

The **level Ø** trigger system[39, 40] is the first level used to identify colliding beam crossings containing interactions. It consists of two hodoscopes of scintillation tiles located just outside the central tracking region, on the inside faces of the end cap calorimeters, 140 cm from the center of the detector. Each array covers a region of pseudo–rapidity of $1.9 < |\eta| < 4.3$. A coincidence of both arrays is $\geq 99\%$ efficient in detecting non–diffractive inelastic collisions. Due to its excellent time resolution, $100-150$ ps, the level Ødetector also provides a coarse measurement of the z–vertex position plus luminosity information.

The **level** 1 trigger uses information from different detector elements in order to reduce the event rate from $200-400$ kHz to 200 Hz. The level Ø scintillators provide the z–vertex position, the muon system supplies the number of muon tracks and the momentum of the muons, and the calorimeters provide information on the clusters of energy in the event. Within the beam crossing time of 3.5 μs, the level 1 trigger system is able to read up to 256 trigger variables which are combined to form up to 32 different triggers. In the particular case of the calorimeters, these triggers compare the sum over the cell analog outputs within

a trigger tower to a threshold set by the user. A trigger tower is a region defined by a 0.2×0.2 solid angle in $\eta - \varphi$ space (see Figure 3.9). The sums are done over all the electromagnetic and fine hadronic sections of each calorimeter tower within the range $|\eta| < 4$.

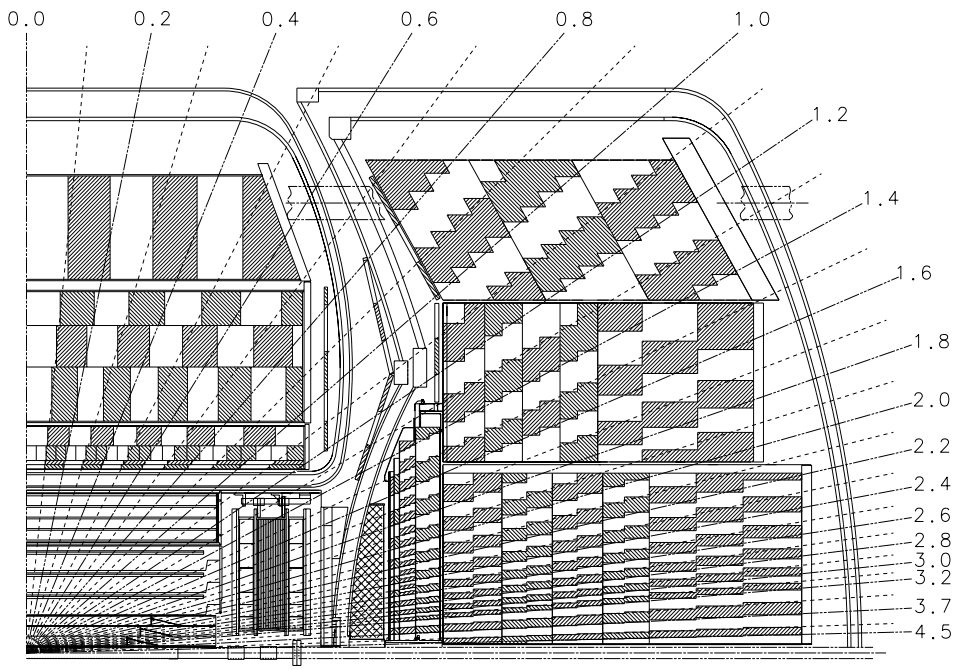

Figure 3.9: Side view of calorimeter trigger towers.

Software Triggers

The **level** 2 trigger and the **Data Acquisition System** are closely intertwined. The former is a software based event filter, placing more stringent cuts on the data to further reduce the rate from 200 Hz to 2 Hz. A maximum of 128 filters can be defined and run on a microvax farm containing 50 VS4000 − 60 processors working in parallel. Out of level 1, the events are transferred to the VAX farm where they are reconstructed and processed by the filters. In the case of the calorimeter filters,

the data are unpacked in the region flagged by the level 1 trigger. The level 1 towers are used as seeds for the jet filter. A jet algorithm adds together all the trigger towers within a fixed cone. The events with jets above a given threshold are sent to the host computer. Finally, the selected events are recorded on 8 mm tapes.

Chapter 4

Data Reconstruction and Simulations

DØ data go through a complicated computing process before they are ready to be analyzed in the production of physics results[37]. Once the events of interest are selected at the software trigger level, the data are mapped into the desired raw **ZEBRA** [42] structure. ZEBRA is a software product that gives standardized, hierarchical storage banks for commonly used data, together with reference links to other related banks. At the **raw** level, the banks are filled with digitized detector electronic signals associated with the readout of each channel. The event data forms a single tree structure and as reconstruction is done, extensive reference links among related bodies of data are established. The DØ reconstruction program, called **DØRECO** , turns raw data into hits, tracks and energy deposits. In a second step, DØRECO uses a set of algorithms to identify physics signatures like electrons, photons, muons, jets, and $\not\!\!E_T$. The fundamental physics quantities associated with them are also calculated and stored in particle banks. Two types of output files are provided by DØRECO. The **standard (STA)** file contains the raw data and complete reconstruction information. The **Data Summary Tape (DST)** contains summaries of tracks and energy clusters plus the particle banks.

In the case of QCD events, the DST files are streamed into smaller files obtained by selecting only the QCD triggers. These events are then written into smaller **MicroDST** files to be used in physics analysis such as the one presented here.

In this chapter, a description of the jet reconstruction process is followed by a discussion on jet definition. There is also a short reference to Monte Carlo event generators and detector simulation programs which are used extensively to help understand the detector performance and tune the reconstruction algorithms.

4.1 Interaction Vertex Measurement

The interaction vertex is determined with the help of the tracking chambers[43]. A precise measurement of its coordinates is essential to obtain the E_T and η of the jets.

The $x - y$ position of the vertex is determined from the tracks reconstructed by the vertex chamber in the $r - \varphi$ plane. Since the beam position remains fairly stable through time, the vertex $x - y$ position is obtained for each run as the average over all the events that belong to that run.

Instead, the z coordinate of the vertex has a broad gaussian distribution centered at $z \approx -10$ cm with a width of about 30 cm. The CDC or FDC tracks reconstructed in the $r - z$ plane are extrapolated until they intersect the z–axis. The mean of the gaussian distribution associated with the intersection points is taken as the z coordinate of the interaction vertex of the event. The z–vertex resolution varies within the range $0.65 - 0.95$ cm depending on the number of tracks in the event and their angular distribution. In the case of multiple interaction events, the two vertices are resolved if the clusters of tracks are separated more than 7 cm on the z–axis.

4.2 Jet Reconstruction

Experimentally, the jet appears as a result of a scattered parton that undergoes fragmentation. This beam of collimated particles showers as it crosses the calorimeters spreading its energy over a larger cone.

The event structure in hadron-hadron collisions is very complex. There is only one active parton from each incident hadron which participates in a $p\overline{p}$ hard scattering process. Then, only a fraction of the hadrons in the final state are to be associated with the hard scattering event. The remaining hadrons are the result of the soft interactions between the passive partons. This process is responsible for the underlying event which has to be subtracted from the hard scattering event. In $p\overline{p}$ collisions, the CM frame of the hard scattering event is typically boosted along the beam axis. Therefore, the most convenient set of kinematic variables to describe the jets are the transverse energy E_T , φ and the pseudo-rapidity η.

A jet definition based on a fixed cone in $\eta - \varphi$ space is well suited to the DØ detector features and has been widely used in hadron collider experiments. Such a definition helps to suppress the effect of the underlying event, since only a small fraction of the associated low E_T particles will fall into the cone of a high E_T jet. The fixed cone algorithm is also a good choice to test QCD predictions in NLO, since they include the contributions of processes that involve more than two jets in the final state. Compatibility between jet definitions used in different experiments is also essential to compare results.

DØ has adopted a fixed cone algorithm[44] to identify and reconstruct jets during the run $1A$ data taking. Successive combination style algorithms[45, 46], similar to those used in e^+e^- physics, are currently under study.

4.2.1 The Fixed Cone Jet Algorithm

The fixed cone algorithm is based on the assumption that the particles from a jet are contained within a cone of radius $R = \sqrt{(\eta - \eta_\circ)^2 + (\varphi - \varphi_\circ)^2}$ centered in the jet axis $(\varphi_\circ, \eta_\circ)$. The choice of a cone size $R = 0.7$ was made to ensure good shower containment and to minimize the jet E_T resolution[47]. This algorithm is similar to the one used by the UA1 and CDF collaborations.

- The jet reconstruction process starts with the determination of the E_T contained in $\eta \times \varphi = 0.1 \times 0.1$ calorimeter towers. This is accomplished by summing separately over electromagnetic or hadronic layers at the hardware level. The algorithm starts from this ordered list of towers which are labeled as **seed towers** if their E_T is greater than 1 GeV.

- Next, all neighbor towers with an E_T greater than 1 GeV are added up. These **preclusters** are used to cut down on the number of towers considered as possible starting points for jet formation.

- A new **cluster** is constructed by adding all the towers within a cone of radius $R = 0.7$ which is defined around the precluster center in $\eta - \varphi$ space. A new cone is defined around the energy weighted center of the jet and the process is repeated until the $\eta - \varphi$ centroid converges. In the case that different seeds form the same cluster, one of them is removed from the list. All the clusters with E_T less than 8 GeV are also removed.

- If a cluster does not share energy with others, it is listed as a **jet.** When it does, the two objects are either split or merged depending on the amount of E_T shared. Since the splitting–merging fraction (SMF) is 0.5, two clusters

will be merged into one jet if the amount of transverse energy they share is greater than 50% of the minimum of the E_T's of the two clusters involved. Otherwise, the clusters are split into different jets and the towers are assigned to the closest center.

The reconstruction process is completed with the calculation of the kinematic variables associated with each jet which are stored in the jet particle bank. The energy E of the jet is defined as:

$$E = \sum_i E_i \,,$$

where the sum is over all the calorimeter towers within the jet cone. Assuming that the measured jet is a cluster of massless particles or cells,

$$p_x = E_x = \sum_i E_{x_i}$$

$$p_y = E_y = \sum_i E_{y_i}$$

$$p_z = E_z = \sum_i E_{z_i} \,.$$

The jet centroid is given by:

$$tan\,\varphi_\circ = \frac{E_y}{E_x}$$

$$cos\,\theta_\circ = \frac{E_z}{\sqrt{E_x^2 + E_y^2 + E_z^2}} \Rightarrow \eta_\circ = -ln\left(tan\,\frac{\theta_\circ}{2}\right)$$

and the jet E_T is calculated as:

$$E_T = \sum_i \sqrt{E_{x_i}^2 + E_{y_i}^2} = \sum_i E_{T_i} \,.$$

Jet Definition. Experiment and Theory

Since the DØ inclusive jet cross sections are compared to EKS[48, 49] and JETRAD[31, 32] predictions, there has to be a good match between experimental and theoretical jet definitions. EKS is a (NLO) calculation of the inclusive jet cross section at parton level that includes both quarks and gluons. Thus, there are, at most, three partons in the final state. Jets are defined by means of a fixed cone algorithm. A cone of radius R is defined around the direction of each parton. Two partons are to be combined into a single parton jet if the condition:

$$\sqrt{(\eta_i - \eta j)^2 + (\varphi_i - \varphi j)^2} < \frac{E_{T_i} + E_{T_j}}{MAX(E_{T_i}, E_{T_j})} \times R$$

is satisfied, where E_{T_i} and E_{T_i} are the E_T 's of the partons involved. The introduction of a jet cone in conjunction with a merging condition in the NLO calculation is necessary to deal with singularities in the matrix elements that prevent the calculation of a finite cross section. These singularities occur when a third parton is very soft or is emitted collinear to the directions of the other initial or final state partons. As a result, a **parton jet** is an object that includes all the partons inside a cone of radius R centered on the average η and φ. The E_T and the $\eta - \varphi$ coordinates of the jet are calculated as:

$$E_T = \sum_i E_{T_i}$$
$$\eta = \frac{1}{E_T} \sum_i E_{T_i} \eta_i$$
$$\varphi = \frac{1}{E_T} \sum_i E_{T_i} \varphi_i \,,$$

where the sums are over the partons inside the cone. Unlike EKS, JETRAD allows the user to choose different jet algorithms. Since the JETRAD predictions

displayed in chapter 7 were obtained using the EKS algorithm, the definitions presented in this paragraph are also valid for JETRAD.

A collider jet crossing the calorimeters is a more complicated object. As the partons move apart after the hard interaction, they emit more partons which fragment into colorless hadrons. This narrow jet of collimated particles, or **particle jet** , gets wider as it crosses the calorimeter. Some of the numerous particles generated in the showering process that occur inside the calorimeter carry a fraction of the energy of the parent partons outside the cone defined by the reconstruction algorithm. Since experimentalists compare measured jets, i.e. **reconstructed jets,** with predicted parton jets, the energy of the former must be corrected to recover the energy of the parent partons. For the same reason, the energy deposited inside the cone by particles associated with the underlying event must be subtracted. In addition, the reconstructed jet is not a massless object. The original parton jet gains mass during the showering and hadronization process. Although the measured jet is considered to be made of massless particles, represented by the calorimeter cells, it has a non–zero invariant mass given by:

$$M_{JET} = \sqrt{E^2 - (E_x, E_y, E_z) \cdot (E_x, E_y, E_z)} \; .$$

In fact, the difference between the jet transverse momentum, measured as:

$$p_T = \sqrt{E_x^2 + E_y^2}$$

and the jet transverse energy is not negligible at low E_T . In average, the difference is of the order of 2% at 30 GeV and vanishes for high E_T jets[51].

TheDØ algorithm merges implicitly when it does the iteration to get the position of the jet centroid and explicitly when it calculates the fraction of shared E_T .

Instead, EKS apply an E_T dependent distance condition. Note that narrow jets are never merged at DØ but they could be merged if EKS's criteria were applied. Jet algorithm and compatibility studies carried out at DØ show that the value of the splitting–merging fraction is not crucial since the fluctuation in the number of jets found is less than 2% for SMF in the range $0.25 - 0.95$ [50]. Furthermore, DØ merging condition and EKS's criteria agree more than 85% of the time in the number of jets found per event for cone size $R = 0.7$ and SMF$= 0.5$ [52, 53].

4.3 Determination of the Event $\not\!\!E_T$

The hermeticity of the DØ calorimeters is a fundamental feature to infer the presence of non–interacting particles. The event missing transverse energy is defined as:

$$\not\!\!E_T = \sqrt{\left(\sum_i E_x^{(i)}\right)^2 + \left(\sum_i E_y^{(i)}\right)^2},$$

where the sum is over all calorimeter cells including the ICD and massless gaps. In a perfect calorimeter, a non–zero $\not\!\!E_T$ indicates there is a neutrino and/or a muon in the event. Neutrinos do not interact within the DØ calorimeters and high P_T muons behave as minimum ionizing particles depositing only $2 - 3$ GeV in the EM modules. In a real calorimeter, the $\not\!\!E_T$ also includes the effect of the noise and the energy and position resolution.

4.4 Monte Carlo Simulations

Monte Carlo Event Generators and Detector Simulator Programs are widely used at DØ to help understand the detector behavior under known conditions. In this section, the description of these programs is limited to the jet physics applications.

4.4.1 Event Generators

ISAJET. The Monte Carlo program called ISAJET[54] simulates pp and $p\overline{p}$ interactions at high energies. It is based on perturbative QCD plus phenomenological models for parton fragmentation. The event is simulated by generating a primary hard scattering. All $2 \rightarrow 2$ processes which involve quarks and gluons are included and the masses for c and lighter quarks are neglected. Higher order processes are included by adding QCD radiative corrections in the leading log approximation both in the initial and final states. Events containing three or more partons are obtained in this way. The cascade process continues until the energy of the partons fall below 6 GeV. At this point, quarks and gluons are fragmented independently into hadrons using the Feynman and Field model[56]. The generation is completed with the addition of "beam jets" resulting from the soft interactions between spectator partons.

HERWIG. Like ISAJET, HERWIG[55] is a general-purpose event generator for high energy hadronic processes. It makes particular emphasis on the detailed simulation of QCD parton showers including color coherence of partons (initial and final) in hard subprocesses, QCD jet evolution with soft gluon interference via angular ordering, backward evolution of initial-state partons including interference and azimuthal correlations within and between jets due to interference.

4.4.2 Detector Simulation

The DØ Monte Carlo simulation program is based on the GEANT package[57] developed at CERN. This package is a tool to simulate detectors by specifying volumes of different materials. It also provides the framework for transporting particles through these volumes including the appropriate interaction processes

involved.

The full structure of supports and individual modules are present in the simulation of the calorimeters. However, the absorber plate–liquid argon structure is replaced by an imaginary material with a suitable effective atomic weight. The real segmentation of the readout cells is imposed, sampling fluctuations are added after showering for each track and the appropriate hadron to electron response is also introduced. The electromagnetic showers evolve until the energy of the particles reach 200 MeV. Below this threshold, the energies are estimated from parametrizations. The energy deposits in the calorimeter cells are summed over all particles and noise is added.

The Shower Library

The full Monte Carlo simulation of hadronic showers, while desirable for realistic evaluation of detector performance, is very time consuming of computer resources. High transverse momentum jet events are particularly slow to generate. The Shower Library method[58, 59] consists of using the full detector and shower simulation only once to make a library of single particle showers. In subsequent simulations, the shower information is read from the library with a great increase in speed.

Obviously, it is not possible to store an infinite number of showers in the library to match every generated particle. Therefore, it is necessary to make the showers depend on a few particle parameters defining a phase space which must be quantized. Five quantities, z-vertex position, η, E_T , particle identity and φ are used in binnings. The particle identity may be electromagnetic (e^-, e^+, γ, π°, η), muon or hadronic.

The agreement between the shower library and full GEANT simulation is excellent[58]. Currently, the library contains more than 1.3 million single particle tracks.

The Test Beam Particle Library

The Test Beam data offer an alternative to the Monte Carlo shower library. A Test Beam Particle Library was developed at DØ [61] to provide experimental shower calorimeter data for electrons and pions in the energy range $2 - 150$ GeV. Figure 4.1 shows the energy distribution out of the calorimeter for incident Test Beam electrons of energies between 2 and 150 GeV. The same information for hadrons is displayed in Figure 4.2. The mean value of the distributions provide an estimate of the energy loss if compared to the energy of the incident particle. The widths of the distributions are estimates of the calorimeter response.

The particle library information is scaled in energy and rotated in space to simulate every condition for particles that enter the calorimeters. Reconstructed jets can be simulated from the Test Beam showers by using their constituents in the particle library.

4.4.3 PJET reconstruction package

PJET[60] is the jet reconstruction package developed at DØ to be used in Monte Carlo simulation studies. A jet algorithm is applied at parton level to reconstruct "generated Parton Jets". This definition is close to the theoretical definitions like EKS and includes all the partons from initial and final state gluon bremsstrahlung and decays. The same algorithm may be used to find "generated Particle Jets", after the hadronization process and before they shower inside the calorimeter.

The program uses a fixed cone type algorithm whose basic parameters are the

cone size R in $\eta - \phi$ space and the minimum transverse energy, E_T, of a jet. The steps in the PJET reconstruction process are the following:

1. The partons or particles are ordered in E_T .

2. The highest E_T parton/particle is used as the center of a cone of radius R and all partons/particles within the cone are included in a candidate jet.

3. The partons/particles included in the candidate jet are removed from the list of available partons/particles.

4. The next highest E_T parton/particle that remains in the list is taken as a new candidate jet. All the partons/particles within a fixed cone of radius R are also included.

5. Steps 3 and 4 are repeated until there are no partons/particles left on the list.

6. Only jets with $E_T > E_T^{min}$ are kept.

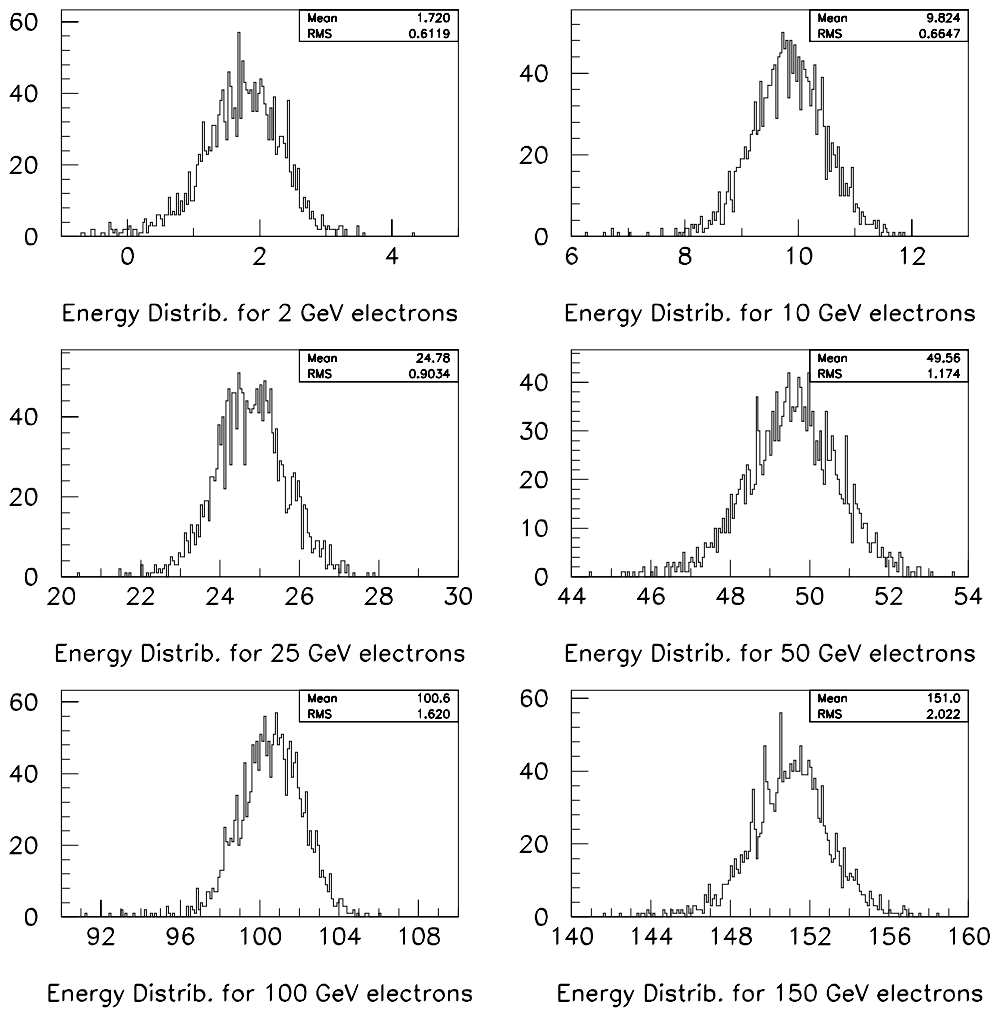

Figure 4.1: Calorimeter energy distributions for monoenergetic incident electrons (Test Beam data).

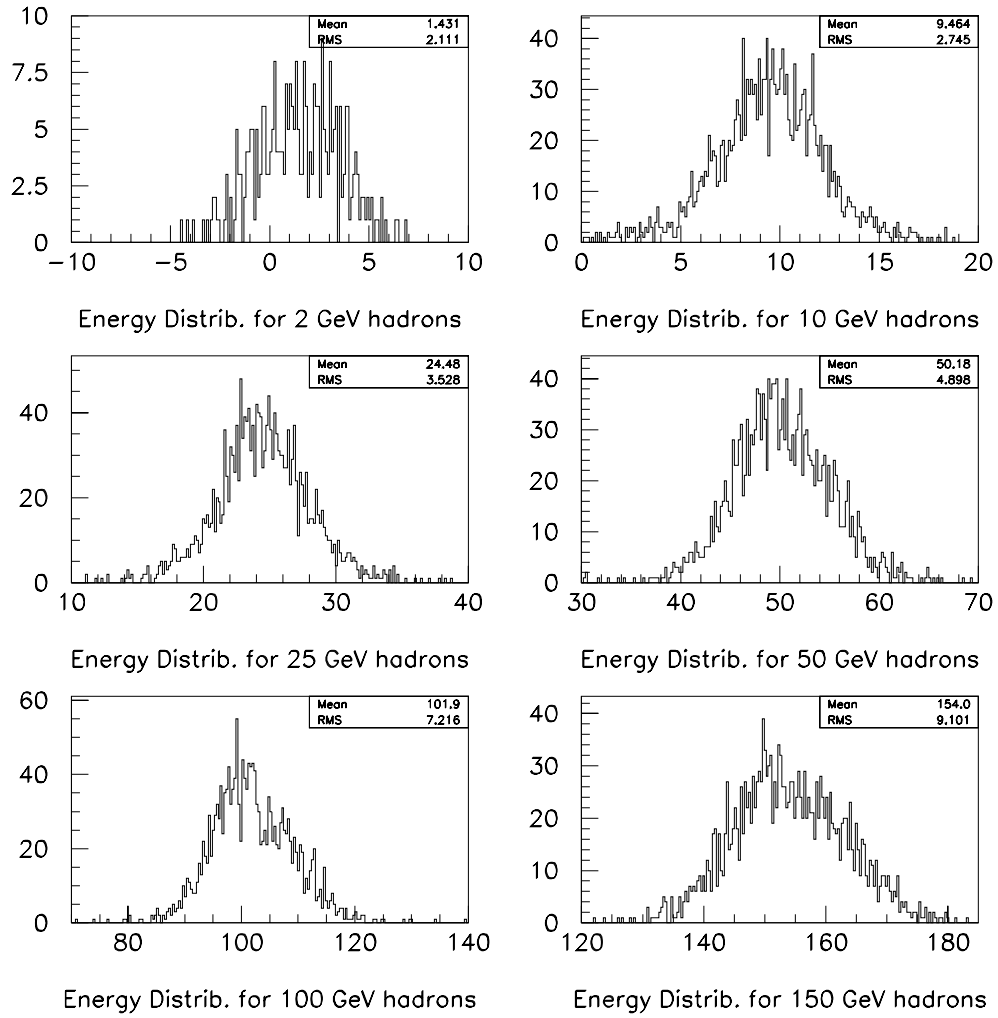

Figure 4.2: Calorimeter energy distributions for monoenergetic incident hadrons (Test Beam data).

4.5 Jet Reconstruction Efficiencies

Jet Finding Efficiency

Sometimes, the jet algorithm does not find a jet. This usually happens to broad and low E_T jets when there is not enough energy in any calorimeter tower to form a seed. In addition, a reconstructed jet is dropped if it falls below the E_T threshold due to calorimeter losses or resolution effects.

Since the inclusive jet cross section is measured for jets with $E_T > 30$ GeV, the reconstruction algorithm must be fully efficient finding jets above this threshold in all pseudo–rapidity regions. This is true in the central calorimeters, where more than 99% of the jets with $E_T > 20$ GeV are found[52, 53]. The ICD and forward regions were tested with a simulation study based on a HERWIG sample of jet events. The events were reconstructed at particle level with the PJET package and at calorimeter level with the same algorithm used in collider data. Assuming that the jet finding efficiency is 100% at particle level, the ratio reconstructed jets over particle jets gives the jet finding efficiency for the fixed cone algorithm. All the jets are counted in the denominator but only the reconstructed jets that match a particle jet are included in the numerator. If a reconstructed jet is within a cone of R= 0.7 around a particle jet, the two jets are matched. If there are two jets within that cone, a smaller cone of R= 0.5 is considered. If there is only one reconstructed jet within the reduced cone, the two jets are matched. If there are two, then the reconstructed jet with E_T closest to the particle jet E_T is selected. If no jet is found within the cone, no match results. Figure 4.3 shows the jet finding efficiency as a function of the PJET E_T . Above 20 GeV, the $R = 0.7$ fixed cone algorithm is fully efficient for all pseudo–rapidities.

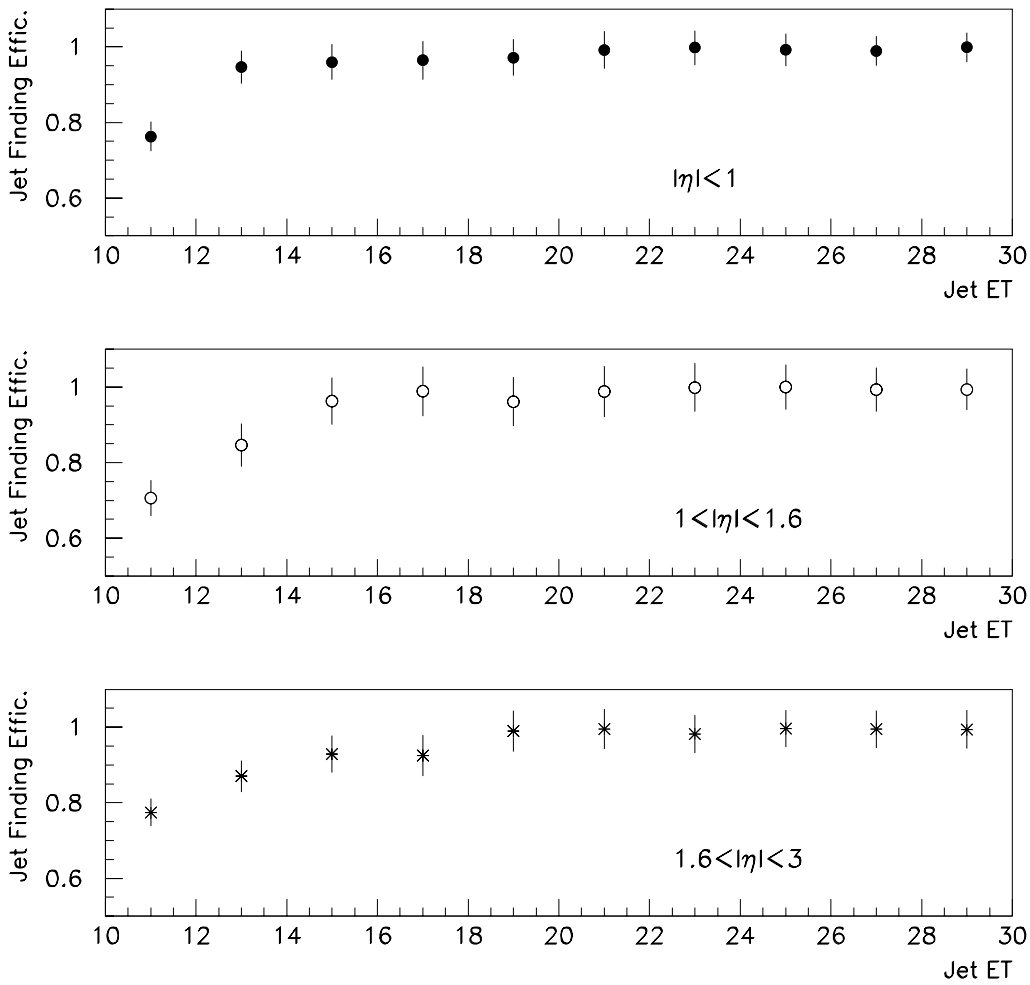

Figure 4.3: Jet finding efficiency for the $R = 0.7$ fixed cone algorithm with (HERWIG simulation).

Energy and Position Determination

The jet energy measured out of the calorimeter is not the actual parton jet energy. A fraction of this energy is deposited in uninstrumented regions, detector cracks, or is leaked outside the cone by particles produced during the calorimeter shower. In addition, the jet E_T spectrum is smeared due to energy resolution effects.

The uncertainty in η and φ is due to reconstruction biases and space resolution. When jets are close to the beam pipe or point to the ICD–massless gaps region, the energy losses due to out of cone effect or poorly instrumented areas distort the η measurement. The bias in the reconstructed jet φ and η is illustrated in Figure 4.4 using a HERWIG simulation of jet events.

Chapter 6 will be devoted to discuss in more detail topics like the jet energy scale, position biases, energy and position resolutions.

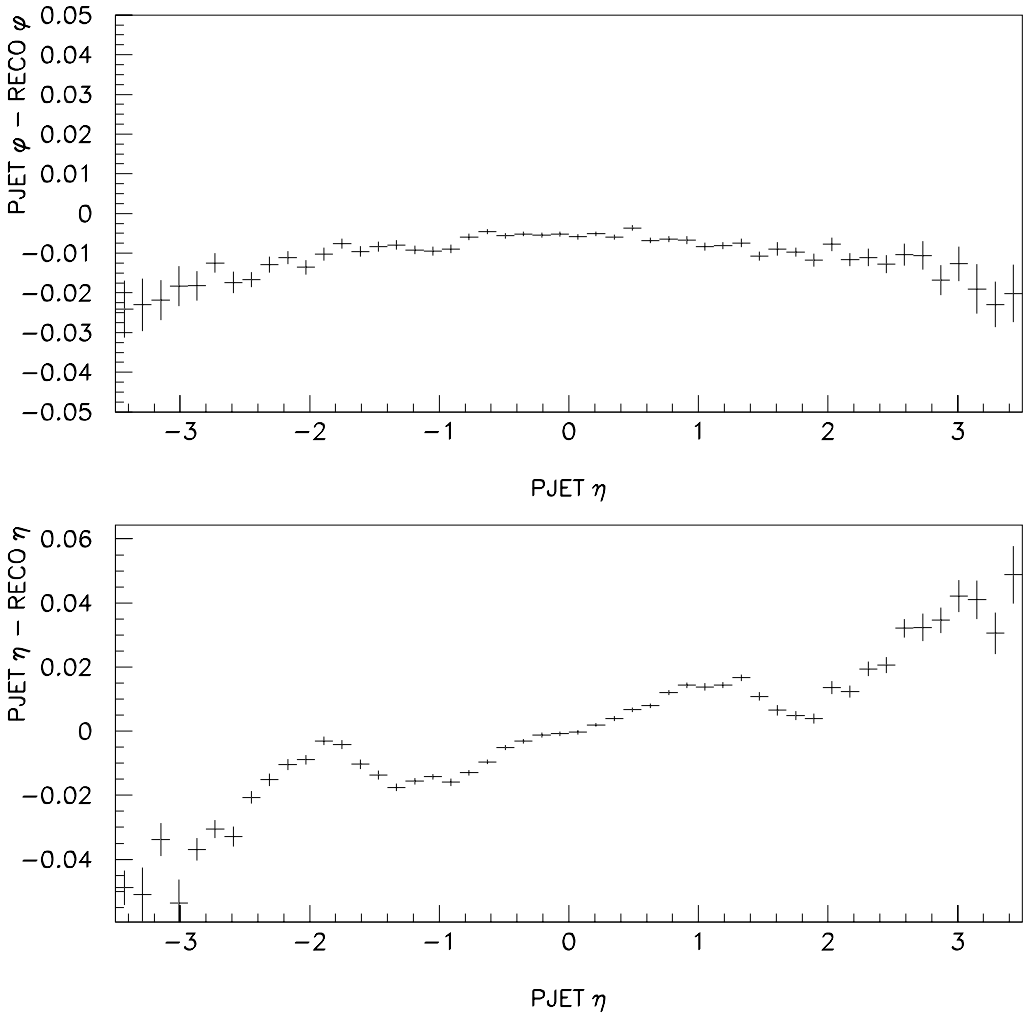

Figure 4.4: Biases in the reconstructed η and φ as a function of the jet pseudo–rapidity (HERWIG events).

Chapter 5

Sample Selection

5.1 Introduction

During run 1A, the accelerator provided $p\overline{p}$ collisions for periods of approximately 20 hours with a duty cycle of 80%. The active period, which is named a store and contains counter rotating beams of protons and anti–protons, is ended periodically due to beam degradation because of low luminosity. The inter–store period is used to prepare a new store and calibrate the detectors. During the active period, the data is arranged in runs or sets of consecutive events with common detector conditions and triggers. A run is ended and a new one started each time a fixed number of events are taken or if a change in the run condition is required.

Jet selection starts at the trigger level. If events passing the jet triggers are accepted, the entire detector is read out, the data recorded and logged to tape. The reconstruction version used for the whole analysis is **RECO–V**10 . In addition, several offline cuts are applied to remove noise and jet background. This chapter describes the jet selection process used in the inclusive jet cross section measurement.

5.2 Jet Triggers

A non–diffractive $p\overline{p}$ collision is an inelastic interaction which results in the breakup of the incoming hadrons into partons. The events of interest for the inclusive jet cross section measurement are those resulting from a parton–parton elastic scattering process. Their signature is jet production.

The jet triggers must handle the event rates as a function of E_T and η to avoid bandwidth saturation and obtain good statistics over the whole spectrum.

Three levels of the DØ trigger system are used online in jet event selection.

- The **Level Ø(LØ)** trigger discriminates non–diffractive events from single–diffractive interactions or soft collisions. The subsample that results from this preliminary selection is called the MINIMUM BIAS (MB) sample. The LØ detector is also used to determine the primary interaction vertex location along the beam direction by timing particles in the beam jets. A cut on the z–coordinate of the primary vertex is applied online at LØ to all the jet triggers except the highest E_T trigger. This requirement, expressed as LØ ($|z| < 10.5$ cm), reduces trigger rates by a factor of $3 - 4$ and selects events which are better measured by the pseudo–projective calorimeters.

- The **Level** 1 **(L**1**)** hardware trigger selects jet candidate events which are reconstructed and tested by the next trigger level. At L1, the E_T of a trigger tower is calculated as:

$$E_T = \sum_i \left[E_T^{EM}(i) + E_T^{FH}(i) \right] ,$$

where the sum is over all the EM and FH cells within the tower i. In run $1A$, the trigger was instrumented for $|\eta| < 3.2$. A jet event fires the level 1 trigger

if the condition JT(n, e) is satisfied. That is, events must contain at least n trigger towers with E_T above threshold e. Level L1 does not introduce dead time since the decision is taken within the 3.5 μs period between crossings.

- The **Level** 2 **(L**2**)** filter performs a fast event reconstruction of the calorimeter regions adjacent to the L1 trigger towers. The jet algorithm uses a fixed cone with size $r = 0.7$; the jets are reconstructed only once with no further iterations involved and no splitting or merging. The event passes L2 if the condition L2JT(n, e, r) is satisfied, where n is the number of jets with E_T greater than threshold e and r is the size of the cone. Computation requires about 200 ms.

Due to computer power and storage limitations, the data to tape was limited to 2 Hz. Only a fraction of this bandwidth was dedicated to jet triggers. As a consequence, the higher rate triggers were heavily prescaled. Table 5.1 describes the jet triggers used in the inclusive jet cross section analysis.

Table 5.1: Description of the jet triggers. The z–vertex position is given in cm and E_T thresholds in GeV. The z–vertex cut is not always applied for JET_HIGH.

Trigger Name	Level Ø	Level 1	Level 2	Prescaled
JET_MIN	MB–LØ(10.5)	JT(1, 3)	L2JT(1, 20)	yes
JET_LOW	MB–LØ(10.5)	JT(1, 7)	L2JT(1, 30)	yes
JET_MEDIUM	MB–LØ(10.5)	JT(2, 7)	L2JT(1, 50)	yes
JET_HIGH	MB–LØ(10.5)	JT(3, 7)	L2JT(1, 85)	yes
JET_MAX	MB	JT(4, 5)	L2JT(1, 115)	no

5.3 Luminosity Measurement

The integrated luminosity L is obtain by integration of the instantaneous luminosity over a period of time. For run 1A, this quantity can be denoted:

$$L = \int^{run\,1A} \mathcal{L} dt$$

The DØ luminosity is obtained by measuring the rate of non–diffractive inelastic collisions. Events are selected by requiring a level Ø coincidence with $|z| < 97$ cm. Scalars count live crossings, coincidences passing the vertex cut, and single hits in groups of similar LØ tiles with and without valid coincidences (see section 3.2.4) The scalers allow the luminosity to be measured independently for each beam bunch and provide feedback to accelerator operations.

The effective cross section of non–diffractive events at $\sqrt{s} = 1.8$ TeV is determined from a combination of results published by the E710 and CDF experiments [62, 63, 64, 65]. It follows that the integrated luminosity is:

$$L(i) = \frac{N(i)}{\sigma_{lum}},$$

where $N(i)$ is the number of non–diffractive events accumulated by the scalars during run i, or the number of MB events if the information from the scalars is not available for a run. The total integrated luminosity for run 1A is the sum over all the runs taken in that period. This quantity has to be corrected to account for LØ detector acceptance, beam contamination, events with multiple interactions and detector dead time

One of the main sources of dead time is due to the Main Ring accelerator which runs through the muon system and the CH modules of the calorimeter. When an 8 GeV p or $\overline{p}$ bunch is injected into the Main Ring, the beam lifetime can be short with subsequent large losses during the first $0.1 - 0.5$ sec. These main ring events fake calorimeter triggers. To avoid this contamination, a process known as blanking [66] is implemented. Each time a proton bunch is injected into the MR, data taking is suspended for $0.1 - 0.5$ s resulting in a 17% dead time. Events are also vetoed or microblanked when the Main Ring beam passes DØ in coincidence with Tevatron beam. This introduces an extra $7-9$ % deadtime. Data acquisition downtimes and high voltage trips are other important sources of dead time.

During run 1A, DØ was able to record 14.9 pb^{-1} out of 27.7 pb^{-1} delivered by the accelerator (see Figure 5.1). Thus, the overall efficiency was 54% and the 12% error in the luminosity determination is mostly due to the uncertainty in σ_{lum}[67, 40].

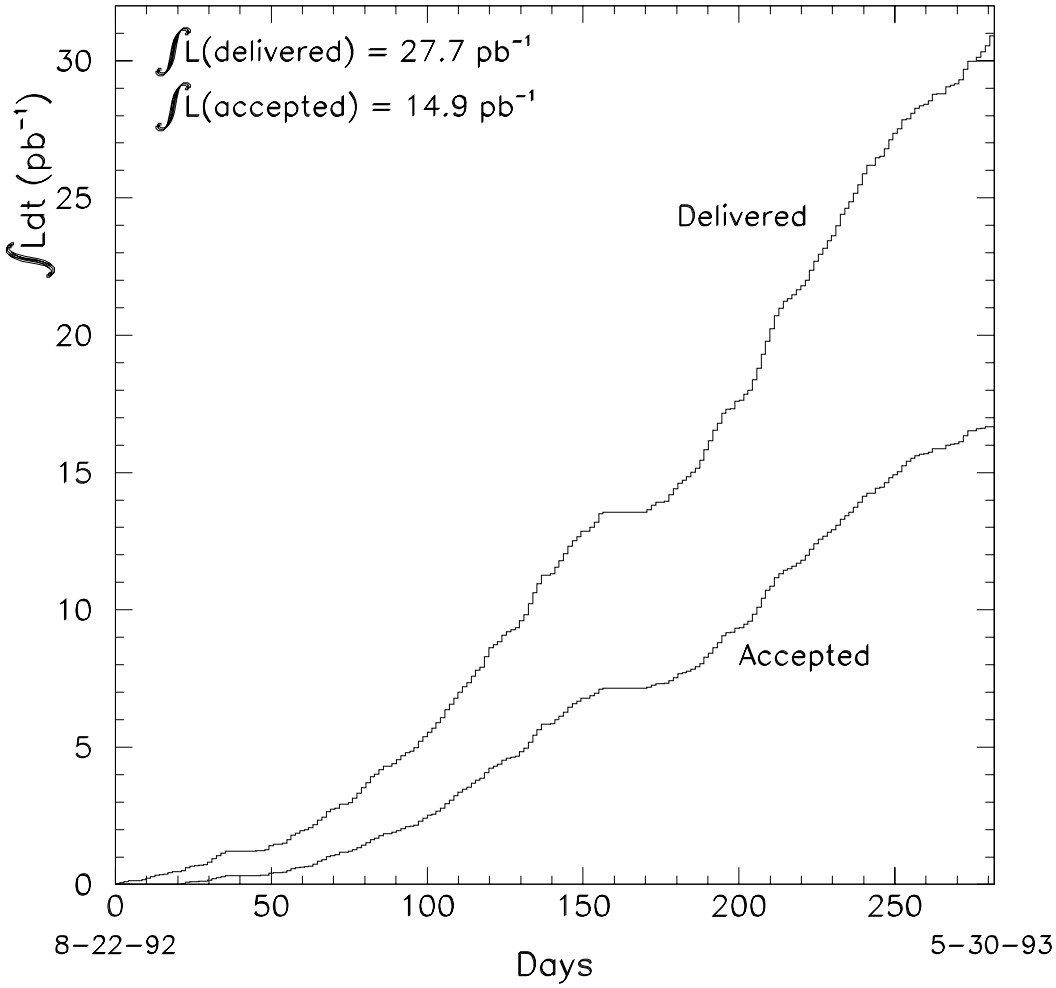

Figure 5.1: Integrated luminosity delivered and recorded by DØ during run 1A.

Effective Trigger Luminosity

The luminosity $L(i)$ must be corrected to account only for those events that are accepted. For each run i and trigger j, the effective luminosity is defined as:

$$L_j^{eff}(i) = \frac{L(i) \times Z_j(i)}{P_j(i)},$$

where Z_j is the fraction of events that pass the LØ (z) condition required by trigger j and P_j is the prescale factor. The effective luminosities of the jet triggers are listed in Table 5.2.

Table 5.2: Total trigger effective luminosities of the sample used in the cross section measurement.

Trigger Name	Eff. Lum. (pb^{-1})
JET_MIN	0.0776 ± 0.0100
JET_LOW	0.735 ± 0.100
JET_MEDIUM	0.98 ± 0.13
JET_HIGH	7.65 ± 1.03
JET_MAX	13.1 ± 1.8

5.4 Jet Selection

A **good quality jet,** or simply a good jet, is an object produced in a parton–parton elastic scattering interaction, which is identified and reconstructed as a jet by the fixed cone algorithm. A good and very energetic three–jet event is observed in Figure 5.2. The existence of spurious energy depositions in the calorimeter cells may either fake a jet or modify a good one. The following are some of the most common sources of noise in the calorimeters.

- **Electronic failures** can make a channel or group of channels shift their

response. The signature of this type of noise is a large energy deposit in a calorimeter cell or group of cells.

- **Cosmic ray showers** can also deposit large amounts of energy in the calorimeters and fake jets. Figure 5.3 shows a cosmic ray event passing through the DØ detector.

- **Accelerator losses** are usually related to main ring activity. These main ring events turn on large regions of the calorimeter faking jet signals. Figures 5.4 and 5.5 illustrate this type of event.

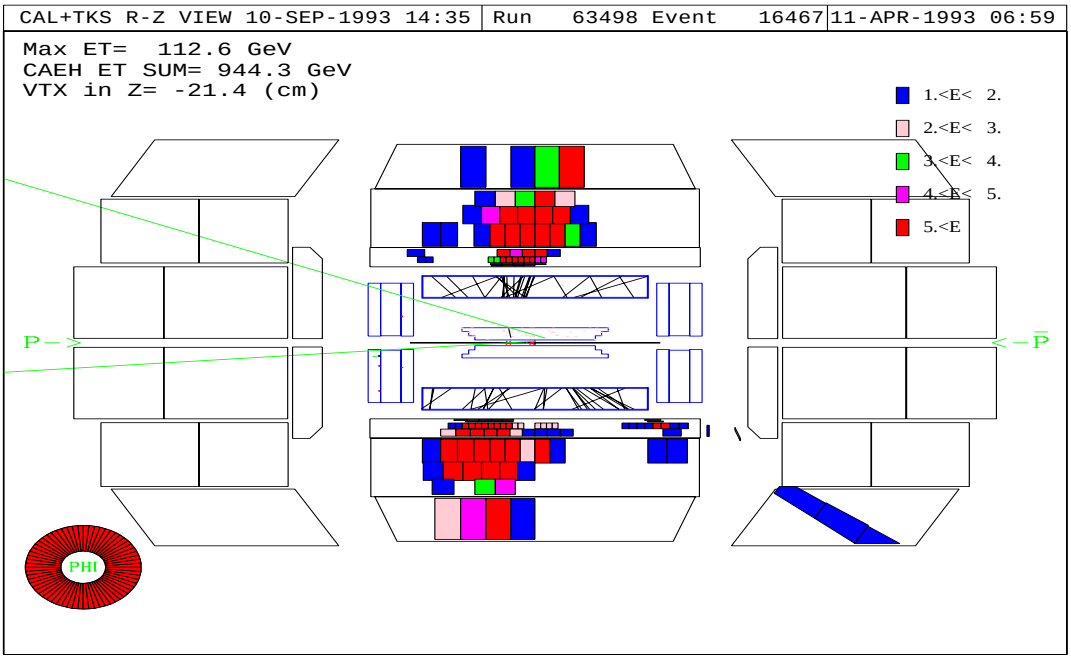

Figure 5.2: Highest E_T three–jet event observed at DØ during run $1A$. The two leading jets have E_T's of the order of 450 GeV

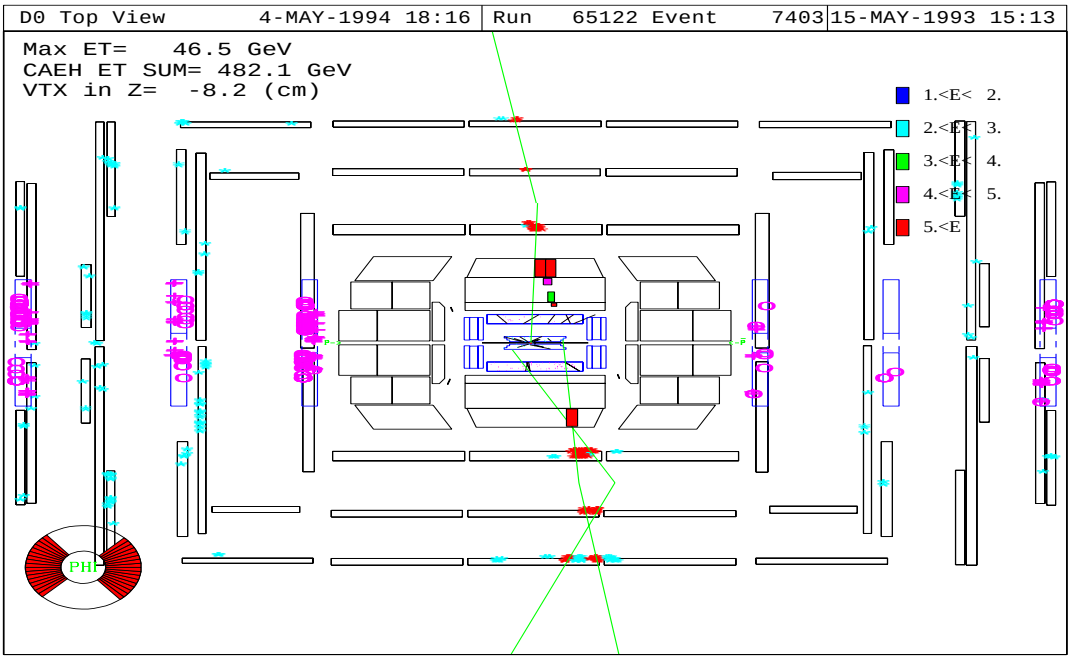

Figure 5.3: Cosmic showers penetrate the detector and deposit large amounts of energy in the calorimeters.

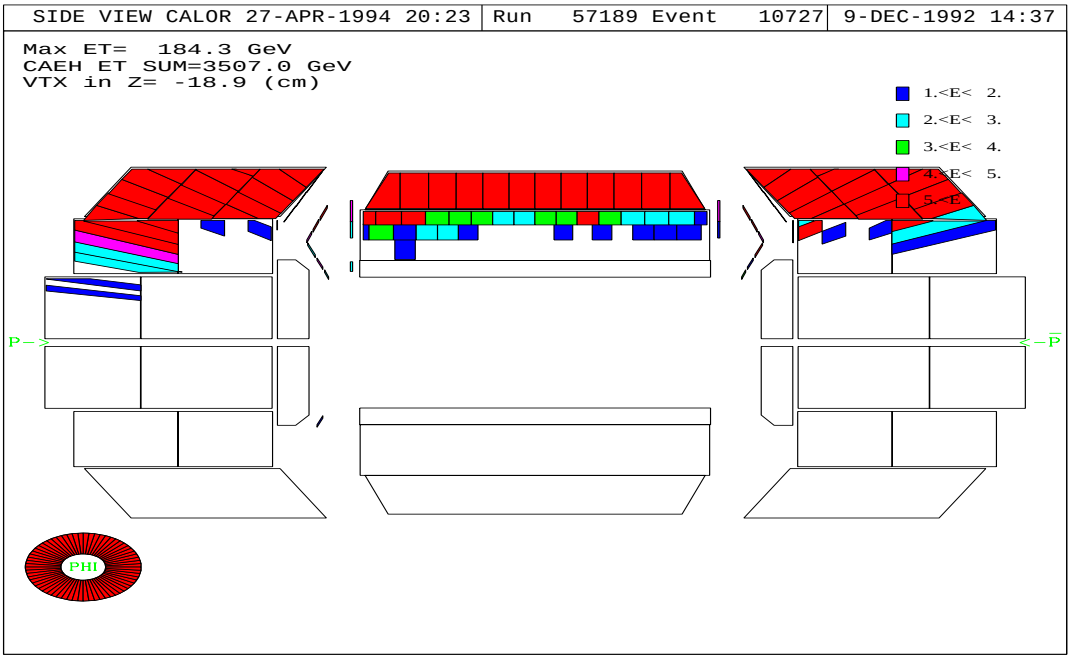

Figure 5.4: The main ring accelerator passes through the CH modules of the DØ calorimeters. Energy is deposited in the whole area during a main ring event.

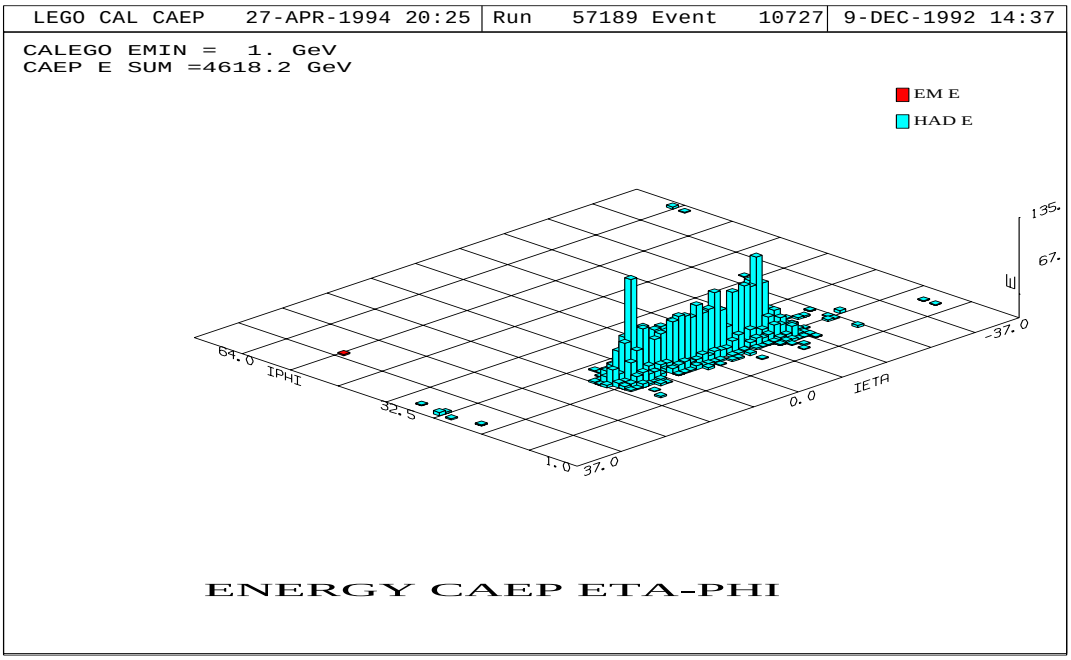

Figure 5.5: The signature of a main ring event is clearly represented in this event display. Large amounts of hadronic energy is deposited along the main ring direction.

5.4.1 Useful Variables for Selecting Jets

A number of jet variables provide discrimination between good and fake jets.

- The jet **Electromagnetic Fraction (EMF)** is the fraction of the total transverse energy deposited in the electromagnetic layers of the calorimeters.
- The jet **Coarse Hadronic Fraction (CHF)** is the fraction of the total transverse energy deposited in the coarse hadronic layers of the calorimeters.
- The **Hot Cell Fraction (HCF)** of the jet is the ratio between the energies of the second most energetic cell and the most energetic one.

The first two variables are very sensitive to fake jets coming from noisy cells. Jets with very low EMF are very likely to be formed by noisy CH or FH cells. If the EMF is very high, the jets are probably associated with noisy EM cells. The CHF is used to flag main ring events which deposit large amounts of energy in the CH cells. The HCF is sensitive to the shape of the jet or the way the energy is spread over the calorimeter cells. While the energy of a fake jet is usually concentrated in a single cell, the energy of a good jet is spread out both longitudinally and transversely over a large number of cells.

5.4.2 Distributions of Selection Variables

EMF Distributions

The EMF distributions are shown in Figure 5.6 for three different detector pseudo–rapidity regions, η_d, and two E_T bins taken from JET_LOW and JET_HIGH. The shapes of the distributions are obviously correlated to the geometry of the detector. Therefore, it is important to distinguish between the physics pseudo–rapidity η

and the detector pseudo–rapidity η_d. The former is measured with respect to the interaction vertex and the later is determined with respect to the geometric center of the detector. Physics η is used for physics analysis but the efficiencies and resolutions depend on η_d.

The EMF distributions are wide and slightly asymmetric gaussians in the central ($|\eta| < 1$) and forward ($2 < |\eta| < 3$) regions centered on <EMF>$= 0.45 - 0.65$ depending on E_T and η_d. The mean value of the distributions moves towards the lower limit for increasing E_T . That means that the high E_T jets tend to deposit a larger fraction of their energy in the hadronic layers. The fake jet contamination associated with noisy cells is mostly confined to the range EMF< 0.05 and EMF> 0.95. The EMF distribution does not provide substantial information in the intercryostat region because the detector lacks EM modules in the range $\eta_d \in [1.2, 1.4]$. As a whole, the EM coverage is very poor for $1 < |\eta_d| < 1.6$. As a consequence, the EMF distribution shifts towards low values, especially for high E_T jets, and the noise at low EMF overlaps with the good jet distribution. Although the noise distribution is expected to be flat as a function of E_T , the noise to signal ratio increases since the jet spectrum falls very fast as a function of E_T .

HCF Distributions

Jets from hard scattering interactions are expected to spread their energy among a large number of calorimeter cells. Thus, it is very unlikely that a good jet deposits more that 90% of its energy in a single cell. Figure 5.7 shows the HCF distributions for different E_T and η_d bins. Fake jet signals are obvious below HCF$= 0.1$.

CHF Distributions

Some of the plots in Figure 5.8 show large concentrations of fake jets above CHF= 0.4. These signals are associated to coarse hadronic noisy cells or main ring events.

Fake Jet Distributions

The fake jet distributions for noise runs, those taken with no colliding beam, are shown in Figure 5.9. In this sample, the jets are all fake. The noise is clearly located below 0.05 and above 0.95 in the EMF distribution. The HCF distribution is mostly concentrated below 0.01.

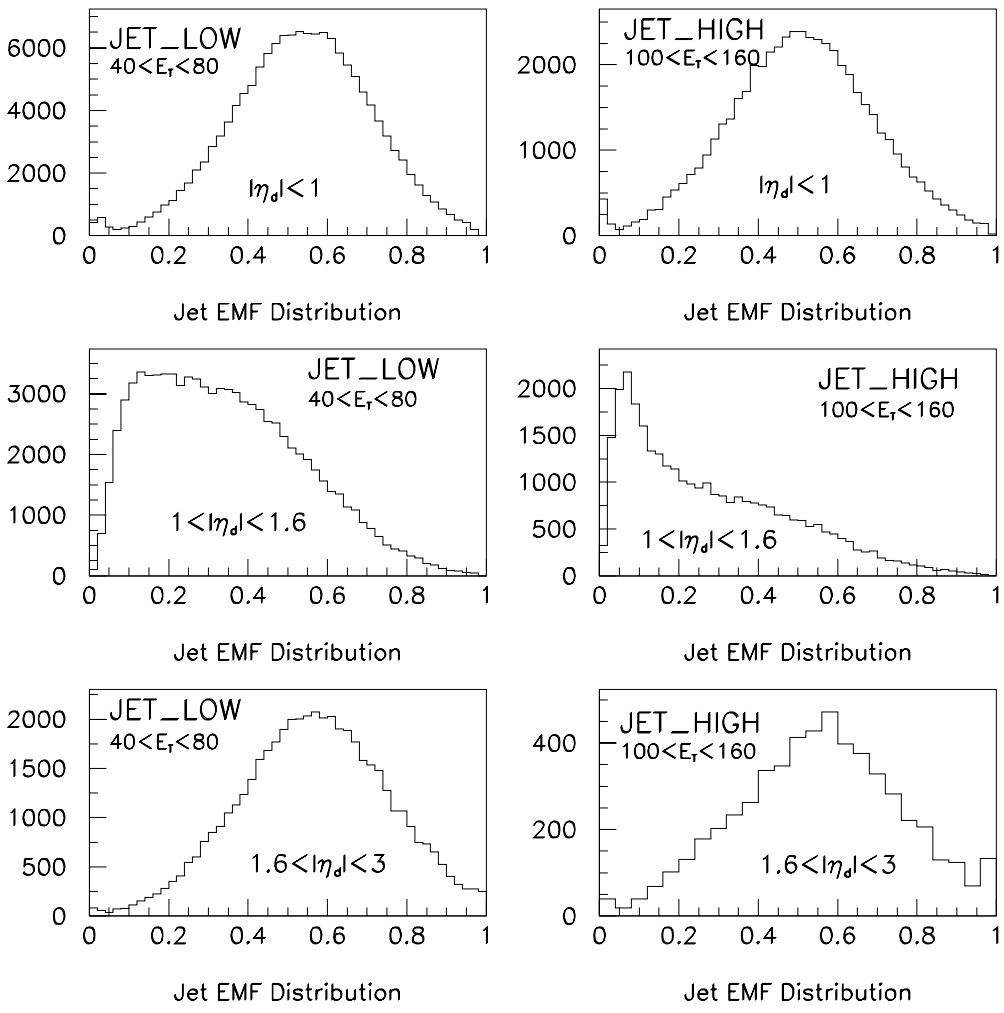

Figure 5.6: Jet EMF distributions for different E_T and η_d bins.

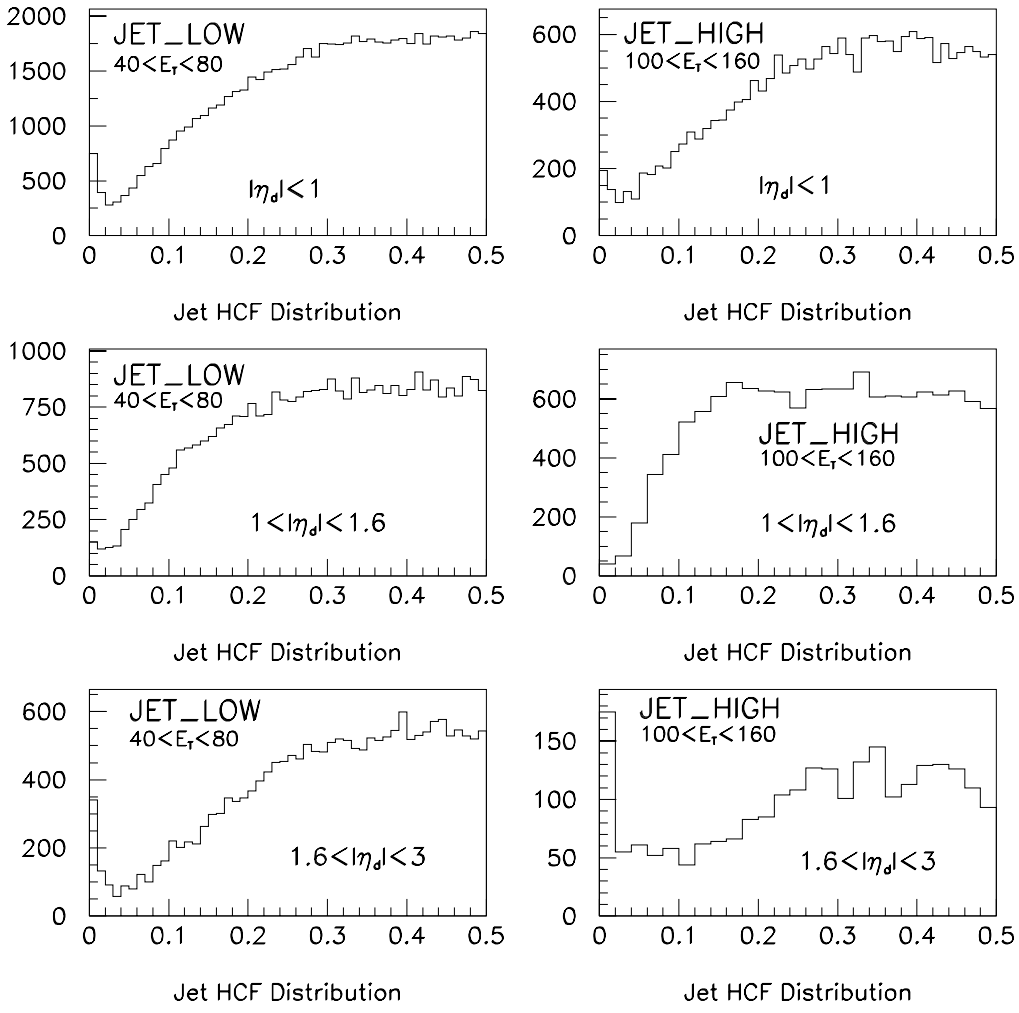

Figure 5.7: Jet HCF distributions for different E_T and η_d bins.

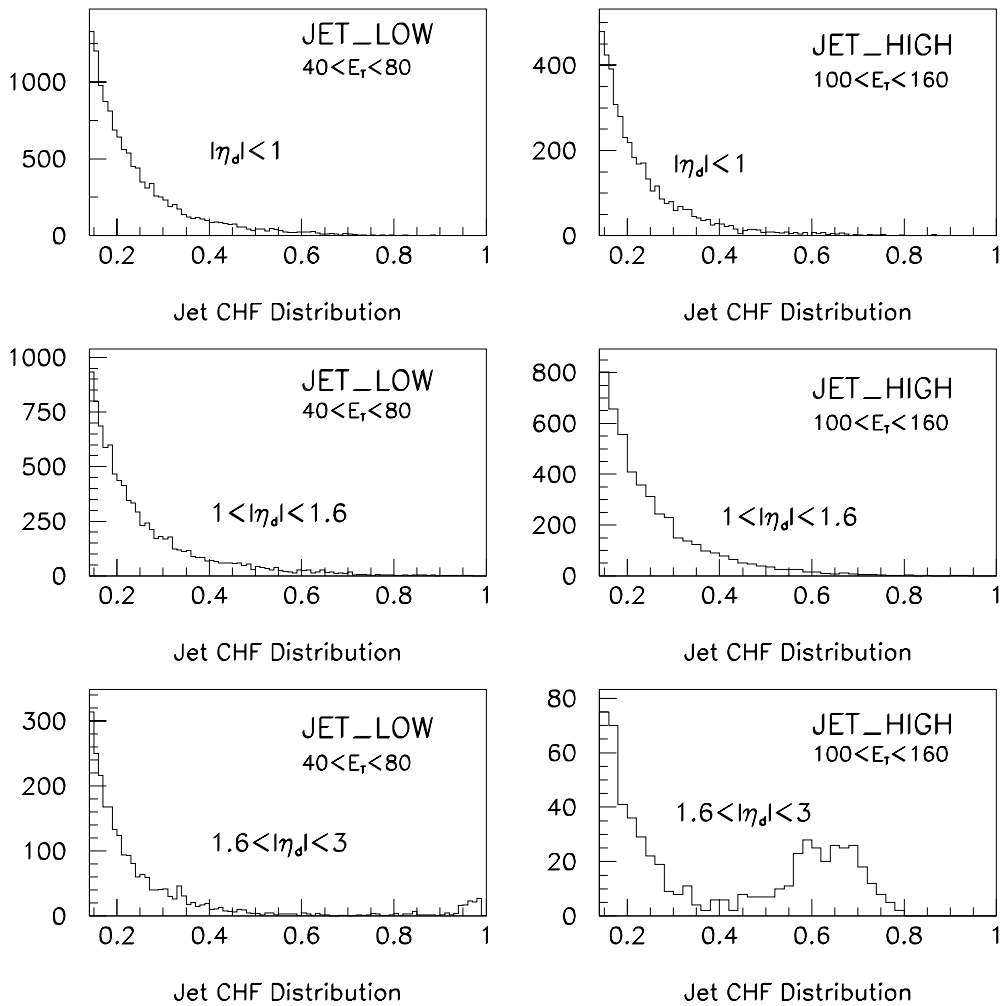

Figure 5.8: Jet CHF distributions for different E_T and η_d bins.

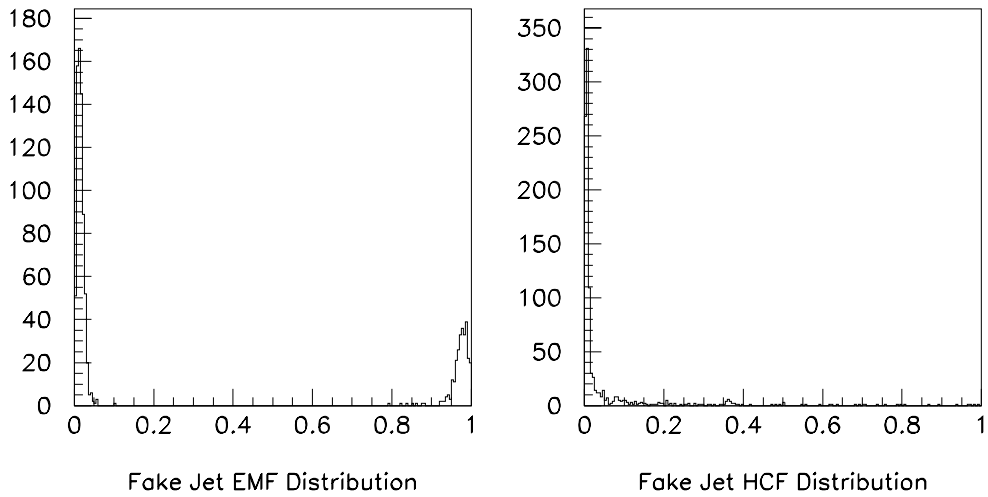

Figure 5.9: Fake jet distributions from noise runs.

5.4.3 Noisy Areas in $\eta_d - \varphi$ Space

The scatter plots included in Figures 5.10 – 5.13 illustrate the position of the jets in $\eta_d - \varphi$ space. These maps are useful to evaluate the overall quality of the calorimeter data, localize different sources of contamination and detect hardware problems. The eight $\eta_d - \varphi$ distributions correspond to eight different E_T bins filled with jet extracted from the five jet triggers.

The two high density horizontal lines observed at $|\eta_d| \in [1.2, 1.4]$ are calibration artifacts. The calorimeters are calibrated using test beam data which provide information to associate an energy value with a cell electronic signal. In the intercryostat region, the energy per ADC count was overestimated producing an artificial shift of the jet cross section towards higher E_T values. The result is a significant increase in the E_T spectrum which vanishes after the energy scale

Table 5.3: Noisy calorimeter regions and their positions in $\eta_d - \varphi$ space.

Region	φ	η_d
1	$(0, 0.2)$	$(0, 0.6)$
2	$(0.45, 0.55)$	$(0.6, 1)$
3	$(0.8, 1.3)$	$(1.8, , 2.3)$
4	$(1.1, 1.5)$	$(-0.2, 0.3)$
5	$(2.8, 3)$	$(-1.5, -1)$
6	$(3.9, 4.1)$	$(-1, -0.8)$
7	$(4.3, 4.5)$	$(0.6, 1)$
8	$(4.7, 4.9)$	$(0.5, 0.9)$
9	$(4.7, 4.8)$	$(2.4, 2.6)$
10	$(5, 5.1)$	$(-0.4, -0.1)$
11	$(5, 5.1)$	$(0.7, 1)$
12	$(5.1, 5.5)$	$(-0.6, -0.2)$

correction is applied. Figure 5.13 shows main ring activity at very high E_T's in the form of a large concentration of fake jets in a narrow window defined by $\varphi \in [1.65, 1.85]$ and $\eta_d \in [-1.4, 1.4]$.

There are more than 10 additional noisy regions that appear at different energies. These are individual cells or groups of cells with unusually high response, which are very likely to be misidentified as jets. The $\eta_d - \varphi$ positions of the regions with highest densities of fake jets are listed in Table 5.3. The noisy areas are also enumerated for further discussion.

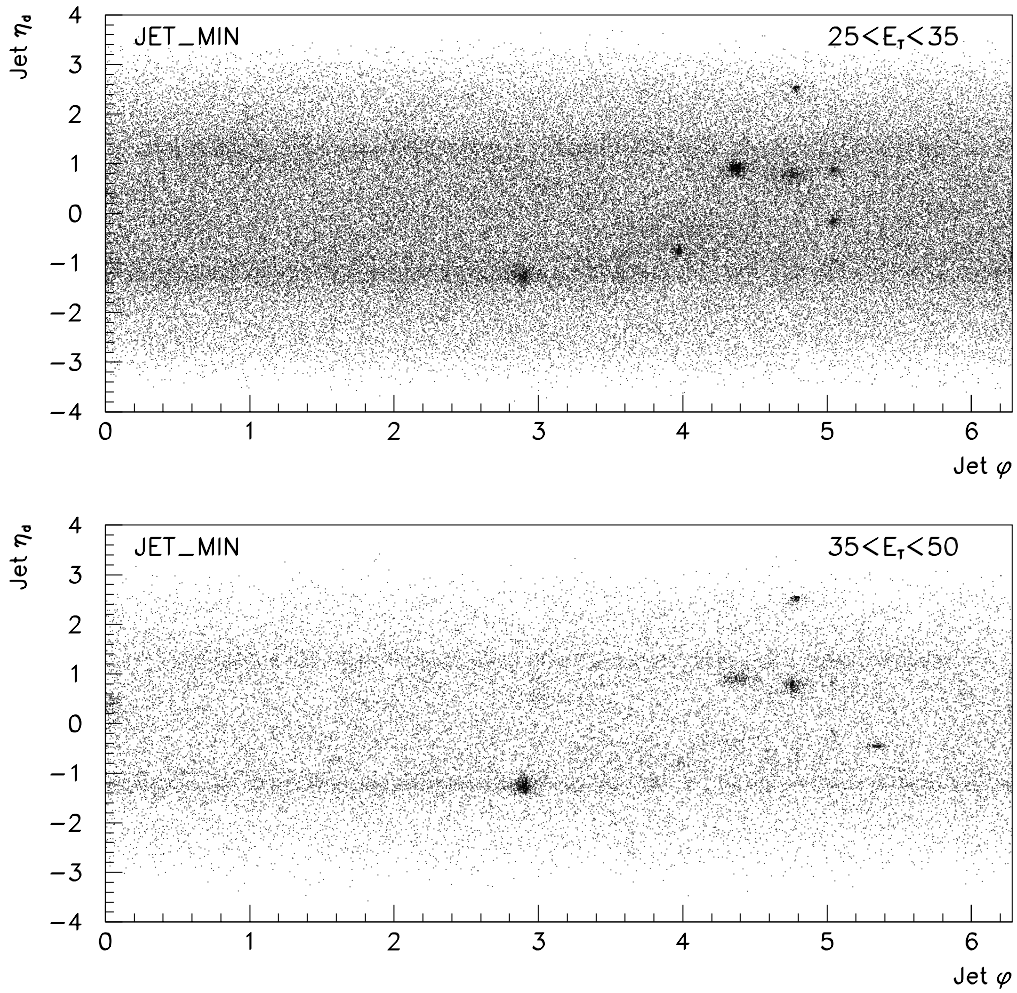

Figure 5.10: $\eta - \varphi$ distributions of jets with $E_T \in [25, 35]$ GeV and $E_T \in [35, 50]$ GeV.

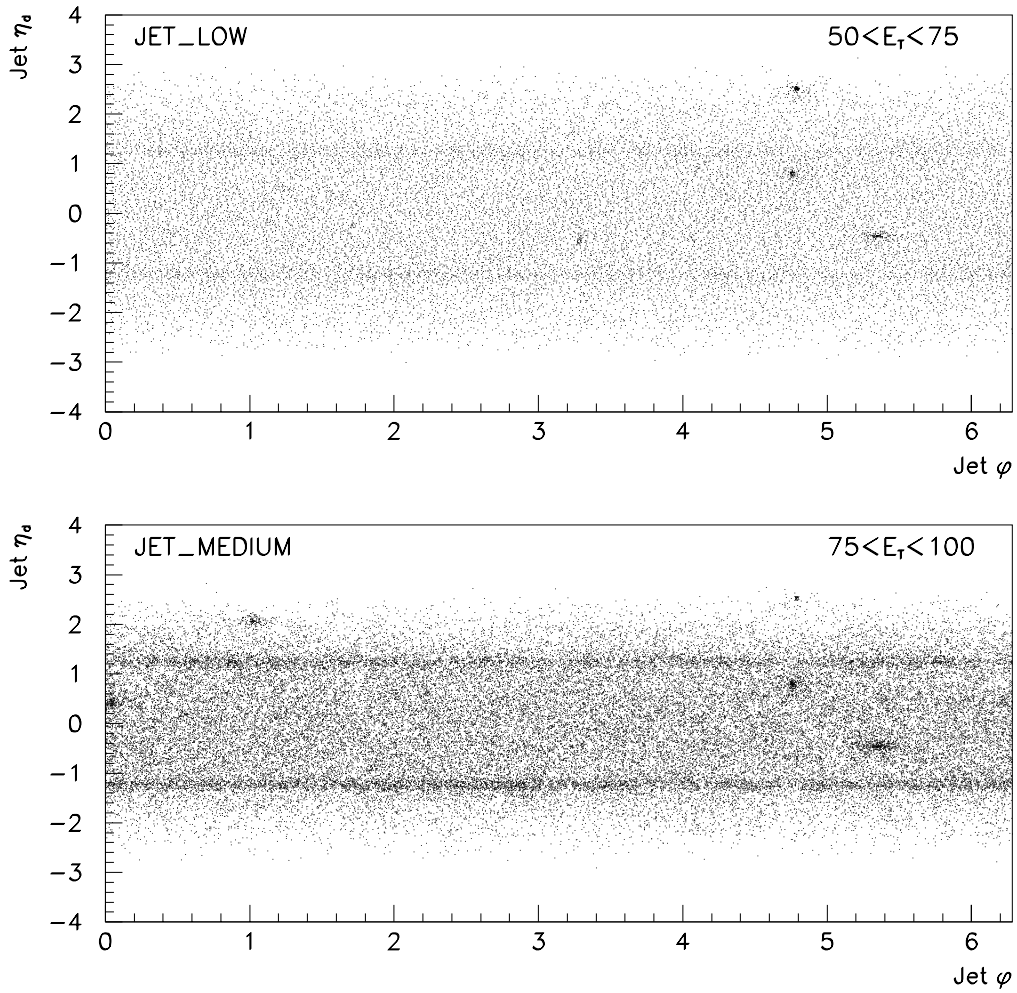

Figure 5.11: $\eta - \varphi$ distributions of jets with $E_T \in [50, 75]$ GeV and $E_T \in [75, 100]$ GeV.

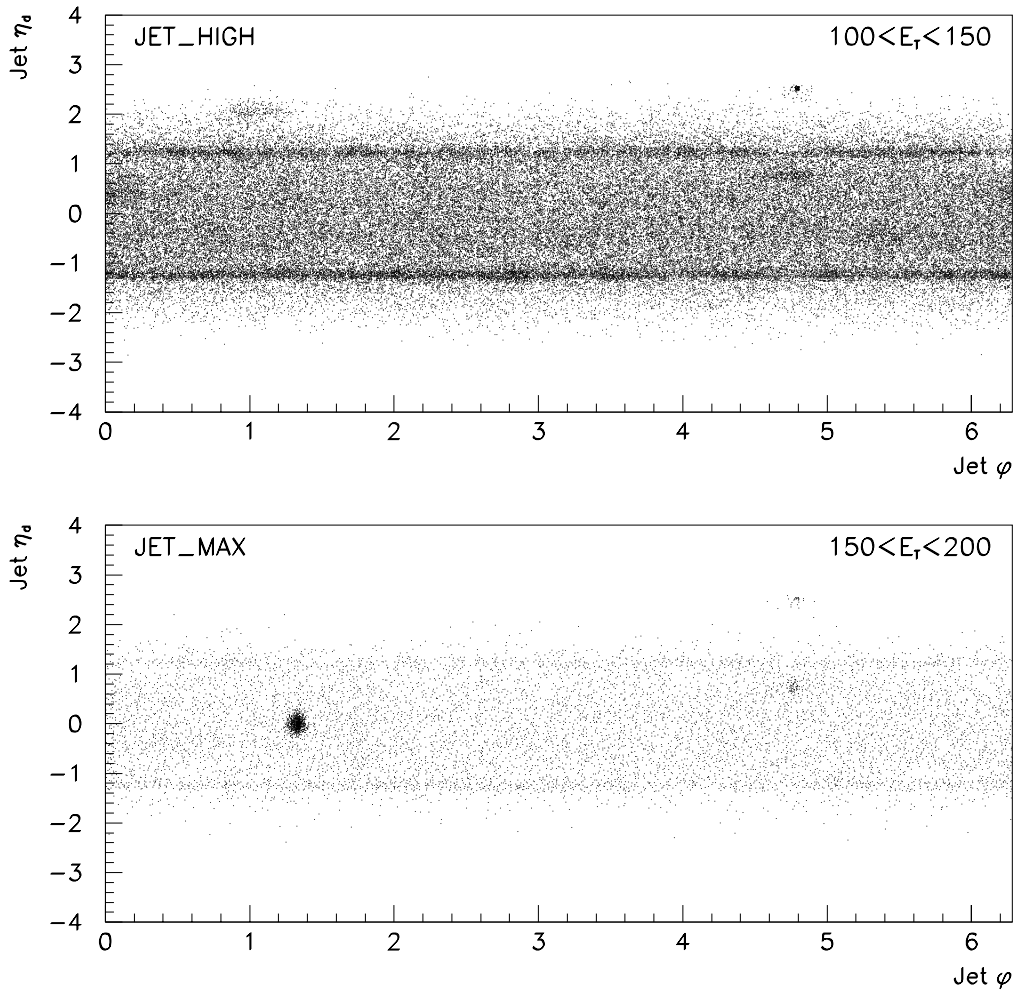

Figure 5.12: $\eta - \varphi$ distributions of jets with $E_T \in [100, 150]$ GeV and $E_T \in [150, 200]$ GeV.

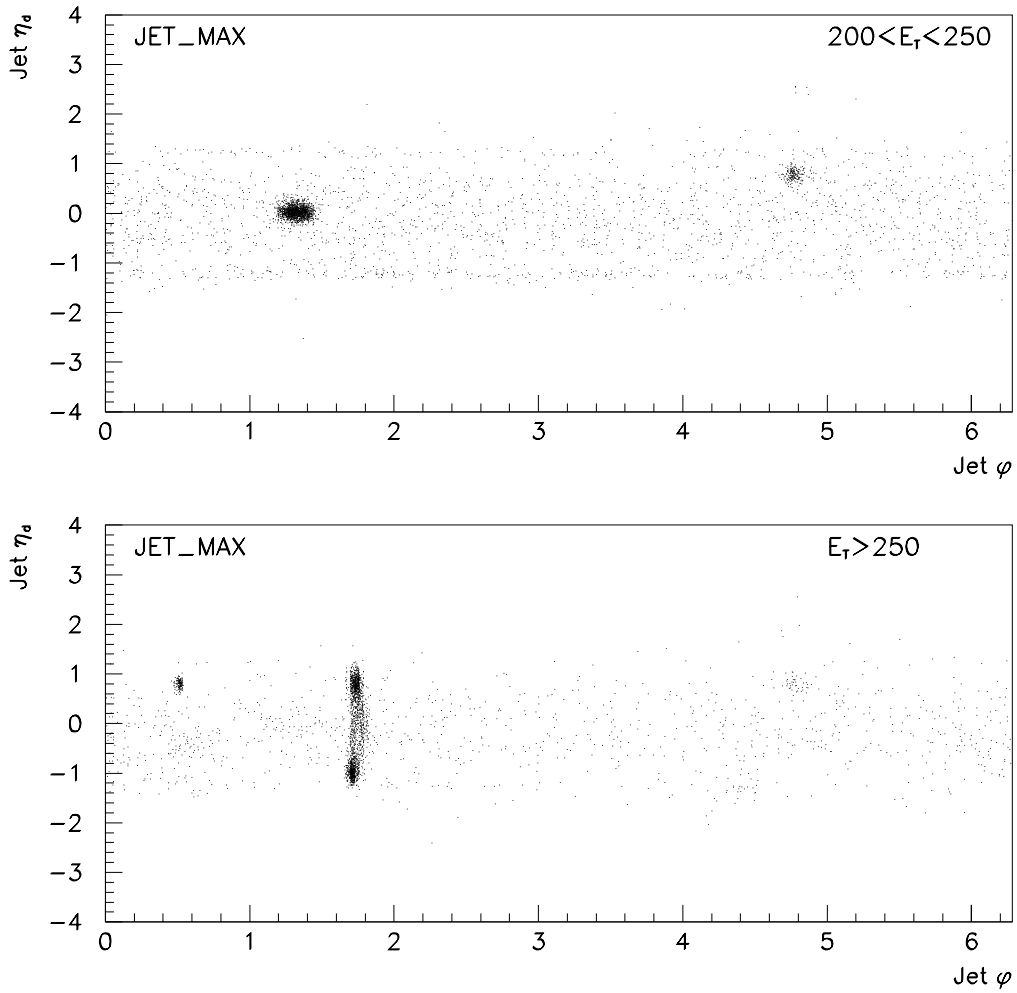

Figure 5.13: $\eta - \varphi$ distributions of jets with $E_T \in [200, 250]$ GeV and $E_T > 250$ GeV.

5.4.4 Standard Jet Cuts

A set of quality cuts, named the standard jet cuts [68], is applied to the jet variables previously described in order to remove fake jets and background. These cuts also remove photons which are reconstructed as narrow electromagnetic jets. In any case, photons are not a background to worry about since the inclusive photon cross section is three orders of magnitude smaller that the inclusive jet cross section. The standard jet cuts are defined as follows:

$$\textbf{EMF} \in [0.05, 0.95]$$

$$\textbf{HCF} > 0.1$$

$$\textbf{CHF} < 0.4$$

The standard cuts are fully applied everywhere except in the IC region. Since this area lacks EM modules, the lower EMF threshold is dropped. Although the noise rejection associated with the standard cuts is excellent, a group of fake jet events with unusual topologies pass the cuts at very high E_T's. Figure 5.14 illustrates the point. The noisy regions identified as 8 and 9 partially survive the standard cuts. They are both associated with two neighboring noisy cells in the massless gaps. The cells form a jet that acquires non–zero EMF when it overlaps a real low E_T jet. In this case, the jet CHF is usually low and the HCF near unity since the two noisy cells have very similar high response. Sometimes the EMF fluctuates above 0.05 and the jet passes the three cuts. The object has an E_T of about 300 GeV and is located in region 8. In addition to the two noisy cells and the low E_T real dijet, a group of noisy EM cells with a total $E_T \approx 150$ GeV form another fake jet that populates

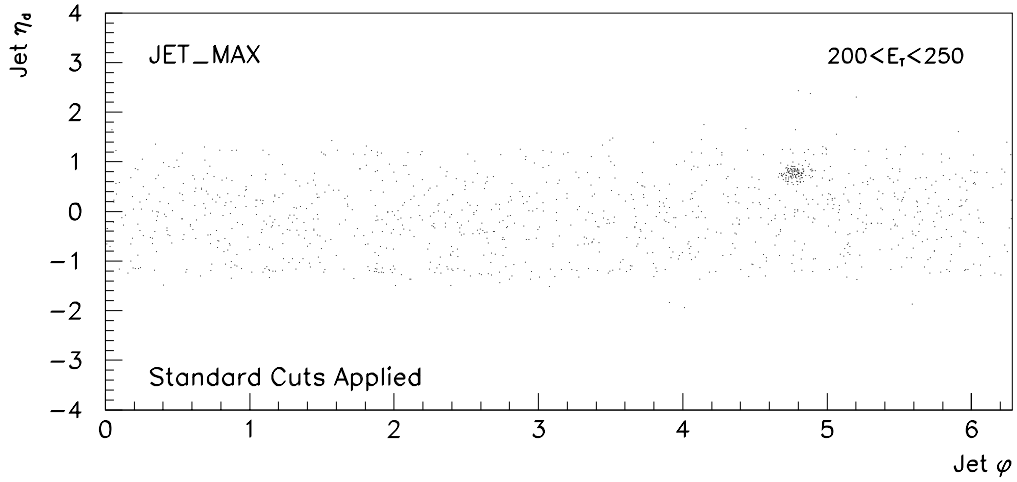

Figure 5.14: $\eta_d - \varphi$ scatter plot of jets with $E_T \in [200, 250]$ GeV after the standard cuts are applied. A group of fake jets survives the cuts in regions 8 and 9.

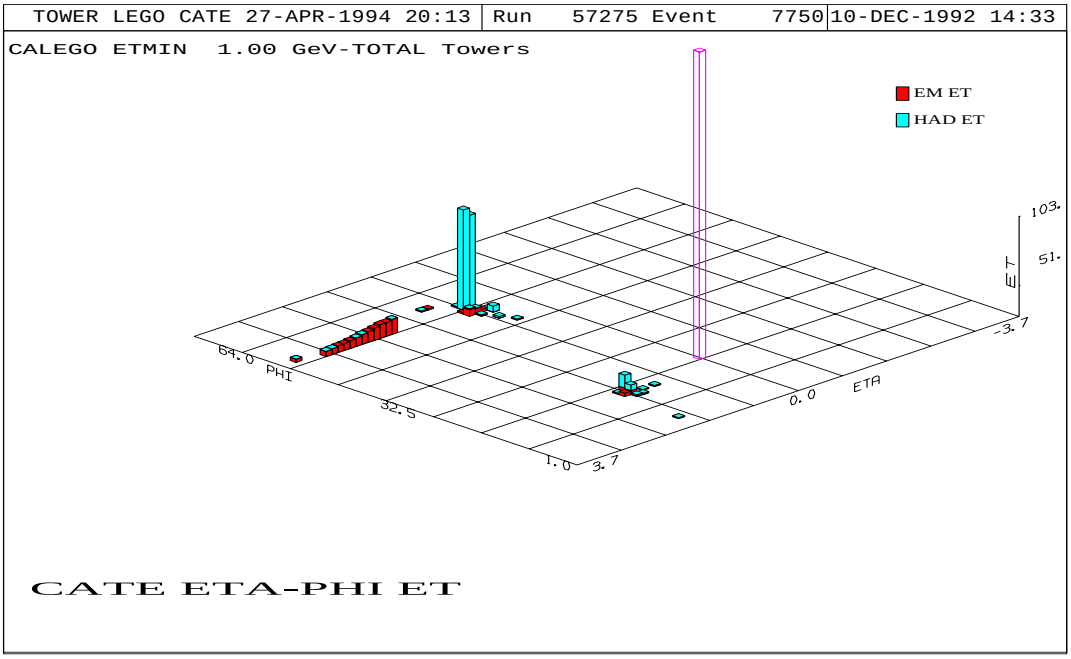

Figure 5.15: Typical multijet event that populates regions 8 and 9. Two neighbor noisy cells in the massless gaps overlap with a real low E_T jet. Sometimes, the object passes the three standard cuts. A group of noisy EMF cells fakes another jet that populates region 9. The tallest column represents the event $\not{E}_T$.

region 9. This object is usually removed by the EMF cut. An example of this type of event is shown in Figure 5.15.

A Cut on the Event $\not\!\!E_T$

A cut based on the $\not\!\!E_T$ of the event is introduced to remove cosmic showers and other unusual fake jet events that survive the standard cuts. By definition, this cut is applied on an event by event basis and relies on momentum conservation in the transverse plane. It cannot be very strict since fluctuations in the jet energy, due to cracks in the calorimeters, out of cone showering, and resolution, may introduce a high $\not\!\!E_T$ into a good dijet event. Therefore, each event is required to satisfy the following condition on the ratio between the $\not\!\!E_T$ and the transverse energy of the leading jet:

$$R_{MTE} = \frac{\not\!\!E_T}{E_T^{jet}} < 0.7$$

which is equivalent to $1/R_{MTE} > 1.43$.

Figure 5.17 (a) is a plot of the leading jet E_T as a function of $1/R_{MTE}$ where the band of noise is clear around $R_{MTE} = 1$. Histogram 5.17 (b) shows that a cut threshold of 1.43 on $1/R_{MTE}$ is large enough to remove most of the noise with good signal efficiency. The threshold does not do a very good job above 200 GeV since a large number of fake events in region 4 pass the cut (see Figures 5.17 (a),(c)). However, it is clear from Figures 5.14 and 5.17 (c) that the standard and R_{MTE} cuts are complementary. The R_{MTE} cut removes the fake jets from areas 8 and 9 and the HCF cut cleans the fake dijet events that populate region 4. For example, Figure 5.16 shows an event triggered by a fine hadronic noisy cell that overlaps a good jet. As a good low E_T dijet is present in the event, R_{MTE} is slightly below

the threshold and the whole event passes. The jet that includes the high E_T noisy cell is removed by the HCF cut.

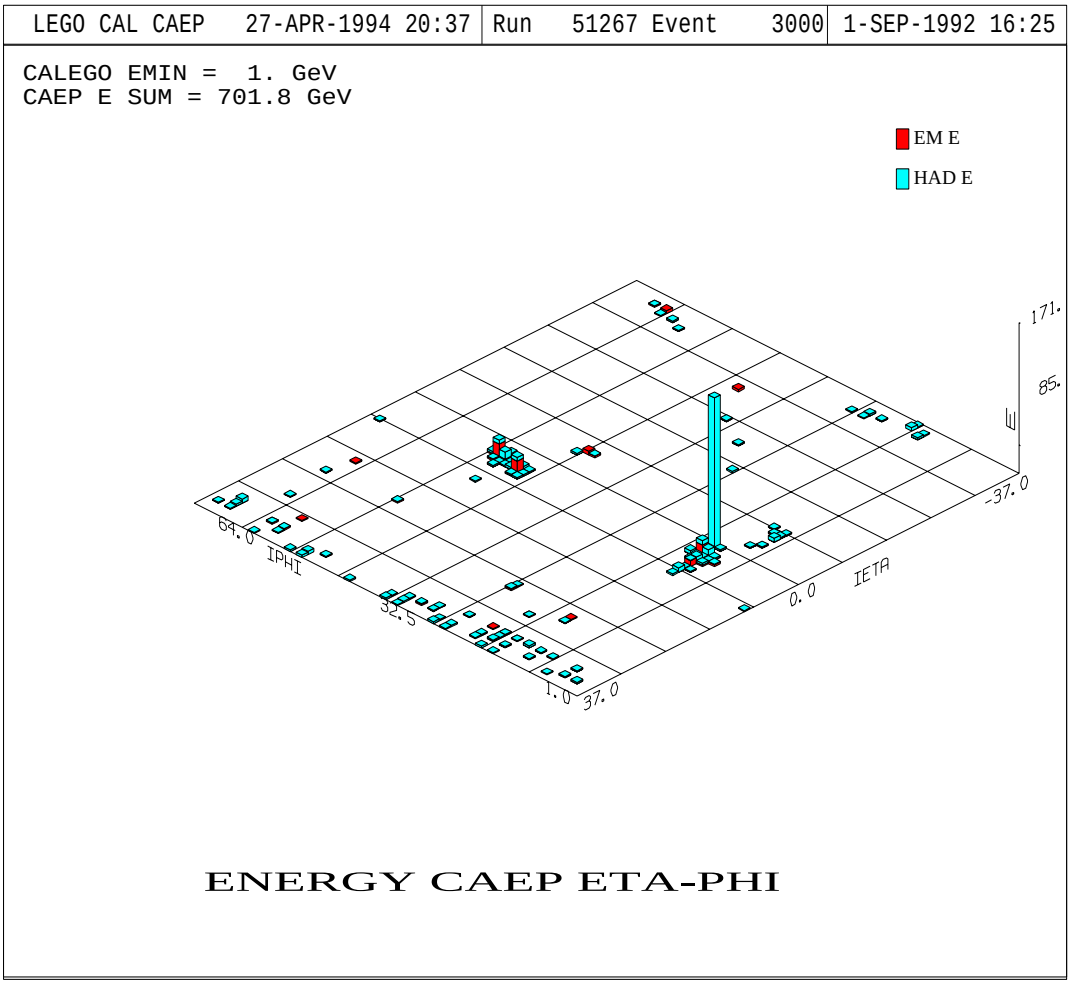

Figure 5.16: A fine hadronic noisy cell superimposed on a low E_T jet forms a jet type object that populates region 4.

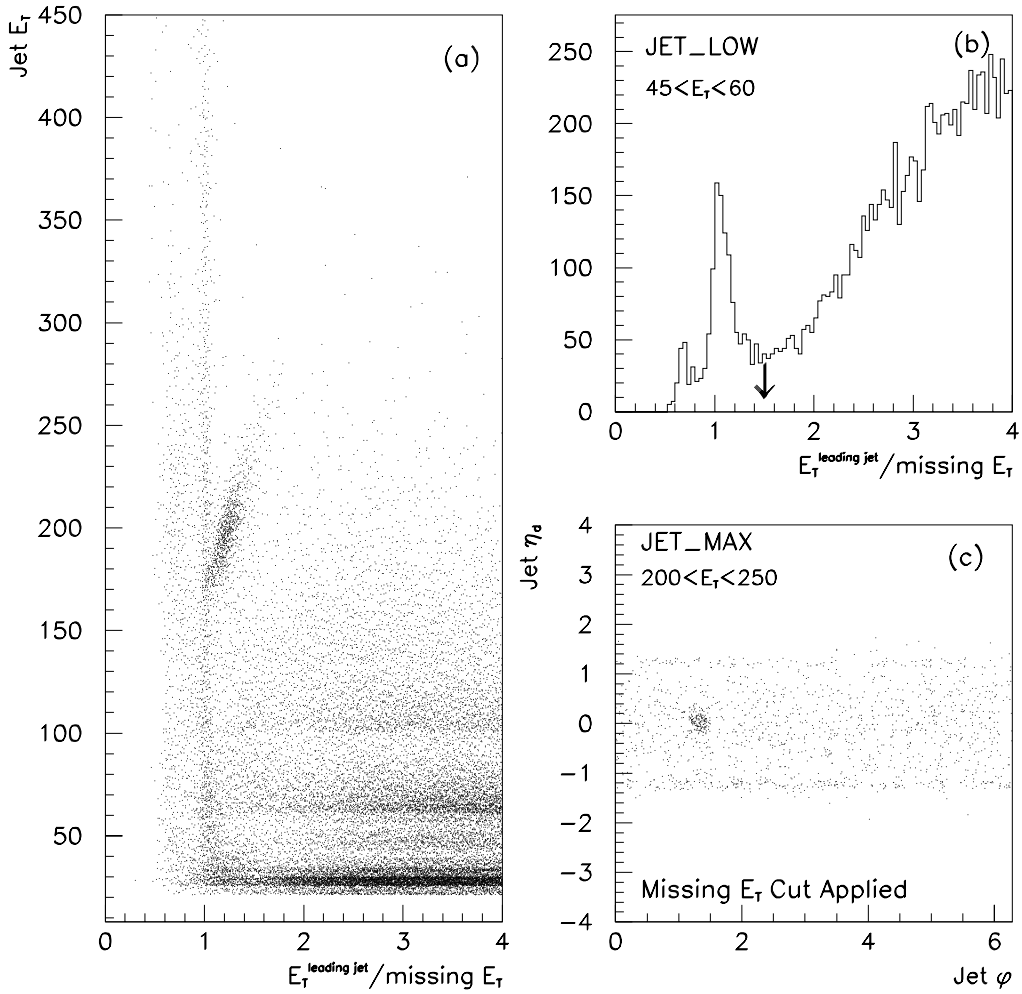

Figure 5.17: (a)–E_T of the leading jet as a function of $1/R_{MTE}$. (b)– $1/R_{MTE}$ distribution for $E_T^{jet} \in [45, 50]$ GeV. (c)– $\eta_d - \varphi$ distribution for jets in the range $E_T \in [200, 250]$ after the R_{MTE} cut is applied.

5.5 Noise Rejection

A run was removed from the list of good quality runs if there was any known problem that could affect the vertex determination from the central detectors or the quality of the calorimeter data. These include general problems like accelerator losses, wrong voltage settings in the calorimeter or central detectors, trigger or data acquisition failures. However, a small number of bad runs and fake jets survived this filter and the jet cuts. The remaining contamination was estimated in different ways.

Noise Runs

Noise runs were taken with no colliding beam. Obviously, all the reconstructed jets in this sample are fake. The jet standard cuts remove 99% of these jets [68]. This is only a rough estimate of the fake jet rejection since the noise spectrum in the jet cross section sample may not be well represented by the noise runs for they only include a few thousand events taken over a very short period of time.

Monte Carlo Simulation

The effect of noisy cells on the inclusive jet cross section was investigated with a Monte Carlo simulation[69]. It consisted of corrupting a fraction of Monte Carlo events with a noisy cell randomly distributed in $\eta - \varphi$ space. The spurious cell can modify an existing jet or generate a new one. For collider data, the percentage of good events with fake jets is $\approx 15\%$ and it is independent of the leading jet E_T . Therefore, 15% of the Monte Carlo events with a leading jet above $E_T^{Min} = 8$ GeV were corrupted by adding noisy cells with $E_T > 2$ GeV consistent with an estimated noise cross section. When the standard jet cuts were applied, the

corrupted jet cross section agreed within 1% with the uncorrupted cross section below 450 GeV.

Jet Occupancy in Noisy Regions

Most fake jets are removed from the noisy regions by the jet cuts. However, small numbers of fake jets will remain in the sample. A statistically based method [70] was used to localize and estimate the effect of runs that contribute most to contamination after the jet cuts were applied.

After the quality cuts are applied, the jet occupancy x_i^{run} is defined as:

$$x_i^{run} = \frac{N_i^{run}}{N_{tot}^{run}}$$

where N_i^{run} is the number of jets in $\eta_d - \varphi$ region i and N_{tot}^{run} is the total number of jets in the sample. The statistical error associated with this quantity is given by:

$$\Delta x_i^{run} = \frac{\sqrt{1 - \frac{N_i^{run}}{N_{tot}^{run}}}}{N_{tot}^{run}}$$

Ideally, if there was no contamination in the sample and the number of jets per run tended to infinite, x_i would be the same for every run. In reality, each run deviates from the mean due to statistical fluctuations and contamination. Then, the jet occupancy is represented by a gaussian distribution with a mean, μ_i, and a variance, σ_i. The significant deviation, defined as

$$\lambda_i^{run} = \left(\frac{x_i^{run} - \mu_i}{\Delta x_i^{run}} \right)^2 ,$$

is independent of statistical fluctuations and becomes a useful quantity to detect the runs that deviate from the mean due to contamination. If there was not noise

in the sample, λ_i^{run} would be a narrow distribution that peaks near zero. The deviation to higher values may be used as a measure of the level of contamination of the run in the region. Figure 5.18 (a) , (b) shows the x_i^{run} and λ_i^{run} distributions for region 8. The significant deviation is plotted again in Figure 5.18 (c) for $x_i > \mu_i + 2\sigma_i$. The process is repeated in a clean region, named control region $8C$, with the same area in $\eta - \varepsilon$ space and the same average x_i. The result can be observed in Figure 5.18. From a comparison between plots (c) and (f), it seems natural that runs with $\lambda_8 > 5$ remain noisy in region 8.

A list of noisy runs with $x_i > \mu_i + 2\sigma_i$ and $\lambda_i > 5$ is produced for each noisy region. The inclusive differential jet cross section is obtained for the central, intercryostat and forward η regions, redefined as CT: $|\eta| < 0.9$, IC: $1 < |\eta| < 2$ and FW: $2 < |\eta| < 3$, both including and removing the runs in the lists. The data removed for this test correspond to $1 - 2$ pb^{-1} depending on the pseudorapidity region. The ratios R_{CT}, R_{IC}, R_{FW} between the cross sections measured from the clean sample and the cross sections from the whole sample are shown in Figure 5.19. In all cases, the jet quality cuts are applied.

The contamination that remains in the IC and FW regions is within statistical errors. In the CT region, for E_T's below 150 GeV, the noise accounts for 3% of the measured inclusive jet cross-section.

The jet quality cuts also remove a fraction of the good jets. On average, the efficiency of the standard jet cuts plus the R_{MTE} is $\approx 96\%$. The dependence of these efficiencies on the jet E_T and η and the corrections applied to the inclusive jet cross sections are discussed in chapter 6.

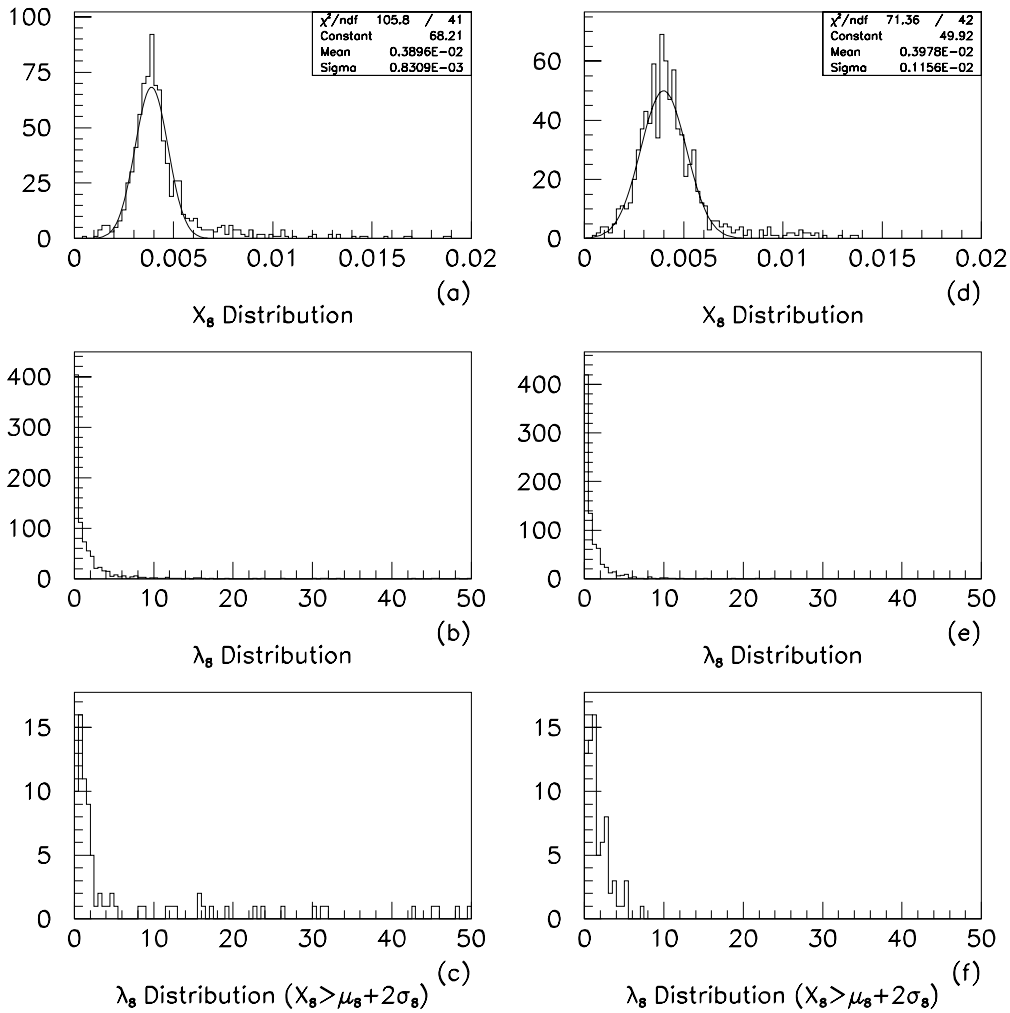

Figure 5.18: (a),(b),(c)–Jet occupancy, x_8, and significant deviation, λ_8, in region 8. Plots (d),(e),(f) correspond to a clean control region $8C$ with the same average x.

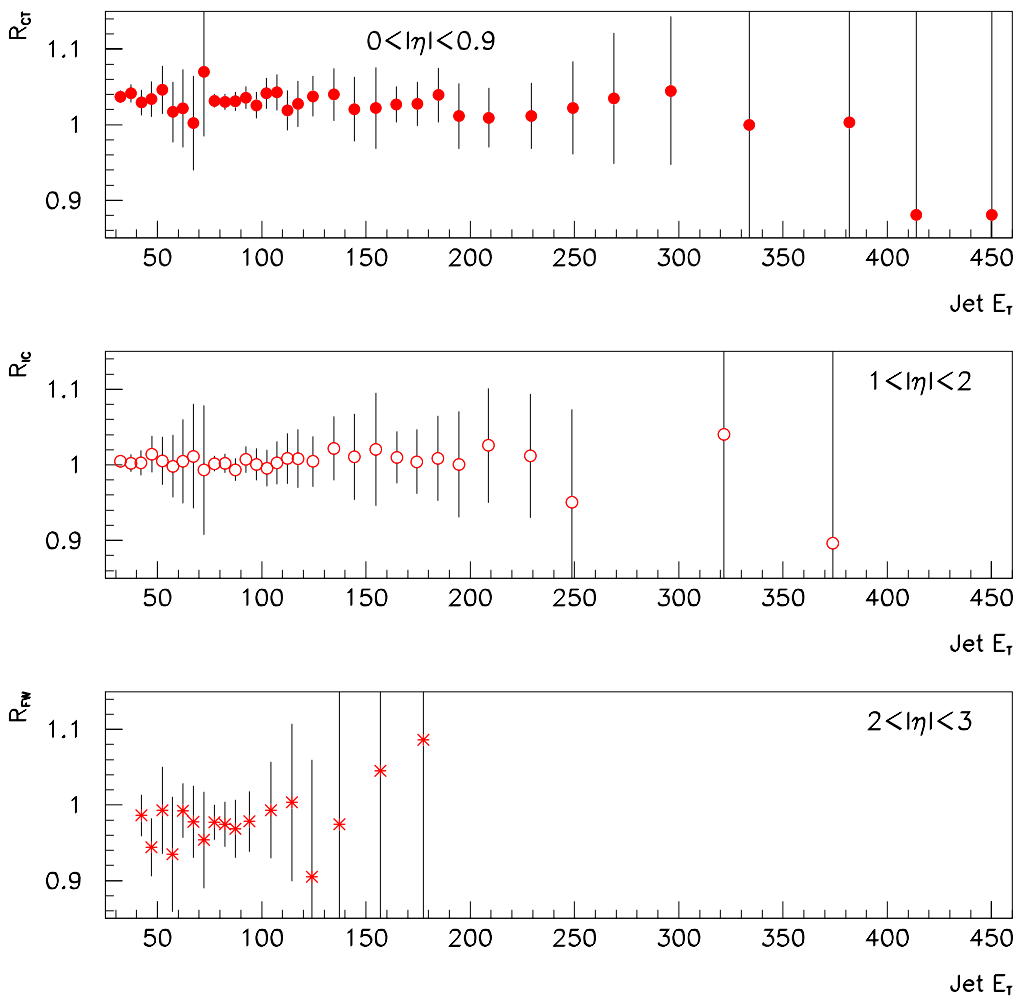

Figure 5.19: Inclusive jet cross section ratios R for the CT, IC and FW pseudo-rapidity regions. The cross section in the numerator is calculated with a reduced sample of clean runs. The denominator uses the whole sample. The jet quality cuts are applied in both cases.

5.6 Event Scanning Consistency Check

As a consistency check, the highest E_T jet events that passed the standard cuts were scanned to detect fake jets in the final sample[71, 72]. The good events satisfy the following requirements:

- At least two jets with well contained energy depositions in the calorimeter.
- No intense firing of the muon chambers which would be a signal for cosmic rays.
- No isolated cells with large energy depositions.

Table 5.4: Events with jets that passed the standard cuts, with E_T's above a threshold ε, were scanned as a consistency check for the noise rejection and good jet efficiency studies. One good event failed the R_{MTE} cut and two bad events passed the cut.

η region	ε (GeV)	good (failed)	bad (passed)
CT1: $\|\eta\| < 0.5$	280	0	1
CT2: $0.5 < \|\eta\| < 1$	280	0	0
IC1: $1 < \|\eta\| < 1.5$	250	0	0
IC2: $1.5 < \|\eta\| < 2$	200	0	1
FW1: $2 < \|\eta\| < 2.5$	130	1	0
FW2: $2.5 < \|\eta\| < 3$	85	0	0

Table 5.4 contains the scanning information. The two bad events which passed the R_{MTE} cut were removed from the sample. They are run 57607 event 5180 and run 63285 event 3490. The first one contains a fake jet reconstructed from electronic noise and the second is a cosmic ray. There is one good event which did not pass the R_{MTE} cut. It is run 58556 event 11686 and did not pass due to

the poor resolution in the IC region. It was not included in the sample since the cross sections were corrected for cut inefficiencies.

Chapter 6

Corrections to Jet Quantities

This chapter describes the corrections applied to the measured jet variables and how detector effects are removed to allow the experimental results to be compared to theoretical predictions. The contribution of every possible source of error is considered in order to determine the total systematic uncertainty associated with the inclusive jet cross section measurement.

6.1 Jet Trigger Efficiency Determination

Several detector and trigger imperfections contribute to trigger inefficiencies.The CH layers of the calorimeter, the massless gaps and the intercryostat detector are not included in the L1 decision. Furthermore, there are smearing effects related to the vertex measurement at LØ and the jet energy resolution. A combination of these effects distorts the jet E_T measured at L1 and L2 in such a way that it may fall below the trigger thresholds. As a function of η_d, the trigger efficiency dips in the intercryostat region and above $|\eta_d| = 2.8$ since the trigger was instrumented for $|\eta_d| < 3.2$.

Definitions and Method

In reference [52, 73], jet trigger efficiency and event trigger efficiency are defined in a convenient way which is appropriate for correcting the inclusive jet cross sections. The **jet event trigger efficiency** is the probability that an event which contains a jet of a particular E_T and η_d satisfies the trigger condition. Instead, the **jet trigger efficiency** is the probability that a jet with a particular E_T and η_d satisfies by itself the trigger condition.

The relative event efficiency of trigger B with respect to the less restrictive trigger A is calculated in reference[73] using collider data as follows:

- Only the two leading jets passing the standard cuts are used.
- $N(\Delta E_T, \Delta\eta_d, A)$ is defined as the number of jets, within the limits of a particular E_T and η_d bin, in an event which passes the less restrictive trigger A.
- The L1 and L2 information stored in the trigger A subsample is used to reconstruct the trigger B decision. Each jet of every event is tested. If one or both of the two leading jets satisfy the trigger A requirement, the two jets are accumulated in the corresponding $N(\Delta E_T, \Delta\eta_d, B)$ bin.
- The relative efficiency of trigger B with respect to trigger A is given by:

$$\varepsilon_{trig}^{rel} = \frac{N(\Delta E_T, \Delta\eta_d, B)}{N(\Delta E_T, \Delta\eta_d, A)}$$

The quantity used to correct the jet cross sections is the absolute event trigger efficiency. For example, the efficiency of the trigger–filter JET_4_MED–JET_MAX is calculated as:

$$\varepsilon^{abs}_{jet\,max} = \varepsilon^{rel}_{jet\,max} \times \varepsilon^{rel}_{jet\,high} \times \varepsilon^{rel}_{jet\,medium} \times \varepsilon^{rel}_{jet\,low} \times \varepsilon^{rel}_{jet\,min}$$

The efficiency of the least restrictive trigger, JET_MIN, cannot be obtained in the same way. Instead, the jet trigger efficiency is determined which is an underestimate of the event trigger efficiency. The procedure for JET_MIN is the following:

- The first two leading jets of every event passing JET_LOW and JET_MEDIUM are excluded to reduce the trigger bias in the sample. In other words, they are more likely to have fired the triggers. The rest of the jets which satisfy JET_LOW, JET_MEDIUM and the standard cuts are considered an unbiased sample suitable to be used in the JET_MIN trigger efficiency calculation.

- Each jet of this unbiased sample is tested for the L1 and L2 condition. If a jet satisfies the requirement, it is counted as a JET_MIN jet by itself. Thus, the JET_MIN trigger efficiency is:

$$\varepsilon^{abs}_{jet\,min} = \frac{N(\Delta E_T, \Delta\eta_d, jet\,min)}{N(\Delta E_T, \Delta\eta_d, unbiased)} \,.$$

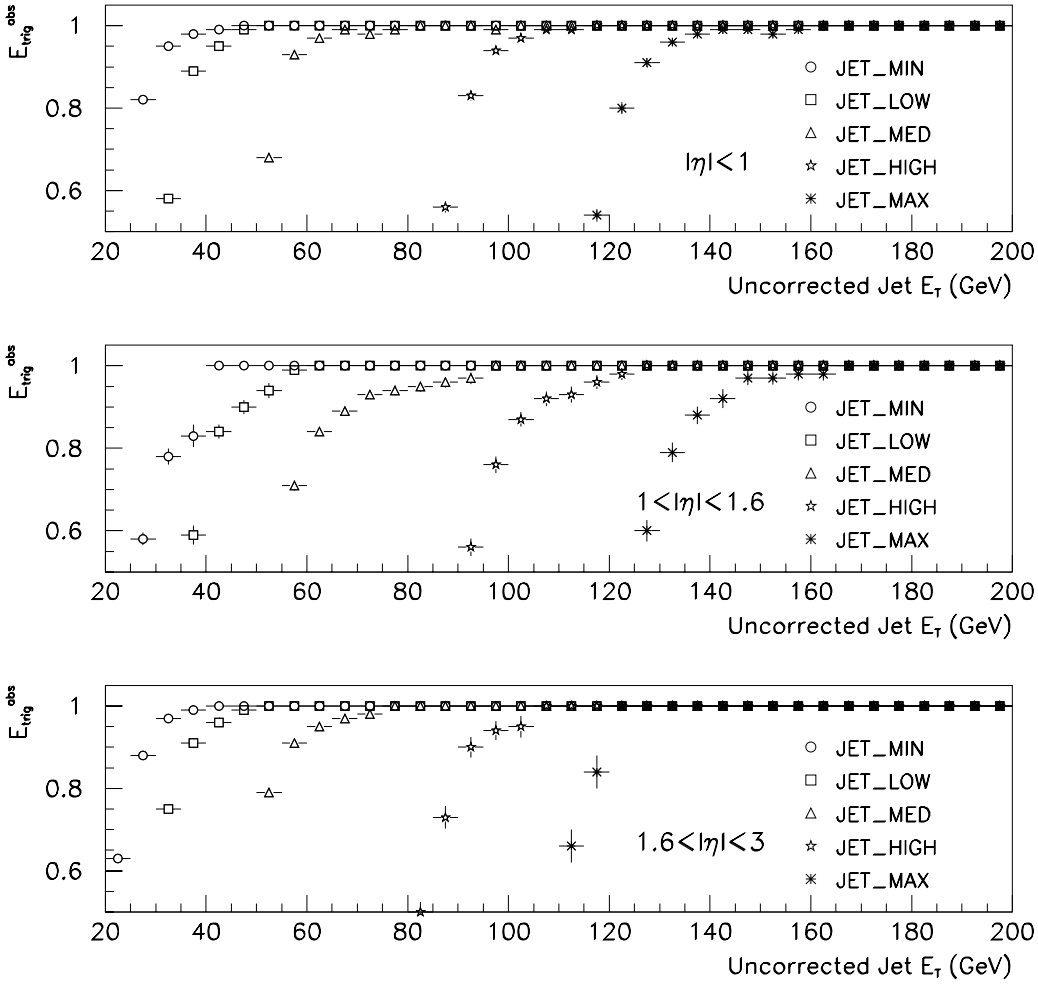

Figure 6.1: Efficiencies of the jet triggers as a function of E_T and η_d for the central, intercryostat and forward regions.

Absolute Trigger Efficiencies

The absolute event efficiencies of the jet triggers for the central, intercryostat and forward regions are plotted as a function of the uncorrected jet E_T in Figure 6.1. Instead of a sharp edge at the E_T trigger threshold, the efficiencies show a slow turn on due to the smearing effects previously mentioned. As a function of η_d, the curves are flat except around $1.2 < \eta_d < 1.4$, where they reach their minimum. The discontinuities observed in some cases are due to low statistics. In other words, the efficiency is artificially set to one when there are no jets in the bin. The general criteria for the inclusive jet cross section measurement is to use the information from the triggers in the E_T , η_d range they are more than 95% efficient. Therefore, the estimated uncertainty on the jet cross sections due to trigger inefficiencies is $\approx 5\%$.

6.2 Cut Efficiencies

The method proposed to calculate the efficiency of the jet cuts is based on the definition of a "true" distribution for each of the variables involved in the cuts[74, 75]. A true distribution includes only good jets and the efficiency of the associated cut is given by the fraction of good jets that remain in the sample once it is applied. In the case of the R_{MTE} cut, the efficiency is given by the fraction of good events surviving the cut.

Most of the fake jets are localized in a very narrow range outside the good jet domain defined by the cut thresholds. Within this domain, it is possible to remove most of the fake jets and obtain a reasonable approximation to the true distribution. Two methods are used to eliminate the noise and calculate the

efficiencies of the standard cuts. The first approach consists of removing only the noisy $\eta - \varphi$ regions. The second adds the R_{MTE} cut to further clean the sample. In both cases the assumption is that neither of the two methods produce a significant modification in the shape of the true distributions. Once most of the fake jets are eliminated, it is reasonable to assume that there are only real collider jets within the good jet domain defined by the cut thresholds. A realistic function is fit to the data in this range and extrapolated outside the good jet domain in order to estimate the fraction of good jets removed by the cut associated with the that particular distribution. The systematic error on the cut efficiencies is mostly due to contamination of the so called true distribution and the choice of the function to parametrize the data points. Thus the difference in the efficiencies obtained from the two alternative methods to clean the sample provides an estimate of the systematic uncertainty. Since there is little trigger bias associated with the calculation of the cut efficiencies[75], the sample used for this study includes all jets regardless of which trigger fires the event. In this way, the higher statistics improve the fit and the accuracy of the final results.

EMF Cut Efficiency

The EMF cut efficiency as a function of the jet E_T is calculated for the CT, IC and FW η_d regions. The method is described in the graphs shown in Figure 6.2. The plots on the top are examples of EMF distributions in the CT region for jets with $E_T \in [50, 100]$ and $E_T \in [100, 150]$. The ten noisy regions are removed to obtain the dashed line histograms and the R_{MTE} cut is added to obtain the solid histograms. The range EMF$\in [0.2, 0.85]$ is considered a part of the true distribution and two gaussian functions are fit to its rising and falling edges.

These curves are extrapolated to EMF= 0.05 and EMF= 0.91 respectively and matched to straight lines that intersect the abscissa at EMF= 0 and EMF= 0.99. The linear extrapolation reflects the fact that the EMF distribution is defined in a finite domain. The limits of the true EMF distribution outside the range $[0.2, 0.85]$ are defined by the gaussian and linear extrapolations.

The EMF cut efficiency for a jet with the average E_T and η_d of a particular bin is calculated as:

$$\varepsilon_{EMF} = \frac{n}{N},$$

where N is the number of jets encompassed by the true distribution and n is the subsample that survives the associated cut. The statistical error dominates at high E_T and is given by:

$$\Delta\varepsilon_{EMF} = \sqrt{\frac{\varepsilon_{EMF}(1-\varepsilon_{EMF})}{N}}.$$

The two methods used to clean the sample provide an estimate of the systematic uncertainty which is added in quadrature to the statistical error. The EMF cut efficiencies as a function of the jet E_T are shown in Table 6.1. The EMF is the most efficient of the standard cuts. However, the efficiency decreases slowly with E_T as the EMF distribution shifts towards lower values.

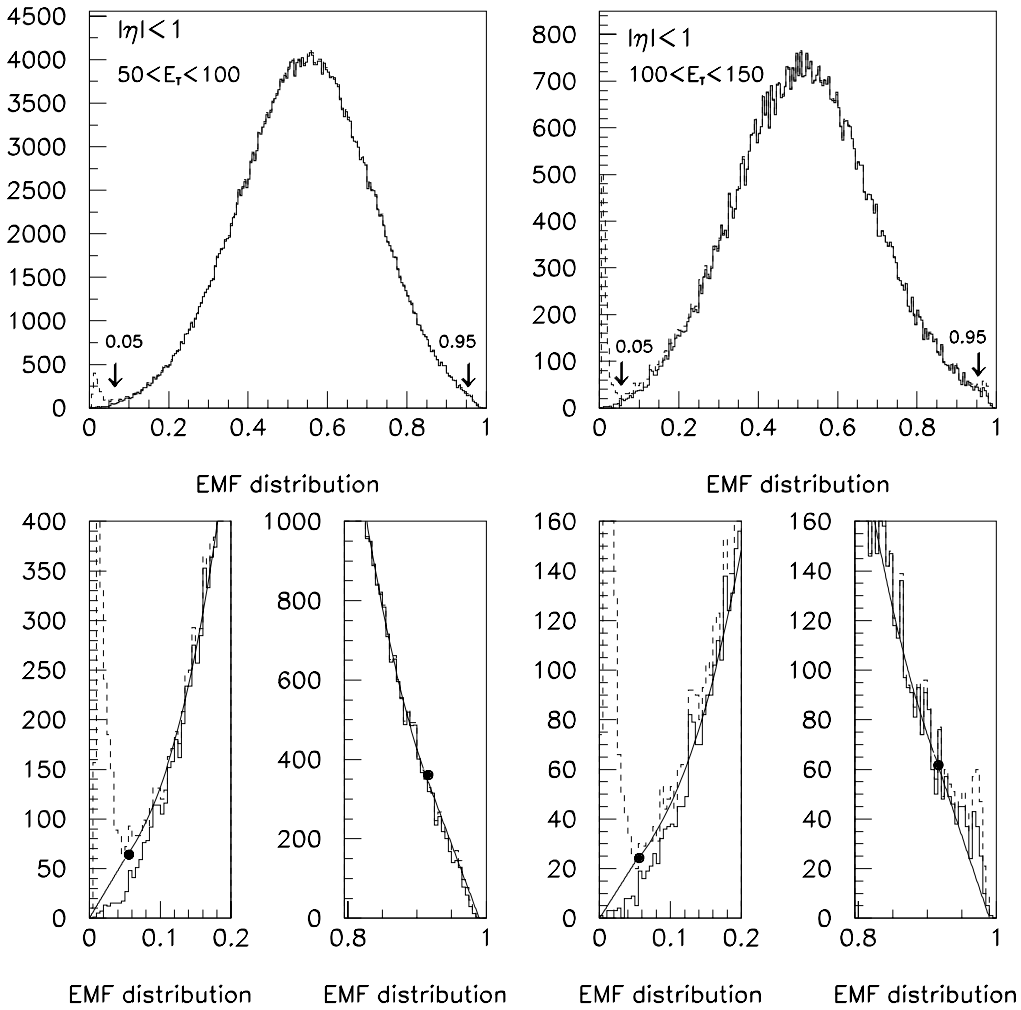

Figure 6.2: Illustration of the method used to calculate the EMF cut efficiency. The histograms in dashed line correspond to a sample deprived from the noisy regions. The R_{MTE} cut is added to obtain the distributions in solid line. The arrows point to the cut thresholds and the dots in the bottom plots indicate the limit between the gaussian fit and the linear parametrization.

HCF Cut Efficiency

The ε_{HCF} calculated here is not the efficiency of the HCF cut but its efficiency after the EMF cut is applied. This improves the accuracy of the method, simplifies the calculation of the cut efficiencies, and its use in physics analyses. The method described for the EMF cut is also used to obtain ε_{HCF}. In this case, a quadratic function is fit to the data in the range HCF$\in [0.1, 0.5]$ and extrapolated until it intersects the abscissa (see Figure 6.3). The HCF cut is the least efficient of the standard cuts. It is quite inefficient at low E_T's but improves at high energies. The results are shown in Table 6.2.

CHF Cut Efficiency

The efficiency of the CHF cut, ε_{CHF}, is calculated after the EMF and HCF cuts are applied. An approximation to the CHF true distribution consists of removing all the jets with $\varphi \in [1.5, 2.2]$, defined as the main ring region. This approach may be complemented with the R_{MTE} cut. The efficiency is the ratio between the number of jets in the true distribution with CHF< 0.4 and the total number of jets in the whole true sample. The results are listed in Table 6.3.

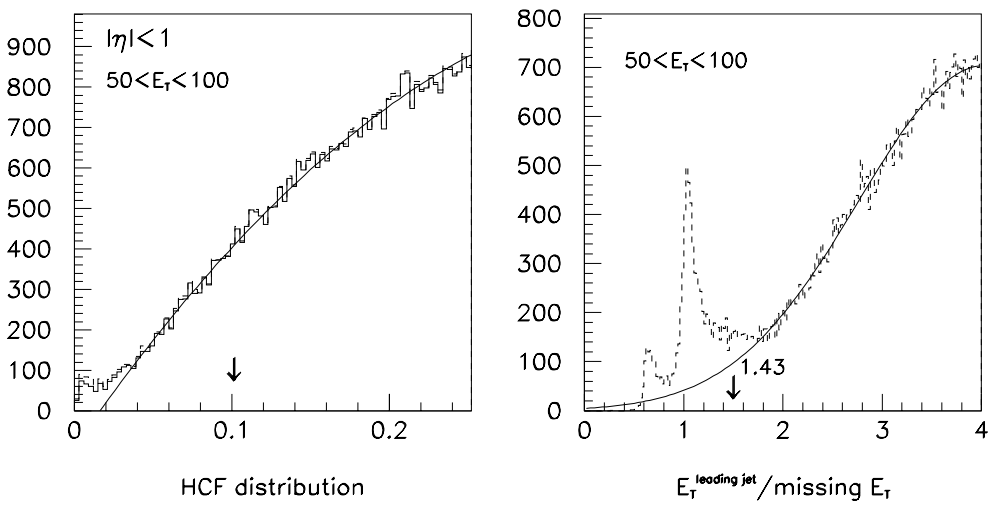

Figure 6.3: Illustration of the method used to calculate the HCF and R_{MTE} cut efficiencies. The histograms in dashed line correspond to a sample deprived from the noisy regions. The R_{MTE} cut is added to obtain the HCF distribution in solid line. A quadratic function is selected to fit the true HCF distribution and a gaussian is chosen in the case of the $1/R_{MTE}$ distribution.

$\not\!\!E_T$ Cut Efficiency

The $\not\!\!E_T$ cut is applied in an event by event basis. That means the whole event is removed if it does not satisfy the R_{MTE} condition. The events with at least one jet in the noisy regions are removed from the sample and the efficiencies are calculated from the $1/R_{MTE}$ distributions. This time, a gaussian function is fit to the data in the range $1/R_{MTE} \in [2, 4]$ and extrapolated to lower $1/R_{MTE}$ values (see Figure 6.3). The R_{MTE} efficiency is obtained with the same procedure used for the standard cuts. The systematic uncertainty is estimated using the fact that it is very unlikely that a good jet event satisfies $1/R_{MTE} < 1$. The efficiencies for this cut are listed in Table 6.4.

Combined Cut Efficiencies

The global efficiency for the standard cuts is obtained as:

$$\varepsilon_{STD} = \varepsilon_{EMF} \times \varepsilon_{HCF} \times \varepsilon_{CHF} \,,$$

where ε_{EMF}, ε_{HCF} and ε_{CHF} are defined as before. This relation does not depend on the order the cuts are applied and is valid even if the three cuts are correlated. The R_{MTE} cut is based on the E_T balance of the event. Hence, it is reasonable to assume that the standard cuts and the R_{MTE} cut are uncorrelated. Then, the total cut efficiency is given by:

$$\varepsilon_{TOT} = \varepsilon_{STD} \times \varepsilon_{MTE}$$

Every jet entry in the inclusive jet cross section measurement is weighted by the total cut efficiency. The error in the cross section due to the jet quality cuts is less than 2%, once the correction is applied. These numbers do not include

the remaining contamination. The total efficiencies of the jet cuts are listed in Table 6.5 and plotted as a function of E_T in Figure 6.4.

Table 6.1: Standard cuts efficiencies as a function of jet E_T for the CT region ($0 < |\eta_d| < 1$). The bins at high E_T were manipulated to study statistical fluctuations.

E_T (GeV)	ε_{EMF}^{CT}	ε_{HCF}^{CT}	ε_{CHF}^{CT}
$8-15$	100.00 ± 0.10	96.62 ± 0.20	99.66 ± 0.10
$15-25$	100.00 ± 0.10	97.32 ± 0.20	99.80 ± 0.10
$25-40$	99.96 ± 0.10	97.69 ± 0.20	99.75 ± 0.10
$40-60$	99.91 ± 0.10	97.91 ± 0.20	99.70 ± 0.10
$60-80$	99.83 ± 0.10	97.75 ± 0.20	99.61 ± 0.10
$80-100$	99.67 ± 0.10	97.62 ± 0.21	99.60 ± 0.10
$100-130$	99.61 ± 0.10	97.25 ± 0.22	99.45 ± 0.11
$130-160$	99.55 ± 0.12	96.99 ± 0.28	99.43 ± 0.13
$160-175$	99.51 ± 0.18	97.53 ± 0.60	98.88 ± 0.34
$175-200$	99.22 ± 0.25	97.51 ± 0.67	99.33 ± 0.35
$200-220$	99.0 ± 0.4	97.79 ± 0.64	99.33 ± 0.39
$220-228$	98.4 ± 1.1	97.1 ± 1.8	100 ± 1
$228-241$	99.1 ± 0.9	97.9 ± 1.7	100 ± 1
$241-260$	99.0 ± 1.0	97.7 ± 1.8	100 ± 1
$260-450$	98.9 ± 1.1	100 ± 1	100 ± 1

Table 6.2: Standard cuts efficiencies as a function of the jet E_T for the IC region ($1 < |\eta_d| < 1.6$). The bins at high E_T were manipulated to study statistical fluctuations.

E_T (GeV)	ε_{EMF}^{IC}	ε_{HCF}^{IC}	ε_{CHF}^{IC}
$8-15$	100.00 ± 0.01	93.28 ± 0.20	99.65 ± 0.05
$15-25$	99.99 ± 0.10	95.99 ± 0.20	99.64 ± 0.05
$25-40$	99.95 ± 0.10	97.36 ± 0.20	99.50 ± 0.054
$40-60$	99.94 ± 0.10	97.57 ± 0.20	99.33 ± 0.054
$60-80$	99.92 ± 0.10	97.43 ± 0.21	99.16 ± 0.06
$80-100$	99.91 ± 0.10	97.19 ± 0.22	98.91 ± 0.08
$100-130$	99.94 ± 0.10	96.54 ± 0.22	98.45 ± 0.10
$130-160$	99.93 ± 0.10	95.80 ± 0.30	98.51 ± 0.18
$160-174$	99.90 ± 0.13	95.3 ± 1.2	97.73 ± 0.50
$174-200$	99.86 ± 0.17	94.7 ± 1.3	97.11 ± 0.70
$200-220$	99.65 ± 0.36	94.8 ± 1.7	98.95 ± 0.70
$220-228$	98.4 ± 1.5	93.0 ± 4.3	97.6 ± 2.4
$228-241$	100 ± 1	94.0 ± 3.4	97.3 ± 2.5
$241-260$	100 ± 1	87 ± 6	96.4 ± 2.4
$260-450$	100 ± 1	80 ± 6	91.3 ± 5.8

Table 6.3: Standard cuts percent efficiencies as a function of the jet E_T for the FW region ($1.6 < |\eta_d| < 3$). The bins at high E_T were manipulated to study statistical fluctuations.

E_T (GeV)	ε_{EMF}^{FW}	ε_{HCF}^{FW}	ε_{CHF}^{FW}
$8-11$	99.71 ± 0.10	97.60 ± 0.10	99.82 ± 0.10
$11-25$	99.63 ± 0.10	98.03 ± 0.10	99.86 ± 0.10
$25-40$	99.38 ± 0.12	98.24 ± 0.10	99.85 ± 0.10
$40-60$	99.35 ± 0.10	98.36 ± 0.10	99.84 ± 0.10
$60-80$	99.37 ± 0.10	98.29 ± 0.11	99.80 ± 0.10
$80-100$	99.24 ± 0.10	97.22 ± 0.14	99.43 ± 0.12
$100-110$	99.05 ± 0.17	96.69 ± 1.1	99.06 ± 0.21
$110-130$	98.84 ± 0.22	95.42 ± 1.1	98.35 ± 0.29
$130-140$	98.85 ± 0.57	93.75 ± 1.7	98.40 ± 0.70
$140-160$	98.54 ± 0.70	96.96 ± 1.1	97.5 ± 1.1

Table 6.4: R_{MTE} cut efficiencies as a function of the leading jet E_T.

$E_T^{leading\,jet}$ (GeV)	ε_R
$25-40$	99.28 ± 0.10
$40-60$	99.60 ± 0.10
$60-80$	99.65 ± 0.10
$80-100$	99.78 ± 0.10
$100-130$	99.72 ± 0.10
$130-160$	99.59 ± 0.10
$160-450$	99.42 ± 0.10

Table 6.5: combined efficiencies of the standard jet cuts, as a function of jet E_T for the three detector regions.

E_T (GeV)	ε_{STD}^{CT}	ε_{STD}^{IC}	E_T (GeV)	ε_{STD}^{FW}
$8-11$	95.96 ± 0.29	92.19 ± 0.28	$8-11$	95.95 ± 0.15
$11-25$	96.69 ± 0.29	95.30 ± 0.29	$11-25$	96.50 ± 0.15
$25-40$	96.78 ± 0.29	96.20 ± 0.29	$25-40$	96.37 ± 0.15
$40-60$	97.01 ± 0.29	96.30 ± 0.29	$40-60$	96.78 ± 0.15
$60-80$	96.86 ± 0.3	96.20 ± 0.30	$60-80$	96.67 ± 0.17
$80-100$	96.67 ± 0.3	95.62 ± 0.31	$80-100$	95.53 ± 0.27
$100-130$	96.26 ± 0.31	95.35 ± 0.32	$100-107$	95.28 ± 0.51
$130-160$	95.87 ± 0.36	93.61 ± 0.44	$107-130$	93.00 ± 0.61
$160-174$	95.89 ± 0.62	91.13 ± 0.50	$130-140$	93.9 ± 1.4
$174-205$	95.65 ± 0.65	92.5 ± 1.3	$140-160$	94.5 ± 1.9
$205-225$	93.1 ± 1.8	91.8 ± 2.3		
$225-241$	96.9 ± 1.8			
$241-450$	95.6 ± 1.7			

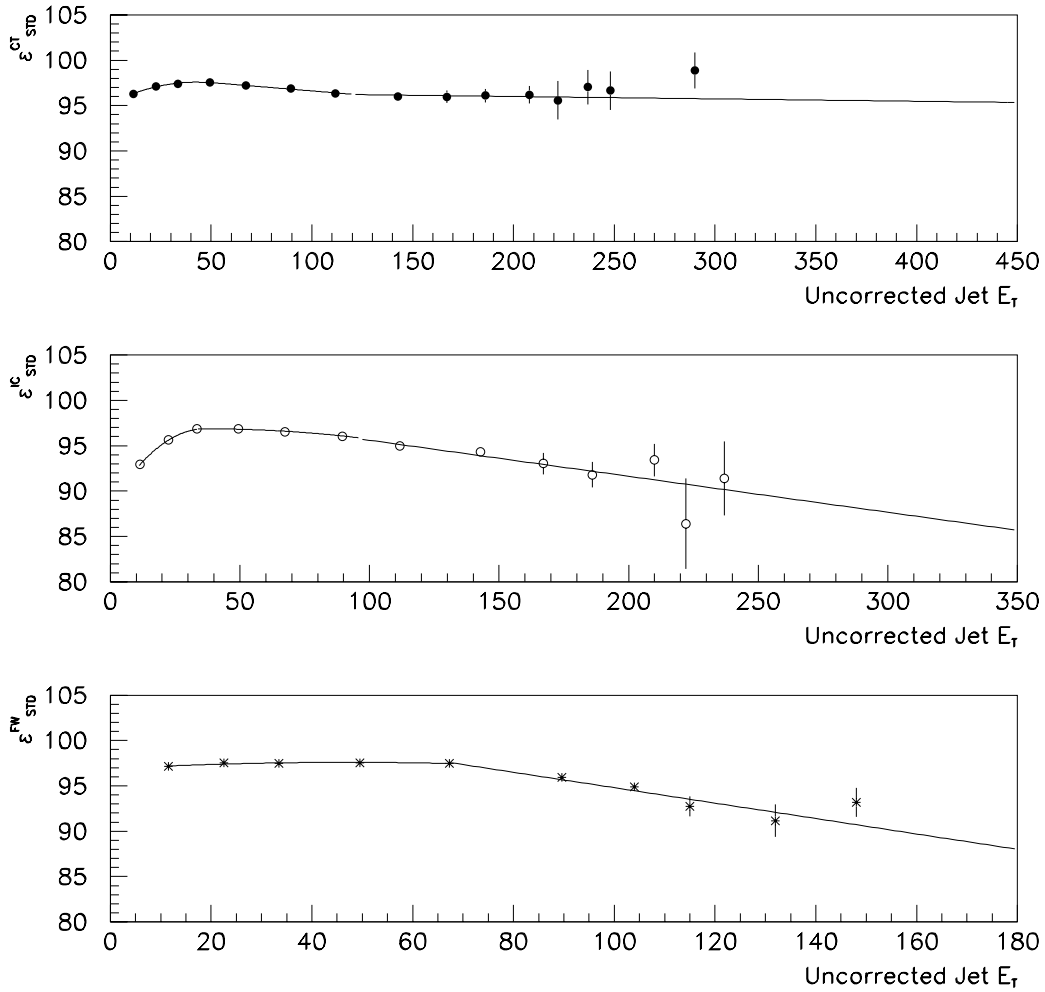

Figure 6.4: Combined Efficiencies of the standard jet cuts, ε_{STD} as a function of jet E_T for the three detector regions. CT: $0 < |\eta_d| < 1$, IC: $1 < |\eta_d| < 1.6$ and FW: $1.6 < |\eta_d| < 3$.

6.3 Jet Energy Corrections

The reconstructed jet energy and E_T are different from those associated with the parent parton jet, which is the object of the inclusive jet cross section measurement. The energy scale is the factor that scales the reconstructed jet energy to the energy of the parent parton jet. DØRECO uses the energy response to single pions and electrons from the test beam. However, the reconstruction program does not return the correct parton jet energy for the reasons enumerated below:

- **Non–linearities** in the calorimeter energy response to low E_T particles ($\leq$ 10 GeV). A particle jet is composed of numerous particles carrying different amounts of energy. Even very energetic jets have a large fraction of their total energy distributed among a large number of low energy particles.

- **Energy losses** in non–instrumented regions like the central detectors, the cryostat walls or calorimeter cracks.

- **Reconstruction effects** related to the fixed cone algorithm. A fraction of the jet energy is leaked outside the cone by showers of particles produced inside the calorimeter.

- **Uranium Noise and underlying event contamination** captured within the cone limits and included in the energy determination.

The original parton jet energy also gets smeared due to resolution effects. Therefore, the jet energy resolution must be determined to remove this effect from the jet E_T spectrum.

6.3.1 Energy Scale

The jet energy scale correction is obtained in several steps [51, 76]. It is a complicated function of the reconstructed jet energy, E_T , η_d, EMF, and the algorithm cone size. The $5-7\%$ error band in the jet scale, propagates to a $20-50\%$ error in the inclusive jet cross section which makes it the largest contribution to the total systematic uncertainty. The dependence of the energy scale on different variables such us the EMF, η_d and E_T is illustrated in Figures 6.5– 6.6.

Electromagnetic Scale

The electromagnetic scale is corrected by +1.2% in the forward calorimeters and 7.2% in the central calorimeters. These numbers make the DØ sample of $Z \to e^+e^-$ decays to produce a mass peak at the value measured by the LEP experiments.

Jet Scale as a Function of EMF

The EMF dependence of the jet energy response is obtained from a dijet event sample. The quantity R_{EMF} is defined as:

$$R_{EMF}(EMF_2) = \frac{E_{T_2}}{E_{T_1}},$$

where E_{T_1} is the transverse energy of the "trigger" jet and E_{T_2} that of the "probe" jet. A "trigger" jet is defined as a jet that satisfies by itself the trigger requirements. The "probe" jet is used to examine the EMF dependence. The average R_{EMF} is determined for each EMF bin of the probe jet. Therefore, R_{EMF} is regarded as the energy response for a jet with a particular EMF with respect to a jet of the same E_T and average EMF.

Jet Scale in the Central Calorimeters

The jet energy scale in the central calorimeters is obtained using the Missing E_T Projection Fraction method initially developed at CDF and modified at DØ [77, 78]. The technique requires real collider events containing one photon and one or two jets. The events must satisfy the cut $\not{E}_T < E_{T_\gamma}$ and the jets have to pass the standard cuts. In addition, the jet $|\eta_d|$ must be less that 0.7 to avoid jets for which a significant amount of energy is deposited outside the CC. The photon is defined as an electromagnetic cluster (EMF>0.9) with a pseudo–rapidity less than 0.9 and isolated from other energy clusters. The missing E_T projection fraction (MPF) is defined as:

$$MPF = -\frac{\hat{n}_\gamma \cdot \vec{\not{E}_T}}{E_{T_\gamma}} ,$$

where $\hat{n}_\gamma$ is the unit vector in the direction of the photon, $\vec{\not{E}_T}$ is the missing transverse energy vector and E_T^γ is the corrected transverse energy of the photon. The MPF is measured as a function of $E_J = E_{T_\gamma} cosh\, \eta_J$, which is a good estimate of the true jet energy in the case of a one photon plus one jet final state. If the events are binned in terms of $E_J = E_{T_\gamma} cosh\, \eta_J$, it is possible to plot this quantity as a function of the average reconstructed jet energy E_J^{reco}. A linear parametrization like $F(E_J^{reco}) = E_{T_\gamma} cosh\, \eta_J$ establishes a link between E_J^{reco} and the correction corresponding to $MPF(E_J)$.

In summary, the way to use the MPF to correct the jet energy is the following:

- The linear parametrization $F(E_J^{reco})$ is used to associate E_J^{reco} with the energy E_J of a jet in a leading order one photon plus one jet process.

- Since $MPF \equiv MPF(E_J)$ was measured as a function of E_J, it can also be

written as a function of E_J^{reco}.Then, the jet energy response in the central calorimeters is given by:

$$R_J = 1 - MPF\left(F(E_J^{reco})\right).$$

Both the jet energy and E_T are corrected with the same scale factor R_J.

Jet Scale as a Function of η_d

A sample of two–jet events is used to project the energy calibration to the forward regions. Initially, both the trigger jet and the probe jet are required to be central ($|\eta_d| < 0.7$). The ratio between the probe jet E_T and the trigger jets E_T is measured in that region. Under the assumption that this ratio is a constant function of the probe jet η, the calibration is extended to the forward regions allowing probe jets of all η's in the sample. If E_{T_2} is the transverse energy of the probe jet and E_{T_1} that of the trigger jet, the corrected E_{T_2} for the probe jet is obtained from the ratio:

$$R_\eta(\eta_2) = \frac{E_{T_2}}{E_{T_1}}$$

by requiring R_η to be equal to the ratio associated with a central trigger jet of the same E_{T_1} and a central probe jet. This part of the calibration accounts for the jet energy leaked outside the cone by the fragments of the parent parton jet, which becomes a large effect at high η's.

Underlying Event and Uranium Noise Subtraction

The underlying event is responsible for a small amount of spurious energy deposited in the calorimeters. Using a minimum bias sample, the energy density associated with the average underlying event is measured as a function of η. The

energy density increases with η, but the corresponding E_T density is approximately flat as function of pseudo–rapidity. Another source of spurious energy is due to uranium decay. A non–zero suppressed sample is used to determine the energy density associated with uranium noise contamination, which is flat as a function of η_d. Hence the E_T density vanishes at very high η_d's. The E_T density contributed by both the underlying event and the uranium noise is expressed in GeV per unit area in $\eta - \varphi$ space and goes from 1.8 through 1.2 as a function of E_T . Therefore, the energy scale determination is completed with the subtraction of $1.8 - 3$ GeV from the jet transverse energy in the case of the 0.7 fixed cone algorithm. This is a big correction for low E_T jets.

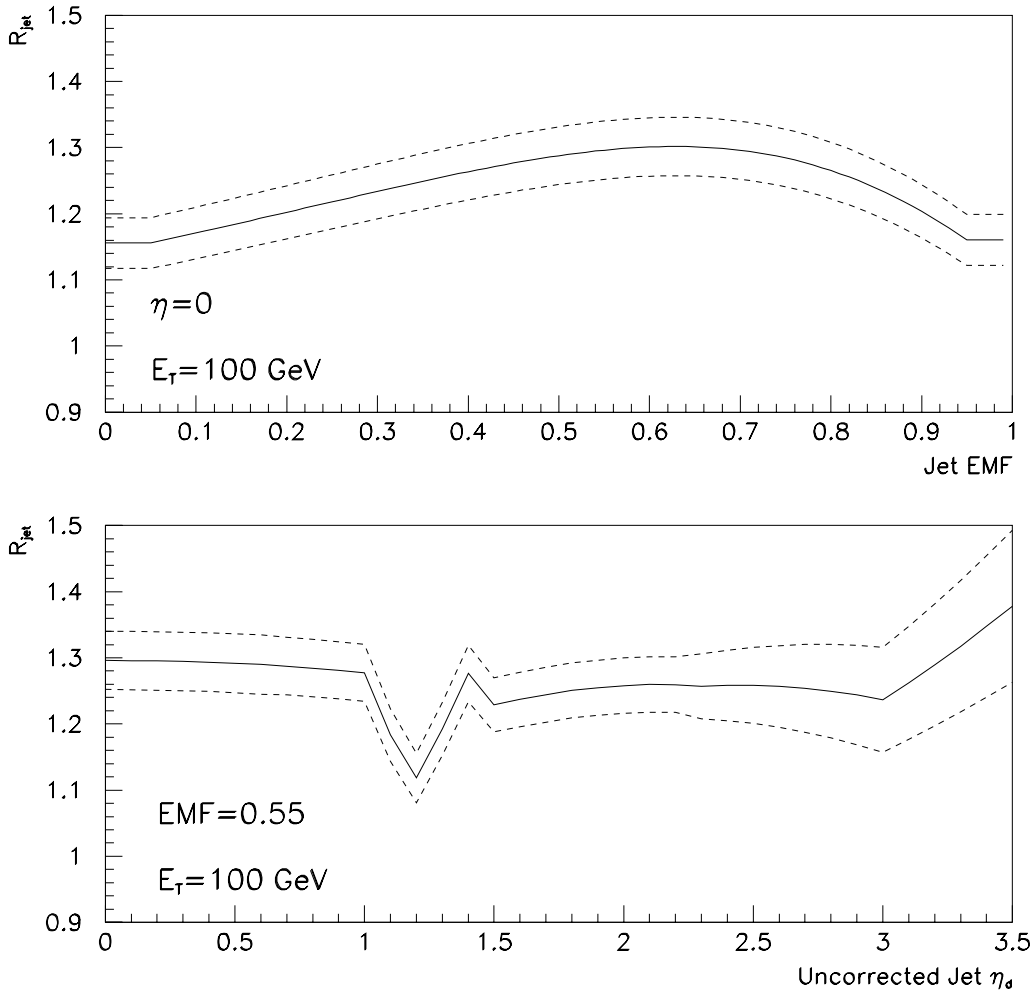

Figure 6.5: Dependence of the energy scale on the jet electromagnetic fraction (EMF) and η_d. The response is better for jets with high and low EMF and gets worse in the forward η_d region due to out of cone effects. The band within dashed lines represents the energy scale uncertainty.

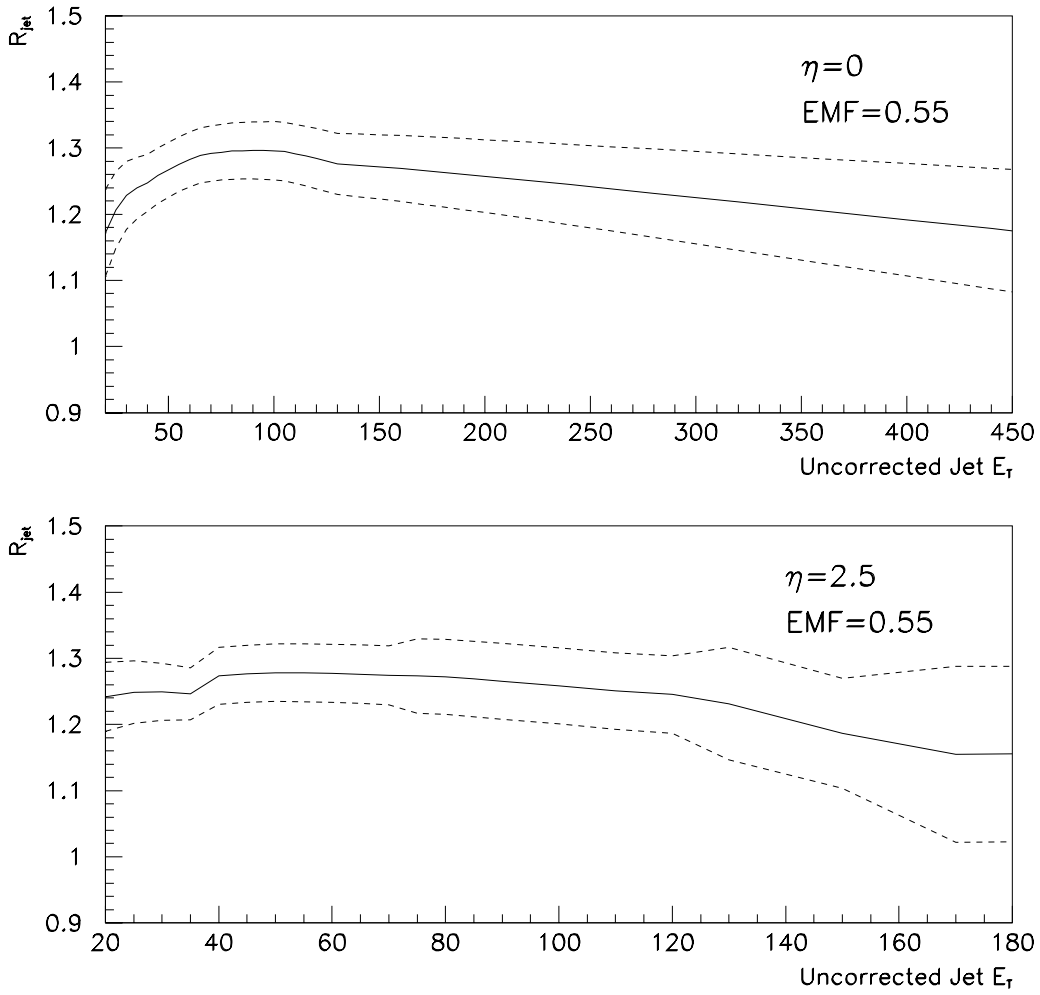

Figure 6.6: Energy Scale correction factor as a function of E_T for jets with $\eta_d = 0$ and $\eta_d = 2.5$. The band within dashed lines represents the energy scale uncertainty.

6.3.2 Energy Resolution

Since the inclusive jet cross section is measured as a function of the jet E_T for different η bins, it is necessary to determine the jet E_T resolution as a function of its transverse energy and pseudo–rapidity. The method introduced in reference[53] is used on a sample of collider dijet events to obtain the jet E_T resolution.

Definitions and Method

The determination of the jet E_T resolution is based on energy conservation in the transverse plane. Therefore, the events must be selected and handled very carefully to minimize the effect of additional low E_T jets and contamination. Although the resolution is a function of the jet position within the calorimeters, the jet E_T resolution is measured here in different physics η bins since it will be used to unsmear jet E_T distributions which are binned in terms of the jet physics η. In any case, the resolutions presented in this section agree within statistical errors with the resolutions calculated in terms of η_d. The following cuts are applied to the dijet sample:

- The z–coordinate of the interaction vertex must be within 100 cm of the center of the detector.
- The two leading jets must have $E_T > 15$ GeV and be back to back in φ within 25°. If there are other jets in the event, they must have $E_T < 10$ GeV.
- All the jets in the event must satisfy the jet quality cuts.

In addition, the jet pseudo–rapidity is corrected for the reconstruction bias, mentioned in chapter 4, and the two leading jets are required to be in the same η

region so that their resolutions are approximately the same.

For low E_T jets, the resolution is also obtained from a $\gamma - jets$ sample[80]. One photon and one or two jets are allowed in the sample. The photon pseudo–rapidity is constrained to $\eta < 0.7$. The γ is required a transverse energy greater than 15 GeV and the leading jet $E_T > 10$ GeV. They also have to be back to back in φ within 15°. The other jets must have $E_T < 10$ GeV. The photon and the jet E_T 's are corrected and the photon spectrum is binned in terms of E_T . The resolution is the width of the jet E_T distribution associated with each photon bin. This method provides a measurement of the jet E_T resolution which is independent of the jet energy scale. On the other hand, the approach considers the γ resolution negligible with respect to the jet resolution. This is not a good assumption for high E_T jets in the forward region since the photons are constrained to the central calorimeter. Hence, the photon data is only used to obtain low E_T measurements of the fractional jet E_T resolution.

The jet balance method is based on the asymmetry variable A which is defined as:

$$A = \frac{E_{T_1} - E_{T_2}}{E_{T_1} + E_{T_2}} ,$$

where E_{T_1} and E_{T_2} are the transverse energies of the two leading jets. The variance of the asymmetry distribution can be written as:

$$\sigma_A^2 = \left| \frac{\partial A}{\partial E_{T_1}} \right|^2 \sigma_{E_{T_1}}^2 + \left| \frac{\partial A}{\partial E_{T_2}} \right|^2 \sigma_{E_{T_2}}^2 .$$

Assuming $E_T \equiv E_{T_1} = E_{T_2}$ and $\sigma_{E_T} \equiv \sigma_{E_{T_1}} = \sigma_{E_{T_2}}$, the fractional transverse energy resolution can be expressed as a function of σ_A in the following way:

$$\left(\frac{\sigma_{E_T}}{E_T} \right) = \sqrt{2} \sigma_A .$$

Results

Figure 6.7 shows the fractional transverse energy resolution as a function of the scale corrected jet energy, which is calculated for each dijet event as the average energy of the two leading jets. The data points for three detector regions bins can be parametrized with a form:

$$\left(\frac{\sigma_{E_T}}{E_T}\right)^2 = \frac{N^2}{E^2} + \frac{S^2}{E} + C^2$$

The different sets of parameters corresponding to each detector region are displayed in Table 6.6.

Table 6.6: Parametrization of the fractional transverse energy resolution as a function of the scale corrected jet energy.

η	N (GeV^2)	S (GeV)	C
$0 - 0.8$	4.92 ± 0.18	0.95 ± 0.01	0.
$0.8 - 1.5$	4.24 ± 2.30	1.51 ± 0.12	0.058 ± 0.01
$1.5 - 3$	0.	2.23 ± 0.03	0.

The E_T resolution in the intercryostat region is much worse than in the central calorimeters as a consequence of the cracks and the existence of large quantities of uninstrumented material. The resolution in the forward region is worse than in the central calorimeters and the intercryostat region due to out of cone and η resolution effects. In fact, the position resolution on the jet E_T measurement is folded into the curves shown in Figure 6.7. The effect of the η resolution on the η spectrum will be discussed in the next sections.

The same functional form is used to parametrize the fractional E_T resolution as a function of the scale corrected jet E_T for five different η regions. These are the curves needed to unsmear the jet cross sections. Figures 6.8 and 6.9 show how

the resolutions in the forward regions fall below those in the central regions when they are plotted as a function of the jet E_T . Table 6.7 contains the values of the parameters.

Table 6.7: Parametrization of the fractional transverse energy resolution as a function of the scale corrected jet E_T . It includes low E_T $\gamma - jet$ data points.

η	N (GeV^2)	S (GeV)	C
$0 - 0.5$	5.99 ± 0.18	0.80 ± 0.03	0.
$0.5 - 1$	5.15 ± 0.25	0.96 ± 0.03	0.
$1 - 1.5$	0.0011 ± 0.0001	1.29 ± 0.03	0.053 ± 0.010
$1.5 - 2$	6.80 ± 0.32	0.53 ± 0.08	0.
$2 - 3$	6.16 ± 0.37	0.62 ± 0.10	0.

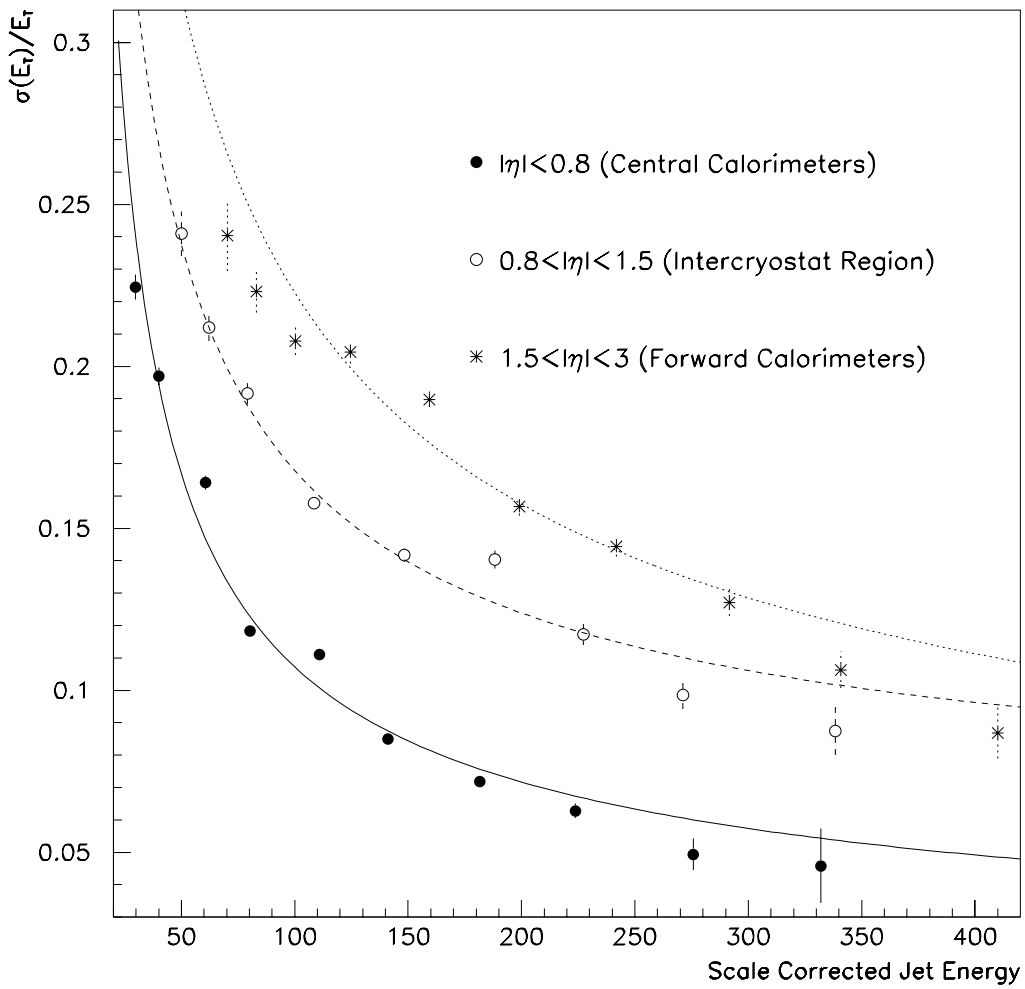

Figure 6.7: Parametrization of the fractional transverse energy resolution as a function of the scale corrected jet energy.

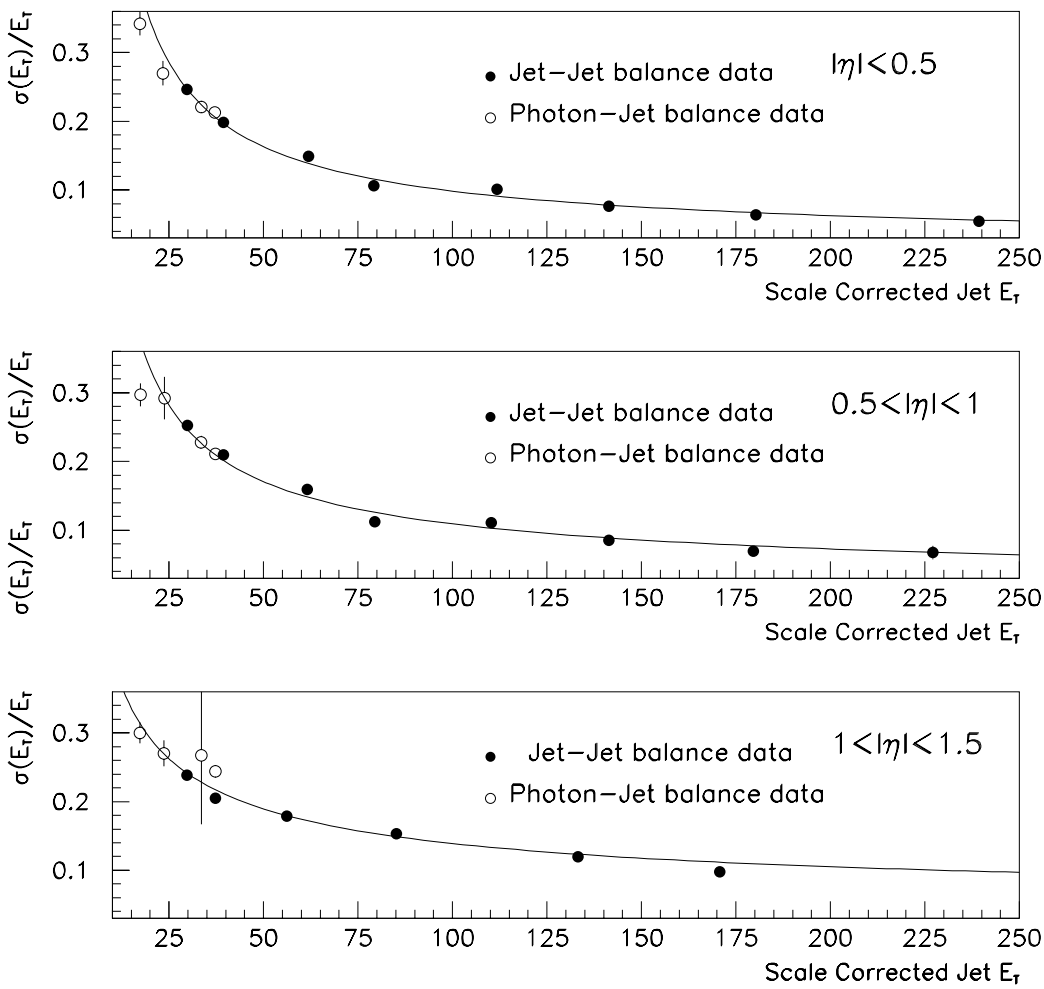

Figure 6.8: Parametrization of the fractional transverse energy resolution in the CT and IC regions as a function of the scale corrected jet E_T . The dark circles are obtained from the $jet - jet$ sample and the open circles are associated with $\gamma - jet$ events. The fit includes both sets of measurements.

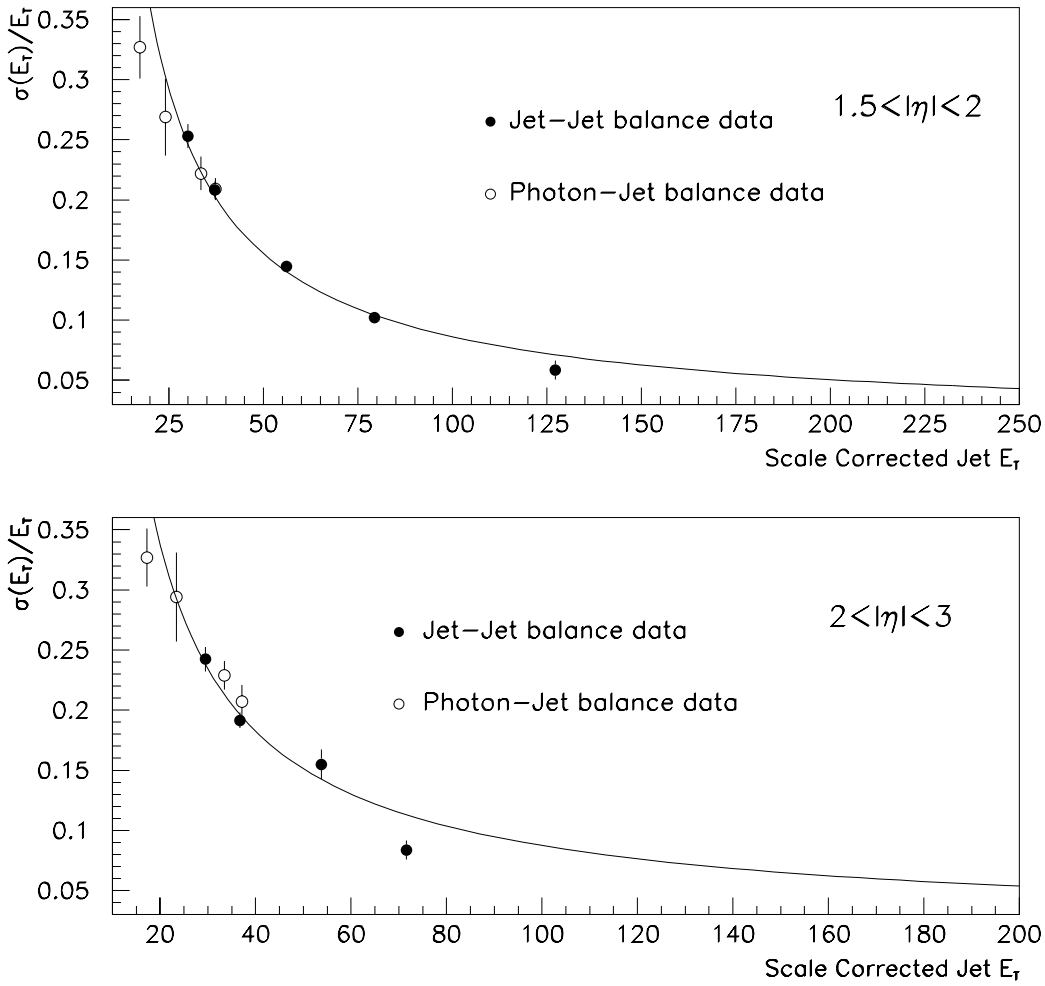

Figure 6.9: Parametrization of the fractional transverse energy resolution in the forward regions as a function of the scale corrected jet E_T . The dark circles are obtained from the $jet-jet$ sample and the open circles are associated with $\gamma-jet$ events. The fit includes both sets of measurements.

6.4 Jet Position Corrections

Several detector and reconstruction effects contribute to the mismeasurement of the jet position, which is given by the azimuthal and polar angles φ and θ. Jets are produced symmetrically around the beam direction making the inclusive jet cross section a constant function of φ. In addition, the DØ calorimeters are uniform in φ, except for the intermodule cracks which produce a negligible effect on the detector acceptance. Therefore, the accurate determination of the azimuthal coordinate is not crucial. On the other hand, the strong dependence of the jet cross sections upon the jet η makes its accurate measurement a critical issue.

6.4.1 Reconstructed η Bias

Description of the Problem

The jet pseudo–rapidity must be related to the parent parton if the experimental measurement is to be compared to theoretical predictions. The η_d dependence of the calorimeter energy response together with algorithm related effects are responsible for a bias of the reconstructed jet η. The η_d of a parton jet assuming perfect position resolution would be:

$$\eta_d^{parton} = \eta_d^{reco} + \rho(E, \eta_d)\,,$$

where η_d^{reco} is the reconstructed jet η_d and $\rho(E, \eta_d)$ is the bias which must be extracted from the reconstructed pseudo–rapidity to obtain η_d^{parton}. Qualitatively, the bias in the range $|\eta_d| \in [1.2, 1.4]$ may be explained as the result of the energy response in the IC region affecting the η determination from the E_z and E of the jet as described in chapter 4. The increase in the bias for $|\eta_d| > 1.8$ is due to out of cone effects which come from the asymmetry of the cone in real space.

Corrected η from a Monte Carlo Simulation

The best way to deal with the η bias is by means of a Monte Carlo simulation. The bias is expected to depend on the jet shape and width which are strongly related to the hadronization model. The HERWIG generator is selected since it provides jets with the most realistic shape[81]. A fixed cone algorithm with the same parameter values specified in chapter 4 is chosen to perform the jet reconstruction both at parton and calorimeter level. Statistically, $< \rho(E, \eta_d) >$ can be obtained as $< \eta_d^{parton} - \eta_d^{reco} >$ where the matching condition described in chapter 4 is used to associate parton jets with reconstructed jets. Figure 6.10 shows the η_d bias as a function of η_d^{reco} for different energy bins. The bias in the negative η_d hemisphere is projected with a negative sign onto the positive hemisphere to improve statistics. A third degree polynomial is fit to the range $|\eta_d| \in [0, 1.8]$ in each of the histograms of Figure 6.10, which correspond to six different energy bins:

$$< \rho(E, \eta_d) >= \alpha + \beta E + \gamma E^2 + \delta E^3$$

A quadratic function is fit in the range $|\eta_d| \in [1.8, 3]$ to complete the parametrization of $< \rho(E, \eta_d) >$:

$$< \rho(E, \eta_d) >= \alpha' + \beta' E + \gamma' E_2$$

The parameters are included in Table 6.8.

The η bias correction is applied to the jet η_d^{reco} in the inclusive jet cross section measurement. To recapitulate, the physics η is translated into η_d, corrected for the bias, and translated back into a corrected physics η.

Table 6.8: Parametrization of the η bias as a function of reconstructed η_d for different energy bins.

Jet Energy (GeV)	α	β	γ	δ
$20-40$	0.0030	-0.021	0.079	-0.036
$40-70$	0.0016	-0.0011	0.043	-0.022
$70-100$	0.00047	-0.0036	0.039	-0.020
$100-200$	0.00047	0.0074	0.0095	-0.0072
$200-300$	-0.00095	0.0068	0.010	-0.0076
$300-500$	-0.00094	0.016	-0.0086	0.00053
Jet Energy (GeV)	α'	β'	γ'	
$20-40$	-0.059	0.044	0	
$40-70$	-0.072	0.047	0	
$70-100$	0.046	-0.077	0.030	
$100-200$	0.0055	-0.026	0.014	
$200-300$	0.012	-0.027	0.012	
$300-500$	0.0059	-0.019	0.0089	

The HERWIG events were generated at $z = 0$. This is not realistic since the z position of the interaction point is not well described by a $\delta(z)$ distribution. The effect of the z–vertex position on the η bias is studied using an ISAJET sample which includes a realistic simulation of the gaussian z–vertex distribution observed in collider data. If the z–vertex distribution is centered at $z = 0$, the bias agrees within statistical errors with the bias observed in a sample constrained to a narrow bin around $z = 0$ [79].

The ISAJET simulation gives twice the η bias observed with the HERWIG simulation. The explanation may be related to the differences in the hadronization models used in the two generators [79]. Although the η bias may be as large as 0.08 for high η's and low energies, it stays below 0.04 in the E_T, η regions of interest. To be consistent with the DØ jet definition and the way the energy scale is determined, the η bias has to be extracted but the jet E_T must not be

recalculated using the corrected η. The reason is that the MPF method does not use the jet position to determine the energy and E_T scale corrections.

The effect of the η bias correction on the inclusive jet cross section depends on the size of the η bins. For 0.5 bins the difference between corrected and uncorrected cross sections varies from a 2% in the region $|\eta| < 0.5$ to a 7% in the in the η bin $2.5 < |\eta| < 3$ [83].

6.4.2 η Resolution

Once the bias is extracted from the η measurement, the quantity $\eta_d^{parton} - \eta_d^{cor}$ should be zero. As a result of the finite calorimeter segmentation, $\eta_d^{parton} - \eta_d^{reco}$ follows a gaussian distribution with a variance $\sigma_\eta(E, \eta_d)$ defined as the jet η resolution. The examples in Figure 6.11 show the change in the width of the $\eta_d^{parton} - \eta_d^{reco}$ distributions once the bias correction is applied. This change may be as large as 20% in the forward region [79]. The quantity $\sigma_\eta(E, \eta_d)$ is obtained from the HERWIG sample and parametrized in six different η_d bins with the form:

$$\sigma_\eta(E, \eta_d) = A + \frac{B}{E} + \frac{C}{E^2} \, .$$

The results are summarized in Table 6.9 and displayed in Figure 6.12.

Once again, the ISAJET simulation returns resolution numbers twice as large as those obtained with HERWIG [79]. Both ISAJET and HERWIG results are in good agreement with those obtained in previous studies [53, 52, 82].

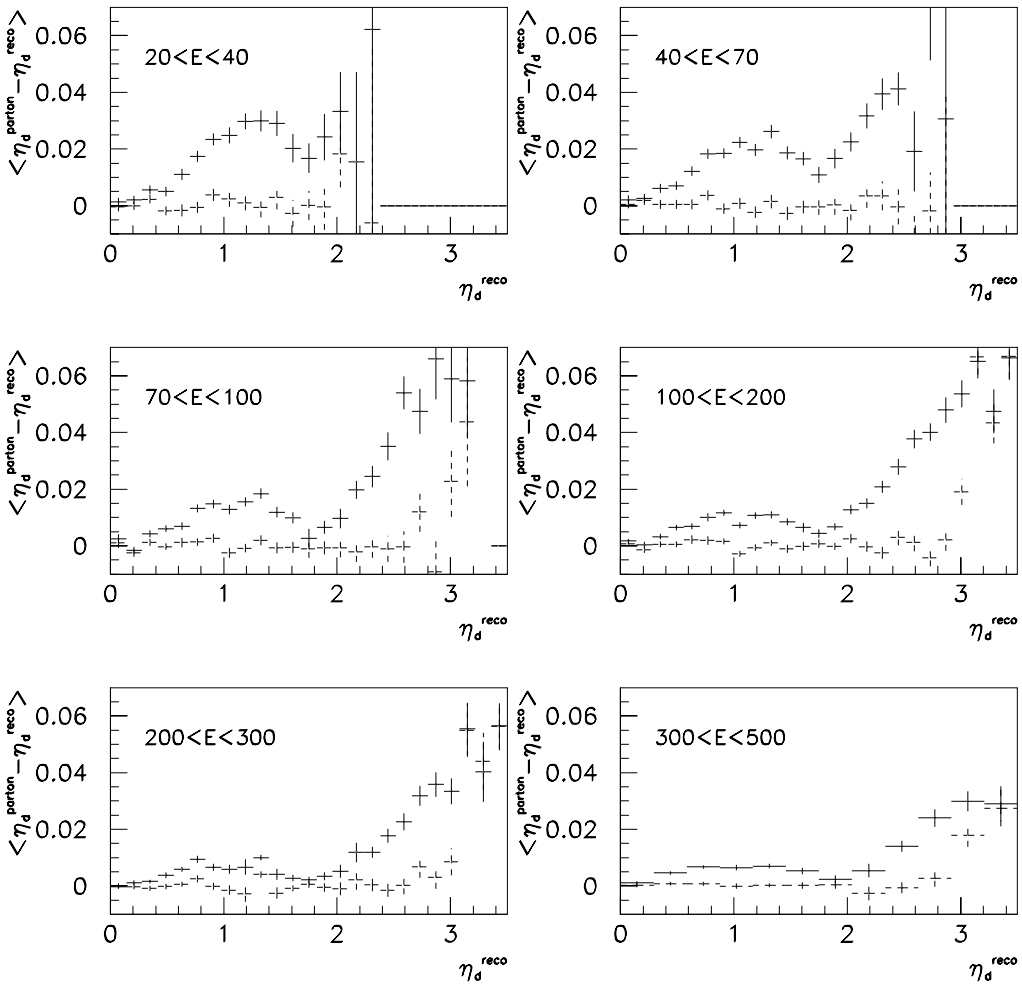

Figure 6.10: HERWIG monte carlo simulation of the η bias as a function of the jet η_d^{reco} and energy (in GeV). $< \rho(E, \eta_d) >$ is plotted in solid line. As a consistency check, $< \eta_d^{parton} - \eta_d^{cor} >$ is plotted in dashed line after the bias correction is applied.

Table 6.9: Parametrization of the jet η resolution as a function of parton jet energy for different η_d bins.

η_d	A	B (GeV)	C (GeV^2)
$0-0.5$	0.0057	0.820	-0.960
$0.5-1$	0.0039	1.19	-3.860
$1-1.5$	0.0052	1.74	-10.98
$1.5-2$	0.0037	2.42	-17.10
$2-2.5$	0.0011	4.00	-100.3
$2.5-3$	0.00081	8.08	-248.0

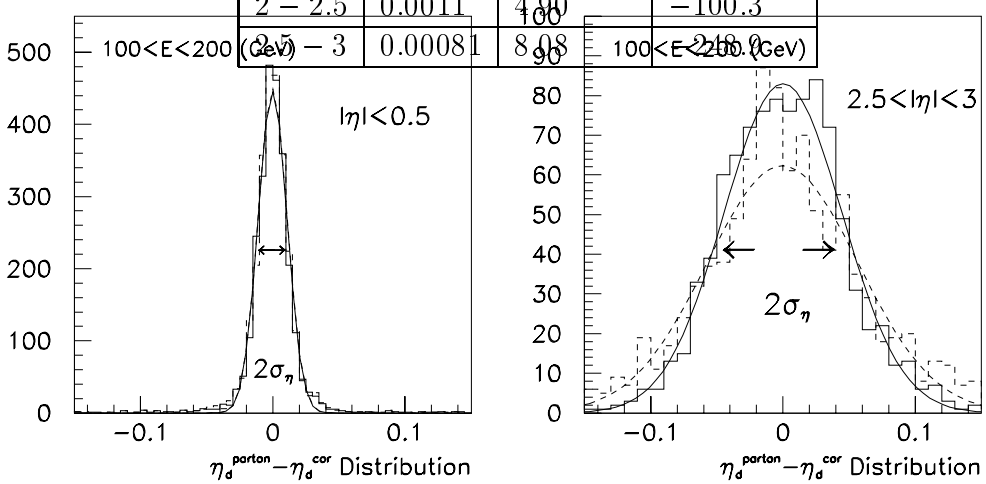

Figure 6.11: HERWIG simulation of the jet η resolution. $\eta_d^{parton} - \eta_d^{cor}$ distributions are shown in solid line and $\eta_d^{parton} - \eta_d^{reco}$ in dashed line.

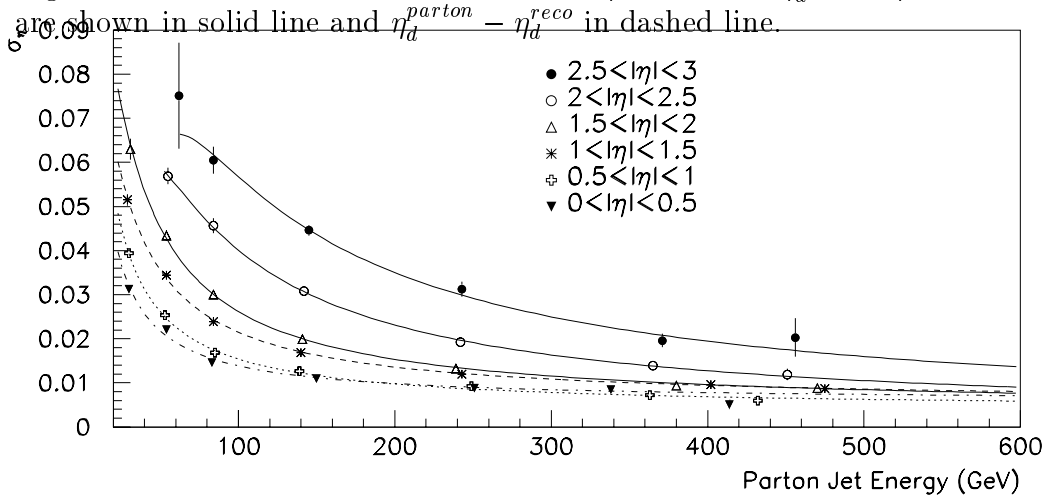

Figure 6.12: $\sigma_\eta(E, \eta_d)$ as a function of the parton jet energy using a HERWIG simulation.

6.5 Smearing Correction to the Jet Cross Sections

6.5.1 Smeared Distributions

The inclusive double differential jet cross section is experimentally determined from two measured jet quantities, E_T and η. In general, if a particular physics quantity is well described by a function $F \equiv F(X)$, it can be determined by measuring the variable X. Every measured quantity has an error associated with the measuring process. If $F(X)$ is binned in terms of X and the distribution of the variable X is described by the probability density function $G(Y - \overline{X})$, with a mean $\overline{X}$ and a variance $\sigma_{\overline{X}}$, the result of the measurement will be the smeared distribution $f(Y)$, related to $F(X)$ through the integral:

$$f(Y) = \int G(Y - X)\, F(X)\, dX\,.$$

If both the resolution function $G(Y - X)$ and the measured distribution $f(Y)$ are known, F(X) can be calculated numerically by solving an infinite system of inhomogeneous linear equations which may be conveniently truncated. If $X_j \equiv Y$ and $X_i \equiv X$, the integral becomes:

$$f(X_j) = \sum_{X_i} C(X_j, X_i) F(X_i)\,,$$

where $i = 1, 2, \ldots, \infty$ and $j = 1, 2, \ldots, \infty$.

In the case of the jet cross section, assuming perfect energy response, the smeared cross section f is written as a function of the unsmeared cross section F as follows:

$$f(E_T', \eta') = \int G(E_T' - E_T)\, G(\eta' - \eta)\, F(E_T, \eta)\, dE_T d\eta\,,$$

where $G(E'_T - E_T)$ and $G(\eta' - \eta)$ are the E_T and η smearing functions which depend on the E_T and η resolutions, σ_{E_T} and σ_η, respectively. In the experiment, σ_{E_T} and σ_η are not independent. In fact, there is a contribution of the position uncertainty and out of cone showering which is folded into the jet E_T resolution. In addition, the jet η distributions are smeared due to η resolution effects. Figure 6.13 shows in a Monte Carlo simulation that the latter effect is not greater than $1-2\%$ for 0.5 η bins. Therefore, the effect of σ_η can be neglected and the double integral may be approximated by a single integral. The shape of the smearing function $G(E'_T - E_T)$ is very important in the determination of the smearing effect. The excellent energy resolution of the DØ calorimeters for electromagnetic objects allows to study this shape with photon–jet events. One photon and only one jet above 10 GeV were allowed in the events used in this test. The histograms in Figure 6.14 are binned in terms of the jet E_T for photons within a narrow E_T bin simulating monoenergetic photons with perfect resolution. The jet E_T smearing function $G(E'_T - E_T)$ is approximated with a gaussian since the distributions in Figure 6.14 are very well described in that way. Then, the convolution is reduced to:

$$f(E'_T) = \int \frac{1}{\sqrt{2\pi}\sigma_{E_T}} e^{-\frac{(E'_T - E_T)^2}{\sigma^2_{E_T}}} F(E_T)\, dE_T \,.$$

Unfortunately, it is not trivial to find the solution to this equation since the rapid fall of the jet E_T distributions induce large oscillations in $F(E_T)$ when solving the group of linear equations. Therefore, this approach was discarded and another method was developed to obtain the unsmeared distributions.

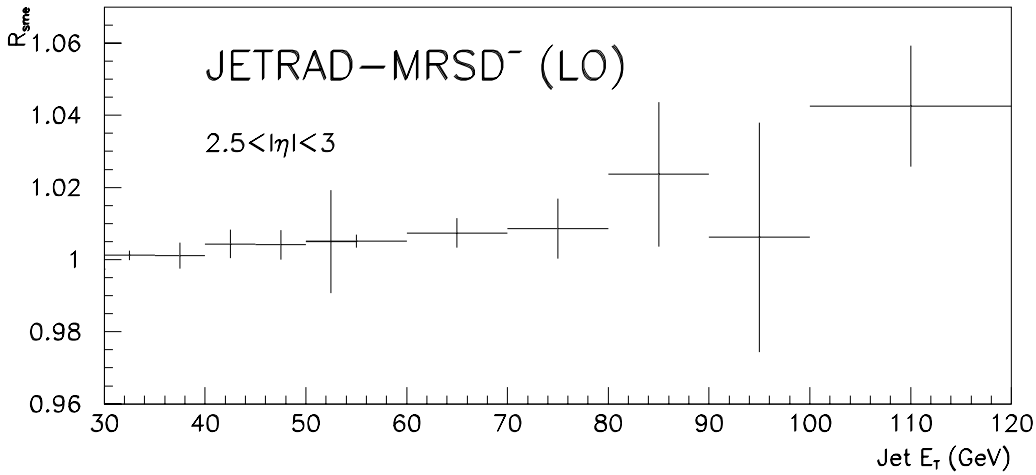

Figure 6.13: R_{sme} is the ratio between the jet cross section smeared both in η and E_T and the jet cross section smeared in E_T only. The smearing effect due to η resolution is less than 2.5% in the very forward region ($2.5 < |\eta| < 3$). The plot corresponds to a Monte Carlo simulation based on JETRAD. The effect is negligible in lower pseudo–rapidity regions since the η resolution is better there.

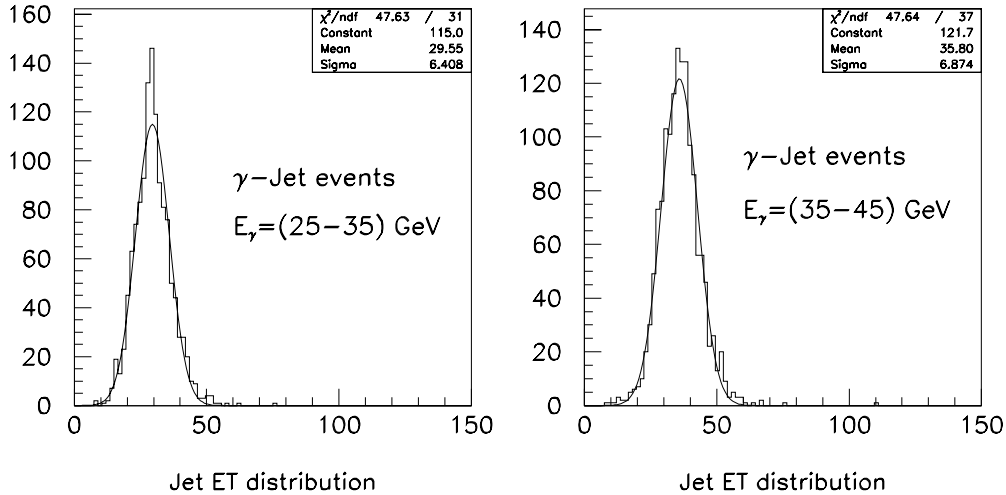

Figure 6.14: The histograms correspond to jet E_T distributions in photon–jet events. The photon is required to have E_T within a narrow bin to simulate monoenergetic photons. The jet distribution is well described by a gaussian function which is used as an approximation to the smearing function.

6.5.2 The Unsmearing Procedure

The inclusive jet cross sections are unsmeared using the following fitting procedure:

- A functional form, which depends on E_T and four independent free parameters, is selected to parametrize the inclusive jet cross section as a function of the jet E_T. The function, called the **hypothesis** , must also be sensitive enough to describe the variety of shapes given by different choices of PDF, μ and λ_c in the theory. Thus, the hypothesis $F(E_T, A, B, C, D)$ is written as:

$$\frac{A}{E_T^B}\left(1 + C\left(\frac{2}{\sqrt{s}}\right)E_T\right)^D \times \frac{1}{e^{A_\circ(E_T)+A_1(E_T)\eta_\circ}} \int_{\eta_\circ}^{\eta_1} e^{A_\circ(E_T)+A_1(E_T)\eta}\, d\eta$$

  where $\eta_\circ$, η_1 define the η bin and:

$$A_\circ(E_T) = \alpha + \beta E_T + \gamma E_T^2$$

$$A_1(E_T) = \alpha' + \beta' E_T + \gamma' E_T^2 \,.$$

  The fixed parameters α, β, γ, α', β',γ' are different for each η bin and were obtained from a JETRAD prediction of the η spectrum which also suggested a quadratic dependence of $A_\circ$ and A_1 on E_T. The η dependent part of the hypothesis function is necessary to follow the shape of the cross sections at high E_T .

- The hypothesis is smeared numerically according to the formula:

$$f(E_T', A, B, C, D) = \int G(E_T' - E_T)\, F(E_T, A, B, C, D)\, dE_T \,,$$

where $G(E'_T - E_T)$ is a gaussian which variance is the jet E_T resolution. Finally, the **smeared hypothesis** , $f(E'_T, A, B, C, D)$ is fit to the inclusive jet cross section.

- The fit provides the parameters A, B, C, D, which determine both the hypothesis and the smeared hypothesis. To correct for the E_T resolution effect, the measured cross section as a function of the jet corrected E_T , must be divided by:

$$R_{res} = \frac{f(E'_T, A, B, C, D)}{F(E_T, A, B, C, D)} .$$

The correction for E_T resolution contributes a systematic error in the inclusive jet cross sections. The most important sources of this uncertainty are:

- The choice of the function proposed as the hypothesis and the fitting procedure.
- The dependence of the unsmearing method on the statistical fluctuations of the data.
- The error in the jet E_T resolution.

6.5.3 Monte Carlo Simulation

A Monte Carlo simulation was conducted to study the contribution of the unsmearing correction to the inclusive jet cross section error. The simulation is based on the generation of JETRAD cross sections in the LO approximation using MRSD$^-$ parton distribution functions. The same binning was used to obtain the jet cross section measurement and the JETRAD predictions to make the simulation more realistic.

Errors due to the Fitting Procedure and Statistical Fluctuations

The fitting procedure and the statistical fluctuations in the data contribute an error to the unsmearing method. The procedure to obtain this contribution is the following:

- The cross sections obtained with JETRAD are taken as the true inclusive jet cross sections and are called **theory.**

- The smeared theory cross sections are obtained by smearing each generated jet using the E_T resolution parametrizations. They are called **simulated data** because they play the role of the data points.

- Realistic statistical errors are included in the simulated data by assigning the same relative statistical errors obtained in the measurement. The statistical fluctuations are included assuming that the simulated data points can fluctuate with gaussian probability around the original mean value. The variance associated with the gaussian distributions are the statistical errors taken from real data. Ten different sets of simulated data points are generated following this technique.

- The unsmearing method is applied to the simulated data in the same way it was described for real data. Once the hypothesis, $F(E_T)$, and the smeared hypothesis, $f(E'_T)$, are determined from the fitting procedure, the smearing correction is calculated as:

  $$R_{res}^{uns} = \frac{f(E'_T)}{F(E_T)} \, .$$

  But now, the ratio R_{res}^{uns}, obtained with the unsmearing technique, can be compared with the true ratio R_{res}^{true} given by:

$$R_{res}^{true} = \frac{simulated\,data}{theory}\,.$$

The process is repeated for the ten sets of simulated data points to get an estimate of the effect of the statistical fluctuations on the accuracy of the method. The difference between R_{res}^{true} and R_{res}^{uns} provides a systematic uncertainty associated with the choice of the function and the fit procedure.

The plots in the top of Figure 6.15 show both R_{res}^{uns} and R_{res}^{true} as a function of corrected jet E_T for the very central and very forward regions ($0 < |\eta| < 0.5$ and $2.5 < |\eta| < 3$). The difference between the two ratios is of the order of $0 - 10\%$. The plots in the bottom of Figure 6.15 show that the hypothetical change in the smearing correction due to statistical fluctuations is less than 0.5% in the central region and less than 5% in the forward.

Error due to the jet E_T Resolution Uncertainty

One of the largest contributions to the error in the unsmearing correction is the uncertainty in the jet E_T resolution functions. This contribution is obtained directly from real data using upper and lower estimates of the jet E_T resolutions in the unsmearing procedure. The results are discussed in the following section.

6.5.4 Results

The fits of $f(E_T', A, B, C, D)$ to the data are presented and displayed in Table 6.10 and Figure 6.16. The total E_T dependent errors added in quadrature to the statistical errors are used in the fit. The E_T resolution corrections to the inclusive jet cross sections are shown in Figure 6.17. Besides the error in the unsmearing

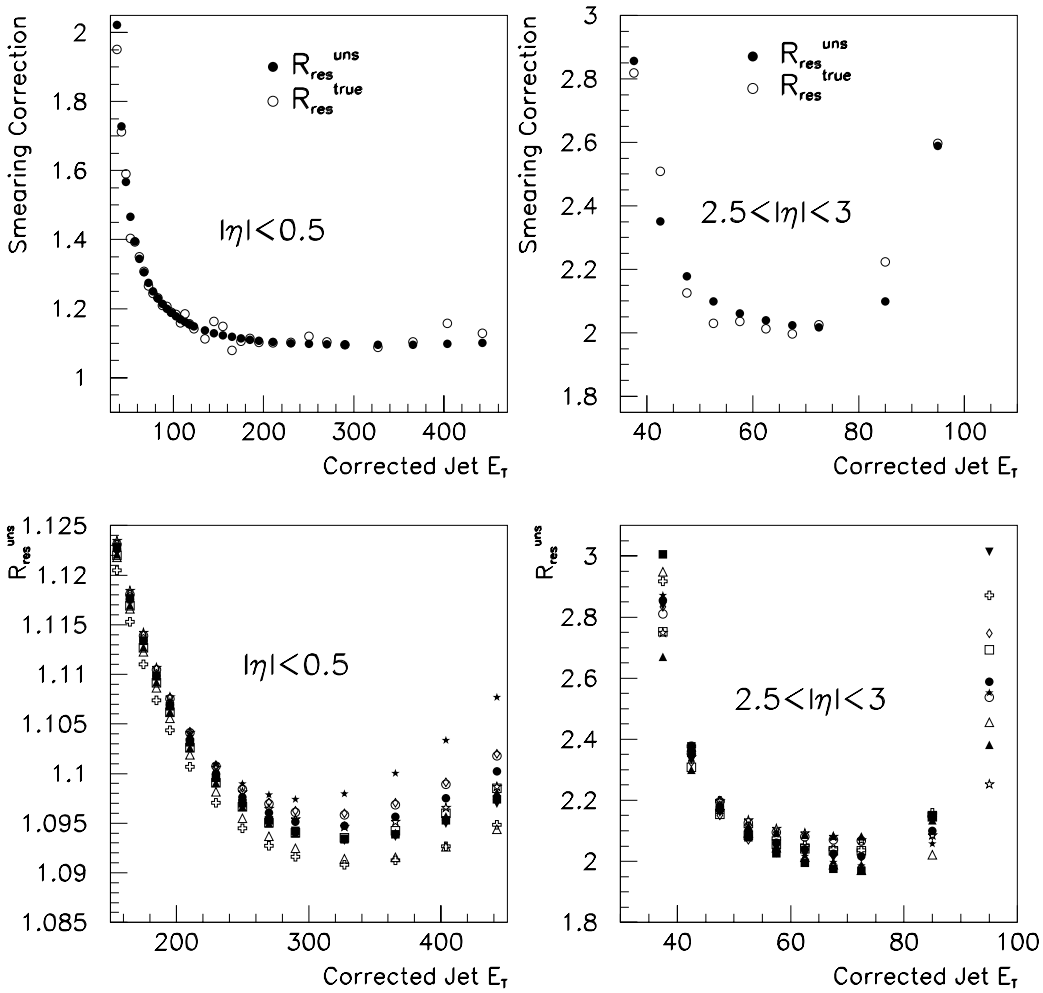

Figure 6.15: Monte Carlo simulation study using JETRAD. Top: comparison between the true smearing effect R_{res}^{true} and the correction R_{res}^{uns} to the cross section obtained with the unsmearing procedure. Bottom: hypothetical change in the smearing correction due to statistical fluctuations of the data.

method, the E_T resolution measurement also contributes to the total cross section uncertainty. The sources are the energy scale correction, the cuts applied to the dijet and $\gamma - jet$ samples and the parametrization. The resolutions were moved within the energy scale uncertainty band and they were also shifted up and down by a 10% to consider the error in the sample selection and fit. The unsmeared distributions obtained using these modified resolutions provided an estimate of the contribution of the E_T resolution uncertainty to the total cross section error. This error dominates at low E_T, ranging from a 10% at 35 GeV to a 2% at 400 GeV in the central η region. In the forward region, it ranges from a 10% at 35 GeV to a 5% at 95 GeV.

Table 6.10: Parametrizations of the inclusive jet cross section hypotheses as a function of the corrected jet E_T for different η_d regions.

η_d	$ln\,A$	B	C	D
$0-0.5$	21.74	4.45	-0.50	22.65
$0.5-1$	22.81	4.77	-1.70	4.43
$1-1.5$	24.28	5.17	-2.41	2.13
$1.5-2$	19.74	3.87	-1.32	16.14
$2-2.5$	20.56	4.19	-3.94	5.18
$2.5-3$	18.90	3.61	-6.57	5.33

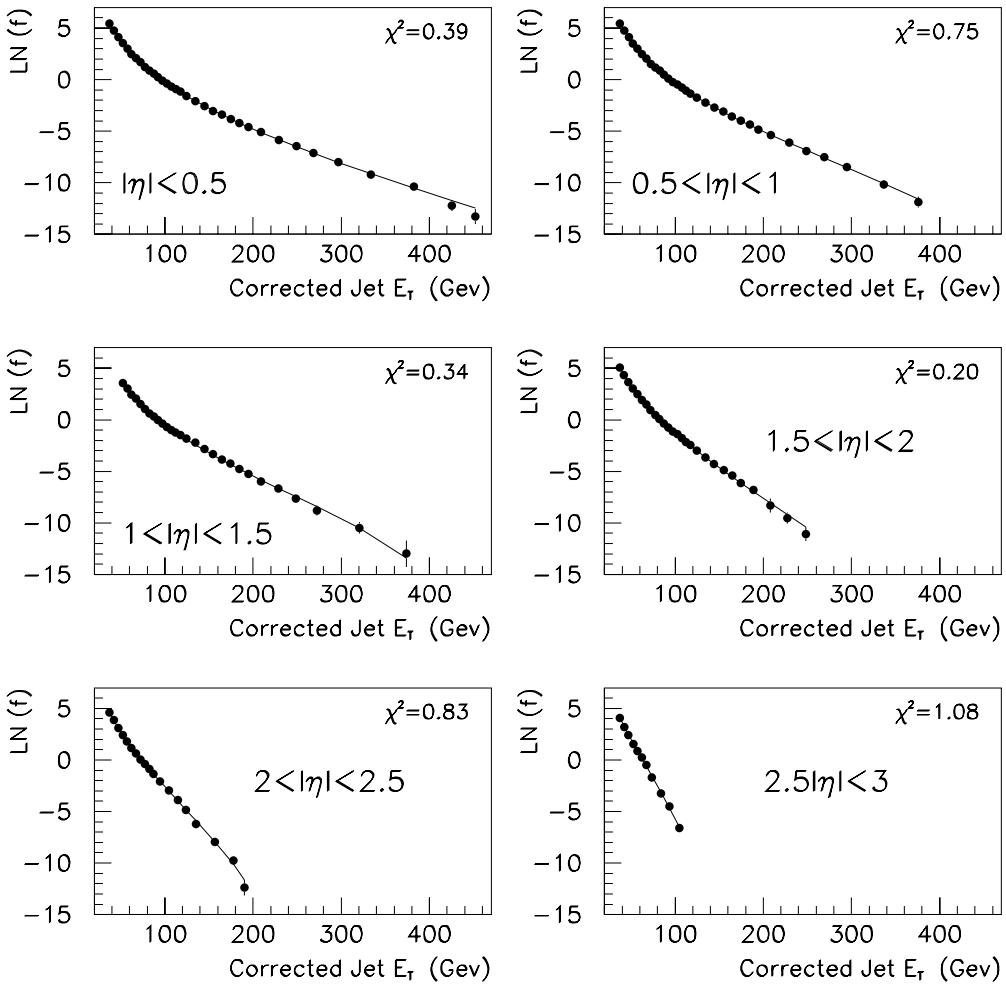

Figure 6.16: Solid lines: smeared hypothesis, $f(E_T', A, B, C, D)$, fit to the corrected jet cross sections measured in different η regions. The data points are plotted in circles

.

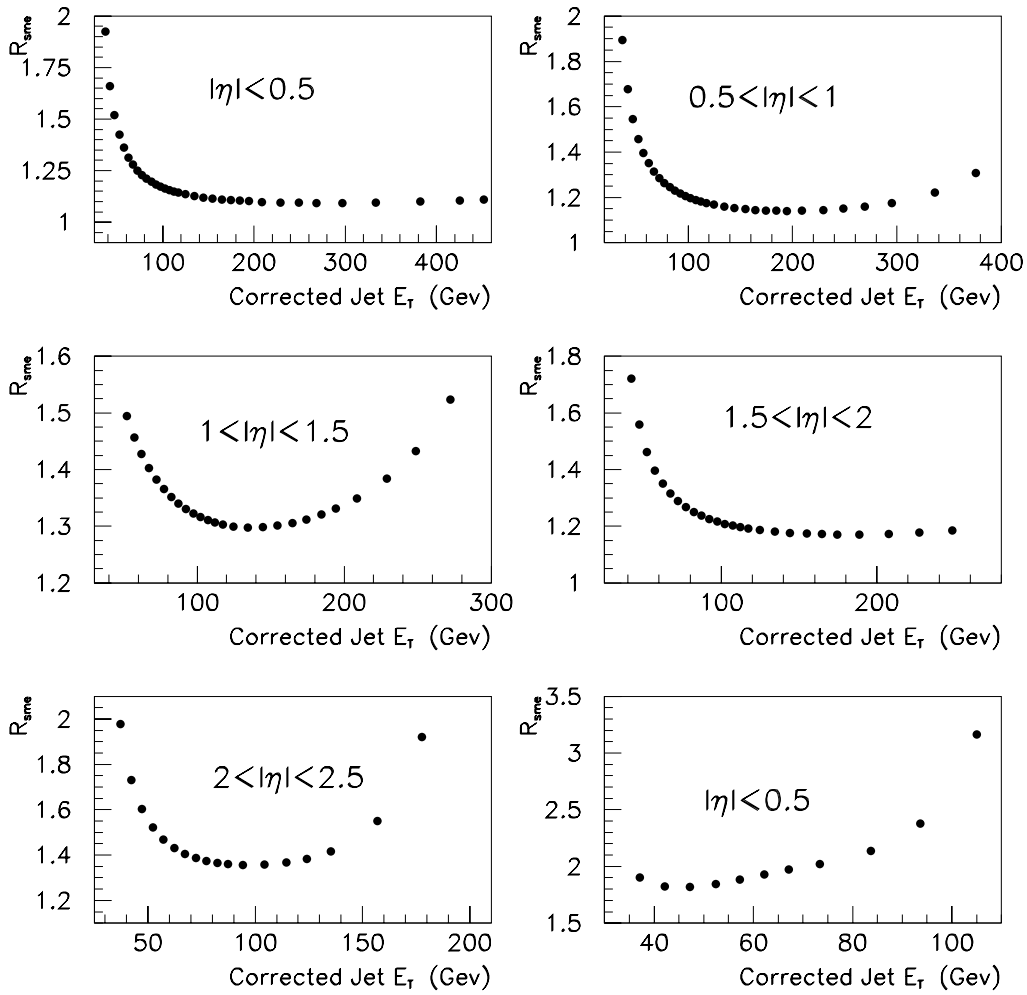

Figure 6.17: Corrections, R_{sme}, for E_T resolution smearing applied to jet cross sections measured in different η regions.

Chapter 7

Results and Conclusion

7.1 Inclusive Jet Cross Sections

7.1.1 Experimental Determination of $< d^2\sigma/dE_T d\eta >$

The double differential jet cross section with respect to the jet pseudo–rapidity and transverse energy is defined as:

$$\frac{d^2\sigma}{dE_T d\eta}.$$

In the experiment, the jet data sample is not taken with a single trigger. Therefore, each individual run and trigger provides an independent measurement of the cross section. The best way to combine these measurements is by calculating an effective luminosity weighted average of the cross sections measured in each run for a particular trigger:

$$\frac{d^2\sigma}{dE_T d\eta} = \sum_i \frac{L_i^{eff}}{L_T^{eff}} \frac{d^2\sigma_i}{dE_T d\eta}$$

where the sum is over all the available runs, and L_i^{eff}, L_T^{eff} are the effective luminosities of run i and the whole sample respectively. In addition, the measured differential cross section is binned in terms of E_T and η. Then,

$$\langle\frac{d^2\sigma}{dE_T d\eta}\rangle(p\overline{p} \rightarrow jet + X) = \frac{N}{L_T^{eff} \times \Delta E_T \times \Delta\eta \times \varepsilon},$$

where the brackets denote an average over a particular E_T and η bin, ΔE_T and $\Delta\eta$ are the bin sizes, $N = \sum_i N_i$ is the sum over the runs of the number of jets in the bin and ε is the product of the efficiencies associated with the measurement.

The number of jets in a bin, N, obeys a poisson distribution. If the total number of jets in the sample, N_T, is much greater than N, the statistical error on the cross section in one bin is:

$$\frac{\sqrt{N}}{L^{eff} \times \Delta E_T \times \Delta\eta \times \varepsilon}.$$

The inclusive differential jet cross sections were measured as a function of the jet E_T in *six* different η bins as shown in Table 7.1. The measurement was not extended below the quoted E_T limits due to the large uncertainties associated with jet definition, energy scale and resolution corrections, trigger and reconstruction efficiencies.

Table 7.1: Kinematic range covered by the DØ measurement of the inclusive jet cross section.

Region	η range	E_T^{min} (GeV)
CT1	$[0, 0.5]$	35
CT2	$[0.5, 1]$	35
IC1	$[1, 1.5]$	50
IC2	$[1.5, 2]$	35
FW1	$[2, 2.5]$	35
FW2	$[2.5, 3]$	35

The calculation of the jet cross section from the reconstructed jet variables was performed in several steps:

- The events which did not pass the $R_{\not{E}_T}$ cut and the jets not passing the standard cuts were removed from the sample.

- The energy and E_T of the jets in the remaining sample were corrected back to the parton jet level. The jet physics η was corrected for reconstruction bias.

- Jet E_T distributions were obtained for each trigger–filter in every η region. Each jet is an entry which was given a weight equal to the inverse of the cut efficiencies. The data points were plotted in the mean value of each E_T bin.

- The E_T distributions were normalized by the corresponding trigger effective luminosity and bin sizes. Since the trigger and reconstruction inefficiencies in the ranges of interest are small compared to the uncertainty in the energy corrections or the luminosity, they were included as a contribution to the total systematic error and ε was set to 1.

- For each particular η region, the E_T spectrum defined in table7.1 was obtained from the five cross sections measured with the jet triggers. JET_MIN was used in the lowest E_T range and JET_MAX in the highest E_T range. The information was extracted from the trigger which provided the highest statistics with the highest efficiency. For every data point, the trigger efficiency was always required to be greater than 95%.

- Finally, the six cross sections were unsmeared to remove E_T resolution effects.

7.1.2 Statistical and Systematic Uncertainties

The statistical errors are not an important source of error in most of the kinematic range covered by the DØ measurement. For example, in the CT1 region, it is always less than 5% below 250 GeV.

The sources of systematic uncertainties were already discussed in chapter 6. Their contribution to the total systematic error of the inclusive jet cross section measurement can be summarized as follows:

- The **Trigger efficiencies** are greater than 95% in the measured E_T, η range except in the IC region where the turn on of the triggers as a function of E_T is very slow. In this range, the trigger E_T thresholds are not close enough to compensate the slow turn on. Therefore, the triggers run out of statistics before the one with higher E_T threshold is fully efficient. Since the cross sections are not corrected for trigger efficiency, there is an error which is less than 5% in all pseudo–rapidity bins except in the IC region where it may be as large as 10%.

- The **jet cuts** and the efficiency correction contribute an average 2% error to the jet cross sections. The effect of the remaining contamination is within statistical errors except at low E_T in the CT regions where it may be as large as a 3%.

- The η **bias** correction is obtained from a Monte Carlo simulation. There is a large uncertainty associated with this correction since the bias is very dependent on the Monte Carlo generator and the hadronization model. The error contributed to the cross section ranges between a 1% in the central region to a 5% in the forward.

- The **energy scale** uncertainty is the largest contribution to the total systematic error in the jet cross sections. In the CT1 region, it ranges from 20% at $E_T = 35$ GeV to 50% at 300 GeV. As the slope of the distributions get steeper at high pseudo–rapidities the energy scale error becomes more important. In the FW2 region, it ranges from 25% at $E_T = 35$ GeV to 80% at 95 GeV.

- The contribution of the **unsmearing correction** is given by the error in the E_T resolution measurement and the unsmearing procedure. It ranges from 10% at 35 GeV to 2% at 400 GeV in the central pseudo–rapidity region and from 12% at 35 GeV to 8% at 95 GeV in the forward region. Smearing corrections due to η resolution effects are not applied since they range from less than 1% in the CT1 region to less than 2.5% in the FW2 bin.

- The uncertainty in the **luminosity calculation** is another important source of error. It contributes a 12% uncertainty in the absolute scale of the jet cross sections.

Assuming these errors are independent from each other, the total systematic uncertainties in the inclusive jet cross section measurements were obtained by adding in quadrature the percent errors of all the contributions.

7.1.3 Results

The DØ inclusive jet cross section measurements are presented and displayed in Tables 7.2–7.7 and Figures 7.1–7.3. The solid bars are the statistical errors and the dotted bars are the total systematic errors obtained by adding all the percent contributions in quadrature. The jet E_T is scaled back to the parton jet level

and the cross sections are fully corrected for η bias, cut efficiencies and resolution effects.

DØ has measured the jet cross sections over more than 8 orders of magnitude in six η bins covering the pseudo–rapidity range $|\eta| < 3$. The highest jet has a transverse energy of 450 GeV and a pseudo–rapidity $\eta = 0.1$. The forward calorimeters detected and measured jets with energies of the order of 700 GeV. The highest E_T values kinematically allowed in the six η regions are 900, 795, 580, 380, 233 and 140 GeV respectively.

Table 7.2: DØ inclusive double differential jet cross section as a function of jet E_T in the CT1 region ($|\eta| < 0.5$). The jet E_T is in GeV and the cross section in (nb/GeV). The E_T spectrum was divided into 5, 10, 20 and 40 GeV bins as E_T increases.

Jet E_T	$\langle d^2\sigma/dE_T d\eta \rangle$	Stat. Error	+ Syst. Error	− syst. Error
37.2	$0.121E+03$	$\pm 0.249E+01$	$+0.362E+02$	$-0.320E+02$
42.2	$0.707E+02$	$\pm 0.177E+01$	$+0.198E+02$	$-0.175E+02$
47.2	$0.404E+02$	$\pm 0.128E+01$	$+0.120E+02$	$-0.110E+02$
52.3	$0.238E+02$	$\pm 0.949E+00$	$+0.573E+01$	$-0.562E+01$
57.3	$0.147E+02$	$\pm 0.728E+00$	$+0.356E+01$	$-0.350E+01$
62.3	$0.917E+01$	$\pm 0.566E+00$	$+0.248E+01$	$-0.200E+01$
67.2	$0.628E+01$	$\pm 0.462E+00$	$+0.147E+01$	$-0.151E+01$
72.4	$0.436E+01$	$\pm 0.381E+00$	$+0.888E+00$	$-0.114E+01$
77.3	$0.281E+01$	$\pm 0.270E-01$	$+0.635E+00$	$-0.633E+00$
82.4	$0.200E+01$	$\pm 0.226E-01$	$+0.458E+00$	$-0.426E+00$
87.4	$0.150E+01$	$\pm 0.195E-01$	$+0.324E+00$	$-0.339E+00$
92.4	$0.108E+01$	$\pm 0.165E-01$	$+0.254E+00$	$-0.251E+00$
97.4	$0.785E+00$	$\pm 0.140E-01$	$+0.198E+00$	$-0.168E+00$
102.4	$0.591E+00$	$\pm 0.121E-01$	$+0.143E+00$	$-0.134E+00$
107.4	$0.451E+00$	$\pm 0.105E-01$	$+0.104E+00$	$-0.949E-01$
112.4	$0.348E+00$	$\pm 0.920E-02$	$+0.798E-01$	$-0.796E-01$
117.4	$0.271E+00$	$\pm 0.810E-02$	$+0.600E-01$	$-0.708E-01$
124.7	$0.177E+00$	$\pm 0.462E-02$	$+0.475E-01$	$-0.387E-01$
134.7	$0.110E+00$	$\pm 0.363E-02$	$+0.276E-01$	$-0.264E-01$
144.7	$0.691E-01$	$\pm 0.287E-02$	$+0.178E-01$	$-0.174E-01$
154.6	$0.424E-01$	$\pm 0.224E-02$	$+0.132E-01$	$-0.836E-02$
164.7	$0.303E-01$	$\pm 0.677E-03$	$+0.774E-02$	$-0.767E-02$
174.7	$0.196E-01$	$\pm 0.545E-03$	$+0.607E-02$	$-0.474E-02$
184.5	$0.133E-01$	$\pm 0.449E-03$	$+0.404E-02$	$-0.384E-02$
194.7	$0.896E-02$	$\pm 0.368E-03$	$+0.259E-02$	$-0.212E-02$
208.8	$0.550E-02$	$\pm 0.204E-03$	$+0.158E-02$	$-0.172E-02$
229.1	$0.262E-02$	$\pm 0.107E-03$	$+0.105E-02$	$-0.770E-03$
249.4	$0.147E-02$	$\pm 0.807E-04$	$+0.377E-03$	$-0.440E-03$
268.4	$0.731E-03$	$\pm 0.570E-04$	$+0.432E-03$	$-0.260E-03$
296.9	$0.309E-03$	$\pm 0.263E-04$	$+0.104E-03$	$-0.111E-03$
333.4	$0.937E-04$	$\pm 0.145E-04$	$+0.759E-04$	$-0.561E-04$
382.6	$0.288E-04$	$\pm 0.817E-05$	$+0.320E-04$	$-0.201E-04$
425.5	$0.450E-05$	$\pm 0.287E-05$	$+0.140E-04$	$-0.279E-05$
451.9	$0.150E-05$	$\pm 0.167E-05$	$+0.302E-05$	$-0.156E-05$

Table 7.3: DØ inclusive double differential jet cross section as a function of jet E_T in the CT2 η region ($0.5 < |\eta| < 1$).The jet E_T is in GeV and the cross section in (nb/GeV). The E_T spectrum was divided into 5, 10, 20 and 40 GeV bins as E_T increases.

Jet E_T	$\langle d^2\sigma/dE_T d\eta \rangle$	Stat. Error	+ Syst. Error	− Syst. Error
37.2	$0.123E+03$	$\pm 0.249E+01$	$+0.343E+02$	$-0.300E+02$
42.2	$0.694E+02$	$\pm 0.176E+01$	$+0.201E+02$	$-0.183E+02$
47.3	$0.399E+02$	$\pm 0.128E+01$	$+0.100E+02$	$-0.981E+01$
52.3	$0.230E+02$	$\pm 0.946E+00$	$+0.610E+01$	$-0.537E+01$
57.4	$0.146E+02$	$\pm 0.736E+00$	$+0.328E+01$	$-0.339E+01$
62.2	$0.883E+01$	$\pm 0.564E+00$	$+0.289E+01$	$-0.184E+01$
67.3	$0.597E+01$	$\pm 0.457E+00$	$+0.136E+01$	$-0.175E+01$
72.4	$0.348E+01$	$\pm 0.345E+00$	$+0.867E+00$	$-0.626E+00$
77.3	$0.254E+01$	$\pm 0.260E-01$	$+0.568E+00$	$-0.558E+00$
82.4	$0.195E+01$	$\pm 0.227E-01$	$+0.363E+00$	$-0.409E+00$
87.3	$0.135E+01$	$\pm 0.187E-01$	$+0.399E+00$	$-0.329E+00$
92.3	$0.926E+00$	$\pm 0.154E-01$	$+0.239E+00$	$-0.214E+00$
97.4	$0.666E+00$	$\pm 0.130E-01$	$+0.162E+00$	$-0.141E+00$
102.3	$0.509E+00$	$\pm 0.114E-01$	$+0.117E+00$	$-0.115E+00$
107.4	$0.387E+00$	$\pm 0.988E-02$	$+0.845E-01$	$-0.911E-01$
112.4	$0.292E+00$	$\pm 0.856E-02$	$+0.748E-01$	$-0.686E-01$
117.4	$0.221E+00$	$\pm 0.742E-02$	$+0.541E-01$	$-0.498E-01$
124.6	$0.152E+00$	$\pm 0.434E-02$	$+0.362E-01$	$-0.337E-01$
134.5	$0.918E-01$	$\pm 0.337E-02$	$+0.265E-01$	$-0.211E-01$
144.4	$0.580E-01$	$\pm 0.267E-02$	$+0.143E-01$	$-0.145E-01$
154.7	$0.391E-01$	$\pm 0.219E-02$	$+0.845E-02$	$-0.922E-02$
164.6	$0.246E-01$	$\pm 0.622E-03$	$+0.688E-02$	$-0.614E-02$
174.6	$0.166E-01$	$\pm 0.511E-03$	$+0.460E-02$	$-0.431E-02$
184.7	$0.111E-01$	$\pm 0.418E-03$	$+0.316E-02$	$-0.321E-02$
194.6	$0.700E-02$	$\pm 0.332E-03$	$+0.260E-02$	$-0.191E-02$
208.7	$0.400E-02$	$\pm 0.178E-03$	$+0.134E-02$	$-0.134E-02$
229.4	$0.193E-02$	$\pm 0.949E-04$	$+0.554E-03$	$-0.565E-03$
248.9	$0.847E-03$	$\pm 0.630E-04$	$+0.488E-03$	$-0.268E-03$
269.4	$0.483E-03$	$\pm 0.480E-04$	$+0.143E-03$	$-0.205E-03$
295.0	$0.174E-03$	$\pm 0.206E-04$	$+0.129E-03$	$-0.100E-03$
336.5	$0.307E-04$	$\pm 0.885E-05$	$+0.498E-04$	$-0.171E-04$
375.7	$0.529E-05$	$\pm 0.399E-05$	$+0.247E-04$	$-0.353E-05$

Table 7.4: DØ inclusive double differential jet cross section as a function of jet E_T in the IC1 η region ($1 < |\eta| < 1.5$). The jet E_T is in GeV and the cross section in (nb/GeV). The E_T spectrum was divided into 5, 10, 20 and 40 GeV bins as E_T increases.

Jet E_T	$\langle d^2\sigma/dE_T d\eta \rangle$	Stat. Error	+ Syst. Error	− Syst. Error
52.3	$0.237E+02$	$\pm 0.973E+00$	$+0.587E+01$	$-0.524E+01$
57.3	$0.141E+02$	$\pm 0.740E+00$	$+0.352E+01$	$-0.322E+01$
62.1	$0.804E+01$	$\pm 0.554E+00$	$+0.261E+01$	$-0.201E+01$
67.2	$0.548E+01$	$\pm 0.453E+00$	$+0.109E+01$	$-0.122E+01$
72.3	$0.327E+01$	$\pm 0.113E+00$	$+0.816E+00$	$-0.801E+00$
77.4	$0.211E+01$	$\pm 0.901E-01$	$+0.530E+00$	$-0.517E+00$
82.4	$0.133E+01$	$\pm 0.712E-01$	$+0.395E+00$	$-0.266E+00$
87.3	$0.102E+01$	$\pm 0.622E-01$	$+0.201E+00$	$-0.232E+00$
92.3	$0.727E+00$	$\pm 0.523E-01$	$+0.189E+00$	$-0.165E+00$
97.4	$0.525E+00$	$\pm 0.443E-01$	$+0.113E+00$	$-0.121E+00$
102.3	$0.377E+00$	$\pm 0.375E-01$	$+0.115E+00$	$-0.781E-01$
107.3	$0.288E+00$	$\pm 0.327E-01$	$+0.560E-01$	$-0.598E-01$
112.0	$0.224E+00$	$\pm 0.288E-01$	$+0.688E-01$	$-0.823E-01$
117.4	$0.174E+00$	$\pm 0.697E-02$	$+0.404E-01$	$-0.360E-01$
124.7	$0.124E+00$	$\pm 0.416E-02$	$+0.273E-01$	$-0.257E-01$
134.6	$0.855E-01$	$\pm 0.346E-02$	$+0.179E-01$	$-0.227E-01$
144.6	$0.459E-01$	$\pm 0.254E-02$	$+0.158E-01$	$-0.113E-01$
154.7	$0.278E-01$	$\pm 0.198E-02$	$+0.831E-02$	$-0.805E-02$
164.7	$0.164E-01$	$\pm 0.547E-03$	$+0.474E-02$	$-0.349E-02$
174.4	$0.109E-01$	$\pm 0.447E-03$	$+0.327E-02$	$-0.368E-02$
184.6	$0.635E-02$	$\pm 0.343E-03$	$+0.224E-02$	$-0.199E-02$
194.5	$0.392E-02$	$\pm 0.271E-03$	$+0.146E-02$	$-0.147E-02$
208.8	$0.189E-02$	$\pm 0.135E-03$	$+0.783E-03$	$-0.535E-03$
228.9	$0.925E-03$	$\pm 0.730E-04$	$+0.322E-03$	$-0.344E-03$
248.7	$0.338E-03$	$\pm 0.452E-04$	$+0.229E-03$	$-0.109E-03$
272.3	$0.985E-04$	$\pm 0.178E-04$	$+0.700E-04$	$-0.558E-04$
320.5	$0.134E-04$	$\pm 0.782E-05$	$+0.168E-04$	$-0.985E-05$
373.8	$0.756E-06$	$\pm 0.227E-05$	$+0.724E-05$	$-0.182E-06$

Table 7.5: DØ inclusive double differential jet cross section as a function of jet E_T in the IC2 η region ($1.5 < |\eta| < 2$). The jet E_T is in GeV and the cross section in (nb/GeV). The E_T spectrum was divided into 5, 10, 20 and 40 GeV bins as E_T increases.

Jet E_T	$\langle d^2\sigma/dE_T d\eta \rangle$	Stat. Error	+ Syst. Error	− Syst. Error
37.2	$0.786E+02$	$\pm 0.208E+01$	$+0.225E+02$	$-0.204E+02$
42.1	$0.443E+02$	$\pm 0.143E+01$	$+0.126E+02$	$-0.115E+02$
47.2	$0.249E+02$	$\pm 0.102E+01$	$+0.603E+01$	$-0.613E+01$
52.3	$0.143E+02$	$\pm 0.745E+00$	$+0.337E+01$	$-0.318E+01$
57.3	$0.881E+01$	$\pm 0.572E+00$	$+0.207E+01$	$-0.208E+01$
62.3	$0.516E+01$	$\pm 0.430E+00$	$+0.149E+01$	$-0.127E+01$
67.3	$0.336E+01$	$\pm 0.343E+00$	$+0.860E+00$	$-0.693E+00$
72.2	$0.198E+01$	$\pm 0.260E+00$	$+0.554E+00$	$-0.506E+00$
77.3	$0.124E+01$	$\pm 0.182E-01$	$+0.285E+00$	$-0.271E+00$
82.3	$0.853E+00$	$\pm 0.150E-01$	$+0.217E+00$	$-0.212E+00$
87.3	$0.558E+00$	$\pm 0.121E-01$	$+0.149E+00$	$-0.131E+00$
92.3	$0.392E+00$	$\pm 0.101E-01$	$+0.908E-01$	$-0.980E-01$
97.4	$0.264E+00$	$\pm 0.826E-02$	$+0.733E-01$	$-0.563E-01$
102.4	$0.213E+00$	$\pm 0.740E-02$	$+0.420E-01$	$-0.517E-01$
107.4	$0.145E+00$	$\pm 0.610E-02$	$+0.438E-01$	$-0.414E-01$
112.4	$0.980E-01$	$\pm 0.501E-02$	$+0.329E-01$	$-0.235E-01$
117.5	$0.721E-01$	$\pm 0.430E-02$	$+0.177E-01$	$-0.217E-01$
124.7	$0.424E-01$	$\pm 0.233E-02$	$+0.137E-01$	$-0.111E-01$
134.5	$0.220E-01$	$\pm 0.168E-02$	$+0.808E-02$	$-0.525E-02$
144.0	$0.117E-01$	$\pm 0.123E-02$	$+0.479E-02$	$-0.446E-02$
155.1	$0.637E-02$	$\pm 0.906E-03$	$+0.115E-02$	$-0.151E-02$
164.8	$0.377E-02$	$\pm 0.249E-03$	$+0.151E-02$	$-0.133E-02$
174.7	$0.188E-02$	$\pm 0.177E-03$	$+0.114E-02$	$-0.398E-03$
188.6	$0.952E-03$	$\pm 0.893E-04$	$+0.239E-03$	$-0.436E-03$
207.7	$0.209E-03$	$\pm 0.420E-04$	$+0.296E-03$	$-0.115E-03$
227.2	$0.618E-04$	$\pm 0.176E-04$	$+0.575E-04$	$-0.431E-04$
248.5	$0.130E-04$	$\pm 0.580E-05$	$+0.111E-04$	$-0.112E-04$

Table 7.6: DØ inclusive double differential jet cross section as a function of jet E_T in the FW1 η region ($2 < |\eta| < 2.5$). The jet E_T is in GeV and the cross section in (nb/GeV). The E_T spectrum was divided into 5, 10 and 20 GeV bins as E_T increases.

Jet E_T	$\langle d^2\sigma/dE_T d\eta \rangle$	Stat. Error	+ Syst. Error	− Syst. Error
37.2	$0.494E+02$	$\pm 0.161E+01$	$+0.147E+02$	$-0.126E+02$
42.2	$0.273E+02$	$\pm 0.112E+01$	$+0.733E+01$	$-0.657E+01$
47.1	$0.139E+02$	$\pm 0.769E+00$	$+0.405E+01$	$-0.364E+01$
52.2	$0.755E+01$	$\pm 0.552E+00$	$+0.177E+01$	$-0.175E+01$
57.2	$0.402E+01$	$\pm 0.396E+00$	$+0.117E+01$	$-0.970E+00$
62.3	$0.221E+01$	$\pm 0.940E-01$	$+0.537E+00$	$-0.515E+00$
67.3	$0.134E+01$	$\pm 0.725E-01$	$+0.338E+00$	$-0.348E+00$
72.4	$0.757E+00$	$\pm 0.542E-01$	$+0.238E+00$	$-0.176E+00$
77.3	$0.490E+00$	$\pm 0.119E-01$	$+0.151E+00$	$-0.139E+00$
82.3	$0.299E+00$	$\pm 0.928E-02$	$+0.791E-01$	$-0.731E-01$
87.3	$0.192E+00$	$\pm 0.742E-02$	$+0.539E-01$	$-0.531E-01$
94.2	$0.903E-01$	$\pm 0.360E-02$	$+0.295E-01$	$-0.267E-01$
104.4	$0.385E-01$	$\pm 0.236E-02$	$+0.132E-01$	$-0.123E-01$
114.5	$0.148E-01$	$\pm 0.148E-02$	$+0.638E-02$	$-0.413E-02$
124.0	$0.563E-02$	$\pm 0.917E-03$	$+0.308E-02$	$-0.187E-02$
135.4	$0.142E-02$	$\pm 0.331E-03$	$+0.909E-03$	$-0.725E-03$
157.0	$0.223E-03$	$\pm 0.495E-04$	$+0.144E-03$	$-0.132E-03$
177.6	$0.300E-04$	$\pm 0.204E-04$	$+0.502E-04$	$-0.235E-04$
190.4	$0.164E-05$	$\pm 0.423E-05$	$+0.491E-05$	$-0.166E-05$

Table 7.7: DØ inclusive double differential jet cross section as a function of jet E_T in the FW2 η region ($2.5 < |\eta| < 3$). The jet E_T is in GeV and the cross section in (nb/GeV). The E_T spectrum was divided into 5 and 10 GeV bins as E_T increases.

Jet E_T	$\langle d^2\sigma/dE_T d\eta \rangle$	Stat. Error	+ Syst. Error	− Syst. Error
37.1	$0.303E+02$	$\pm 0.124E+01$	$+0.962E+01$	$-0.876E+01$
42.2	$0.135E+02$	$\pm 0.809E+00$	$+0.476E+01$	$-0.399E+01$
47.2	$0.612E+01$	$\pm 0.544E+00$	$+0.214E+01$	$-0.199E+01$
52.5	$0.249E+01$	$\pm 0.350E+00$	$+0.888E+00$	$-0.709E+00$
57.3	$0.128E+01$	$\pm 0.253E+00$	$+0.570E+00$	$-0.269E+00$
62.2	$0.664E+00$	$\pm 0.599E-01$	$+0.237E+00$	$-0.223E+00$
67.1	$0.310E+00$	$\pm 0.413E-01$	$+0.121E+00$	$-0.113E+00$
73.4	$0.886E-01$	$\pm 0.158E-01$	$+0.521E-01$	$-0.372E-01$
83.7	$0.181E-01$	$\pm 0.202E-02$	$+0.954E-02$	$-0.675E-02$
93.7	$0.453E-02$	$\pm 0.107E-02$	$+0.355E-02$	$-0.361E-02$
105.0	$0.438E-03$	$\pm 0.272E-03$	$+0.156E-02$	$-0.346E-03$

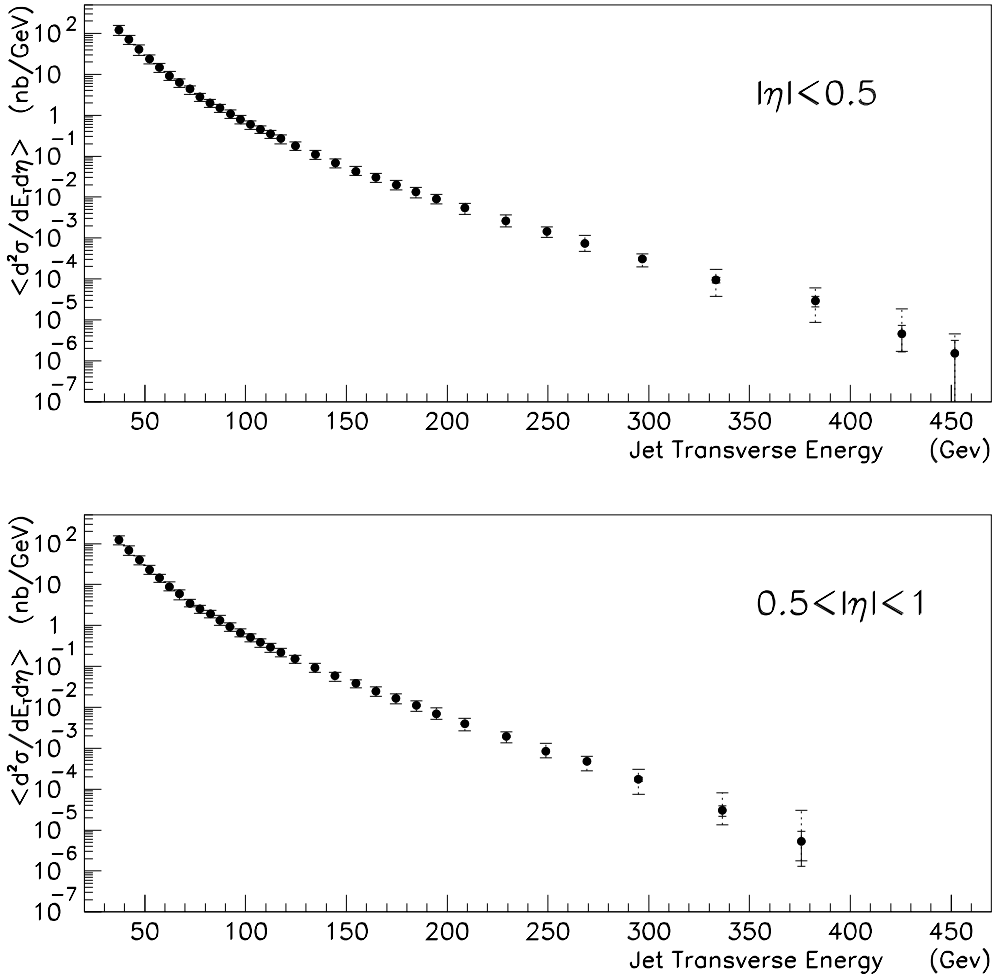

Figure 7.1: DØ inclusive double differential jet cross section as a function of jet E_T in the CT1 and CT2 regions ($|\eta| < 0.5$ and $0.5 < |\eta| < 1$). The solid bars are the statistical errors and the dashed bars are the total systematic errors.

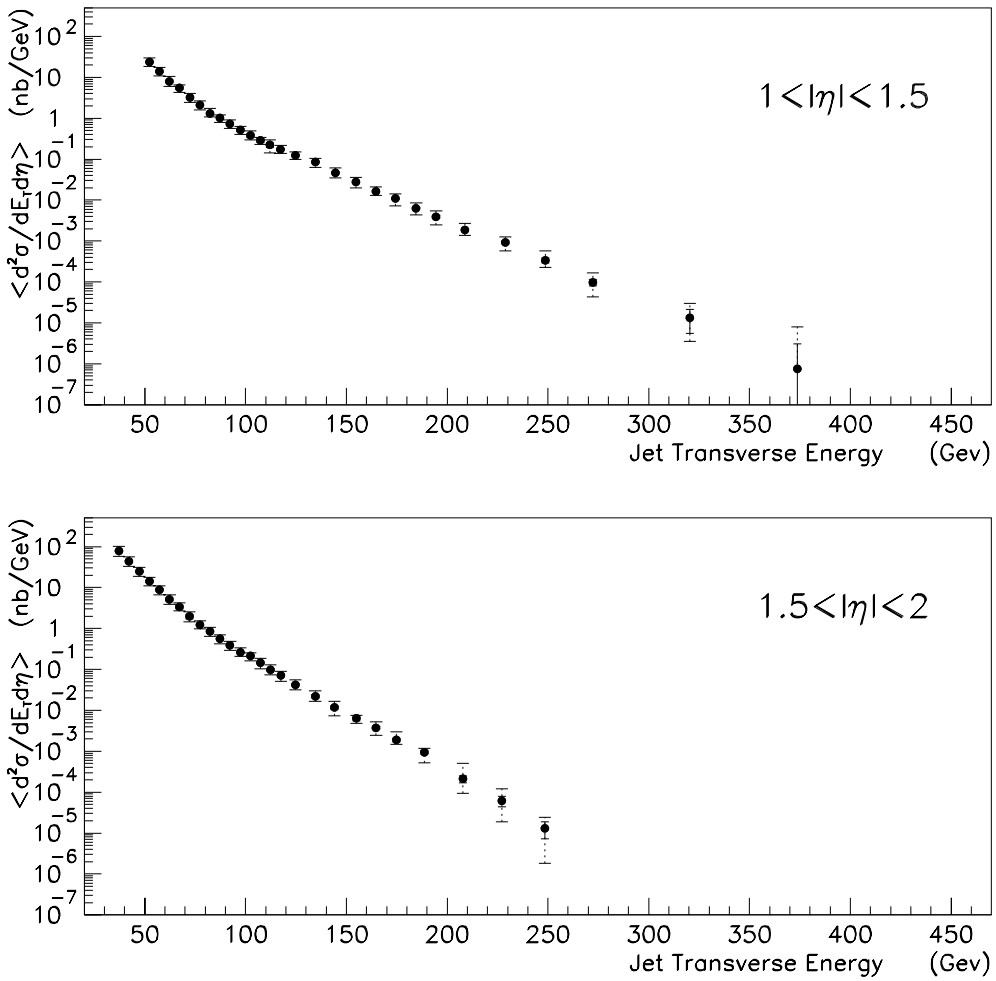

Figure 7.2: DØ inclusive double differential jet cross section as a function of jet E_T in the IC1 and IC2 regions ($1 < |\eta| < 1.5$ and $1.5 < |\eta| < 2$). The solid bars are the statistical errors and the dashed bars are the total systematic errors.

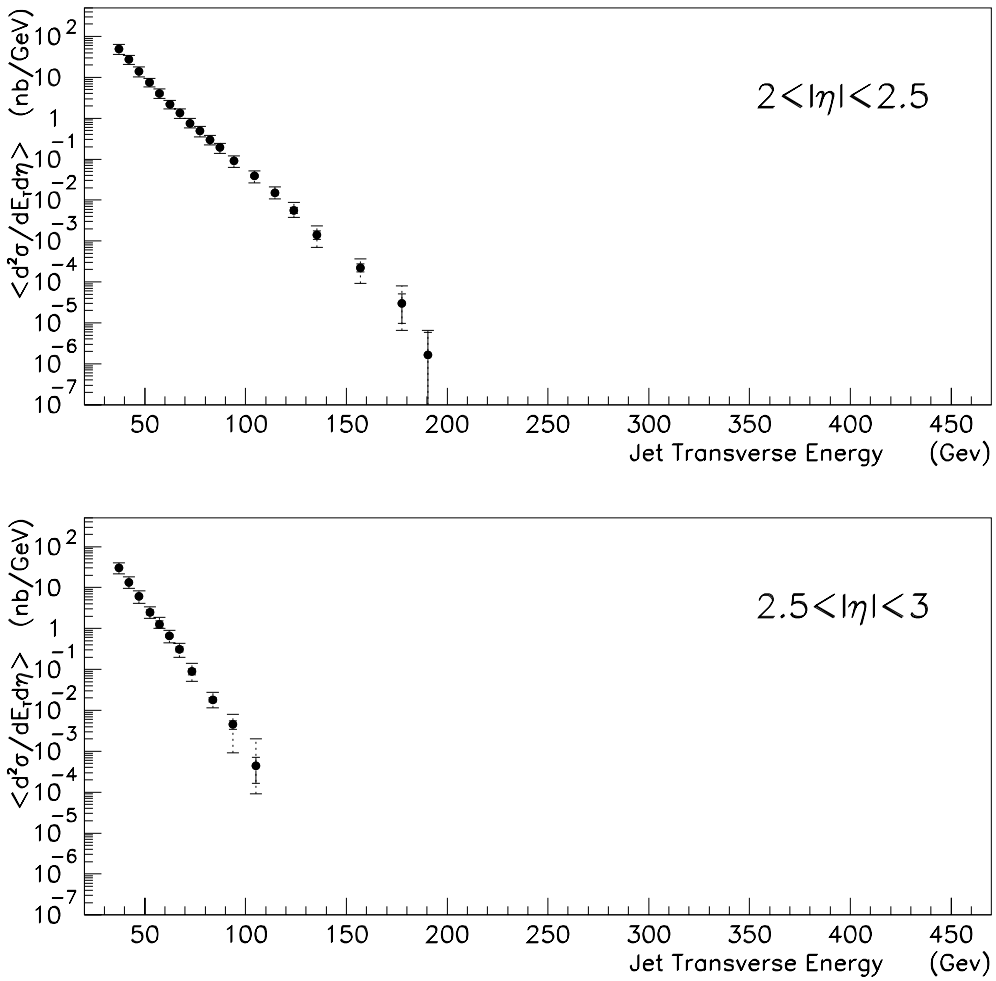

Figure 7.3: DØ inclusive double differential jet cross section as a function of jet E_T in the FW1 and FW2 regions ($2 < |\eta| < 2.5$ and $2.5 < |\eta| < 3$). The solid bars are the statistical errors and the dashed bars are the total systematic errors.

7.1.4 Comparison with QCD Predictions

The Next–to–Leading Order prediction of the inclusive jet cross section by Ellis et al.[48, 49] was used to compare the theory with the experimental measurement. This prediction depends on the choice of the renormalization scale μ, the factorization scale μ_f and the parton distribution functions (PDF).

Figure 7.4 shows the dependence of the inclusive jet cross sections on μ for different values of E_T, η and $\mu = \mu_f$. Although the LO calculation shows a very large dependence on μ, the NLO prediction is less sensitive to the choice of the renormalization scale. The change in the cross section is of the order of $10 - 20\%$ if μ takes values between $E_T/2$ and $2E_T$ in the kinematic range measured with the DØ detector.

A large number of parton distribution functions have been proposed by different groups, based on the available experimental data. The MRS collaboration[27] proposed different sets of PDF's from which HMRSB0 provided the best fit to the experimental data available at the moment of their publication. The CTEQ collaboration[28] also proposed a number of PDF sets. They adopted the following label scheme: CTEQnMX, where n is a version number; M designates the $\overline{MS}$ renormalization scheme; X is absent for the best fits, otherwise it distinguishes the alternative sets within a given scheme. CTEQ2MS includes a singular gluon distribution; CTEQ2MF proposes a flat gluon distribution; and CTEQ2ML uses the LEP value for Λ_{QCD} (220 MeV). The dependence of the inclusive jet cross section on the choice of the PDF set is illustrated in Figure 7.5 for the kinematic range measured at DØ. Hence the uncertainty in the prediction, due to the choice of the PDF set is of the order of 10% if CTEQ2ML is excluded.

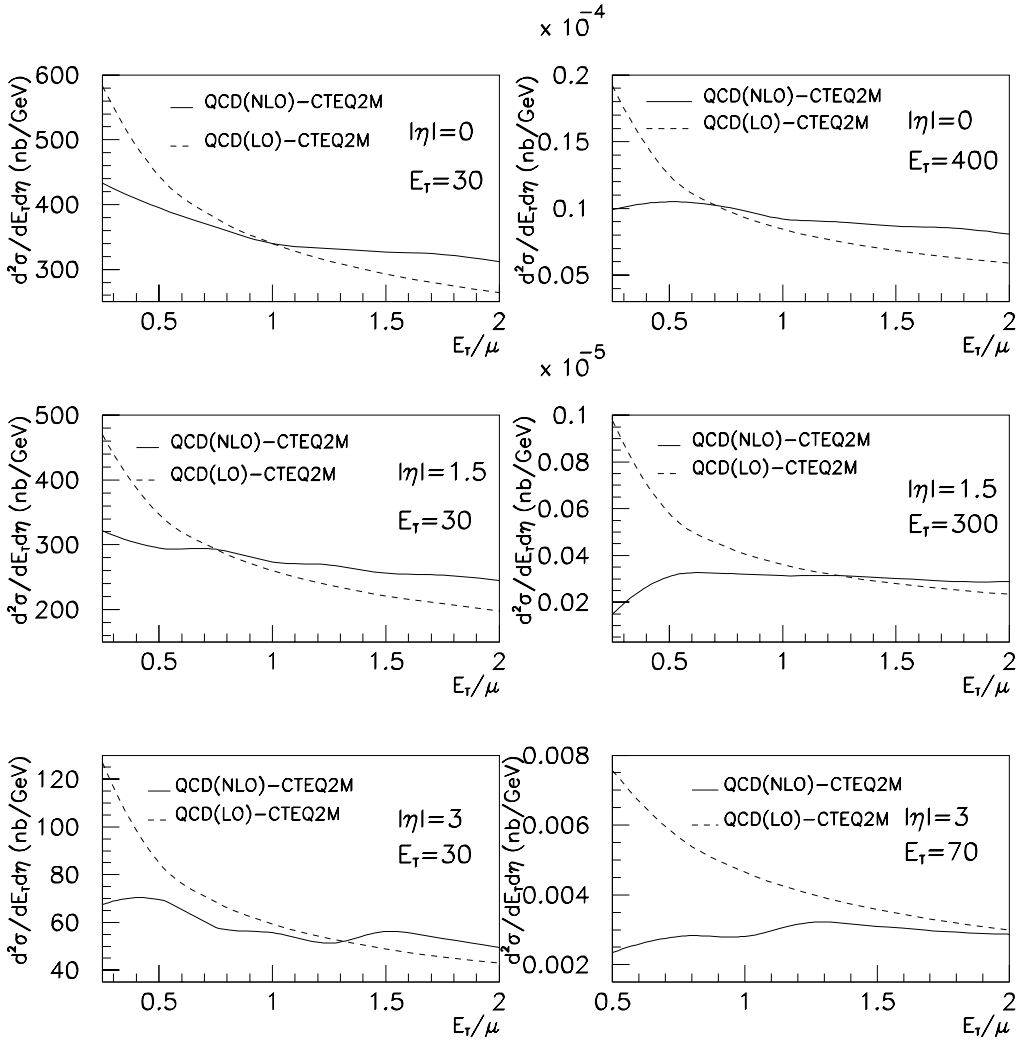

Figure 7.4: Dependence of the EKS QCD prediction of the inclusive jet cross sections in the LO and NLO approximations on the renormalization scale μ.

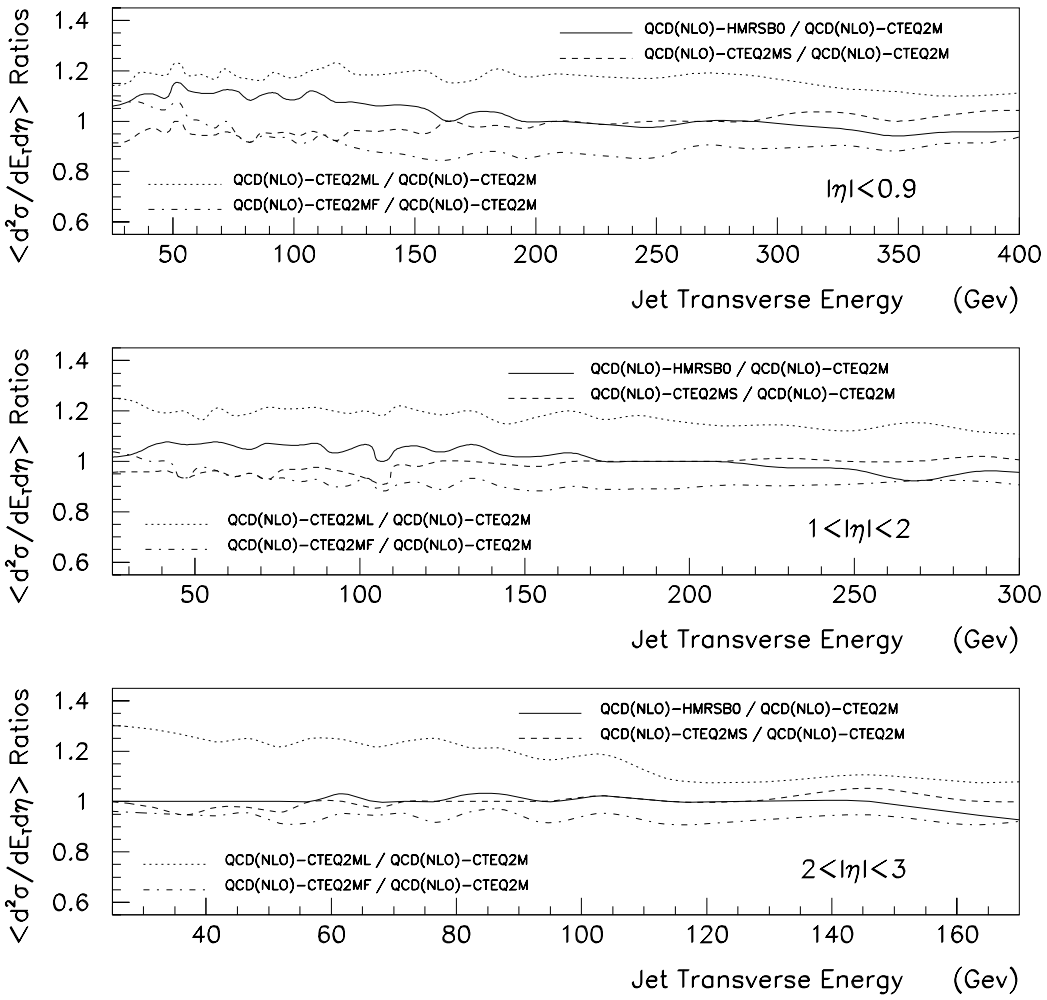

Figure 7.5: Ratios of the EKS predictions of the inclusive jet cross sections in the NLO approximation using different PDF sets. All the sets are compared to the best CTEQ fit, CTEQ2M.

Figures 7.6–7.8 display the double differential jet cross sections measured at DØ in different pseudo–rapidity regions compared with the EKS QCD(NLO) theoretical predictions using CTEQ2M distribution functions. The ratio plots in Figures7.9–7.11 allow a better comparison. There is good agreement between theory and experiment in the central ($|\eta| < 1$) and forward ($2 < |\eta| < 3$) pseudo–rapidity regions for $E_T < 100$ GeV. In the IC region ($1 < |\eta| < 2$), the agreement is marginal in the same E_T range. This region is the least instrumented part of the calorimeter and the systematics are still not well understood there. In all the measured η bins, the ratio between data and theory grows linearly with increasing E_T. This behavior is likely to be originated in the jet energy scale correction. For example, the lack of photon events with $E_{T_\gamma} > 100$ GeV introduces a very large uncertainty in the jet scale since the jet energy response at high E_T is determined as an extrapolation of the low energy response.

The CDF collaboration reported good agreement with the EKS QCD(NLO) prediction in the pseudo–rapidity range $0.1 < |\eta| < 0.7$. They also established a lower limit on the quark compositeness scale, $\Lambda_c > 1.4$ TeV [24, 25]. The UA2 collaboration measured the inclusive jet cross section in the range $|\eta| < 2$ and compared with a LO prediction. They reported good agreement with theory in the central region. Their measurement falls below the theory at high pseudo–rapidities and the disagreement grows as a function of η [23].

7.2 Conclusion

In a $p\overline{p}$ collider, the inclusive differential jet cross section is a basic measurement of the elastic scattering interaction between partons. Therefore, this measurement is a quantitative test of the strong interaction, described by QCD. Using a 13.1 pb^{-1}

sample taken during the $1992 - 1994$ run, DØ has extended the measurement of the double differential inclusive jet cross section to previously unexplored pseudo–rapidity regions. For the first time, this quantity was measured in the range $2 < |\eta| < 3$, providing new experimental results to test the existing theoretical predictions. The data was compared to the QCD calculations at the Next–to–Leading order approximation by Ellis et al.[48, 49]. Good agreement is observed for $E_T < 100$ GeV over the central ($|\eta| < 1$) and forward ($2 < |\eta| < 3$) pseudo–rapidity regions. The agreement is marginal in the IC region ($1 < |\eta| < 2$), which is the most poorly instrumented and least understood part of the calorimeter system. Above 100 GeV, the data is systematically high with respect to the theory and the difference grows linearly as a function of jet E_T. This trend is observed in all the measured η regions. Work on refining the jet energy scale is still in progress and this may result in a different energy correction, especially for $E_T > 100$ GeV. Due to the large errors of the measurements, greater than 30%, it is not possible at the moment to extract any information that favors any particular PDF set. A better understanding of the systematics associated with the measurement is needed to narrow down the uncertainty band. This would eventually allow to rule out some PDF sets, accomplish a better test of QCD and establish a lower limit in the quark compositeness scale.

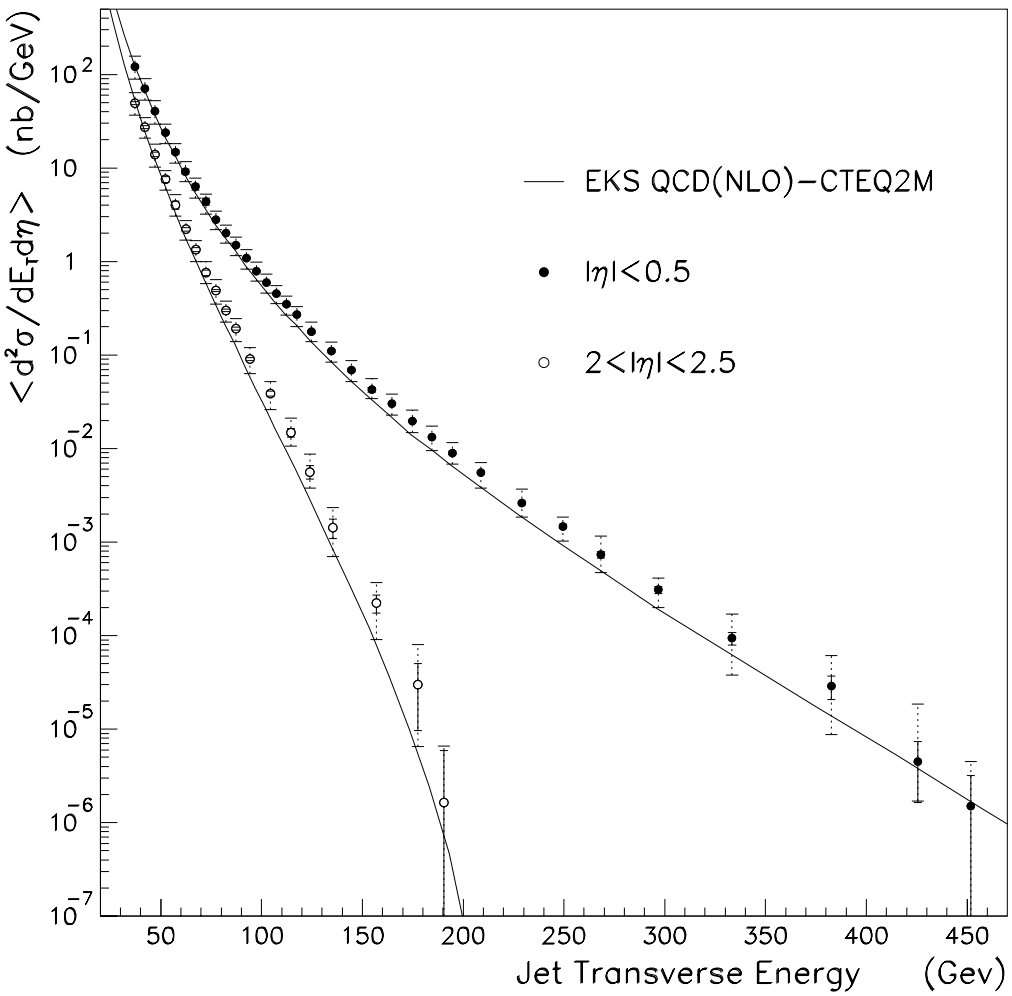

Figure 7.6: DØ inclusive jet cross sections as a function of the jet E_T compared with EKS QCD(NLO) predictions using CTEQ2M distribution functions.

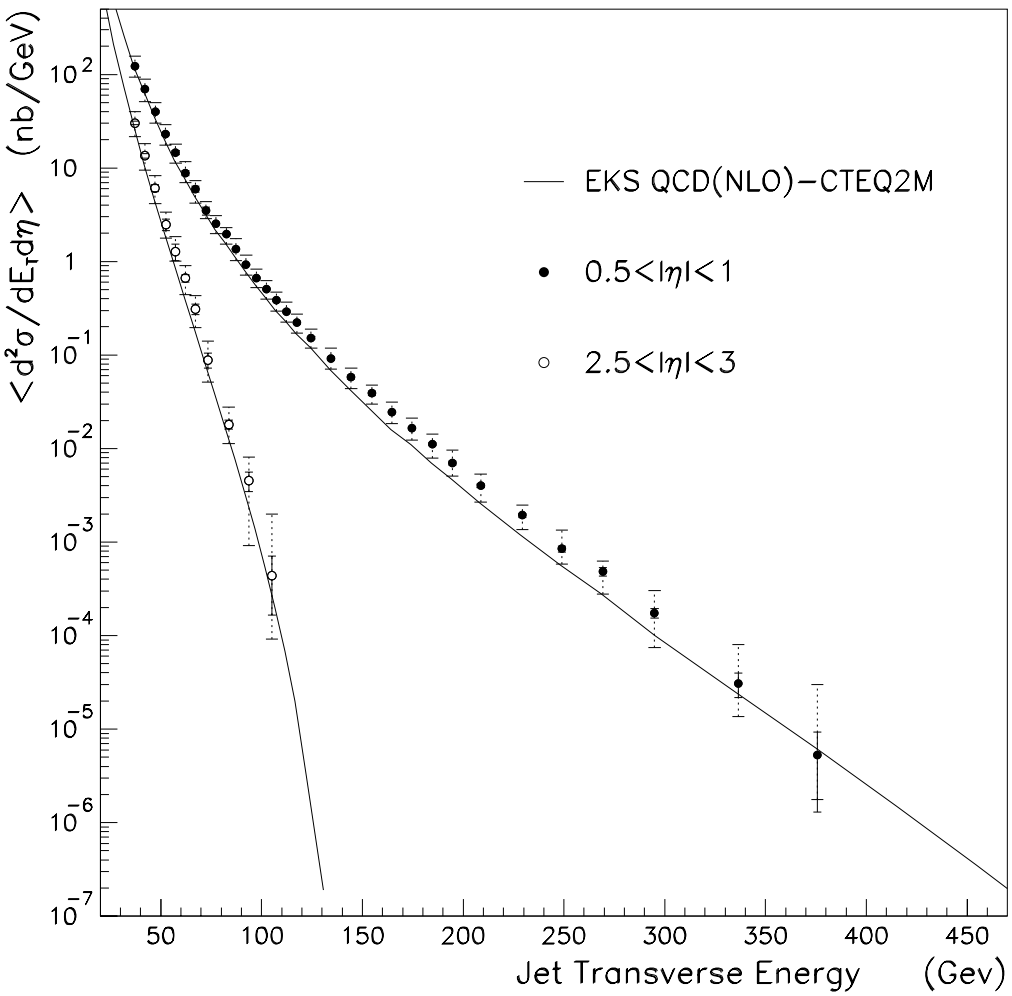

Figure 7.7: DØ inclusive jet cross sections as a function of the jet E_T compared with EKS QCD(NLO) predictions using CTEQ2M distribution functions.

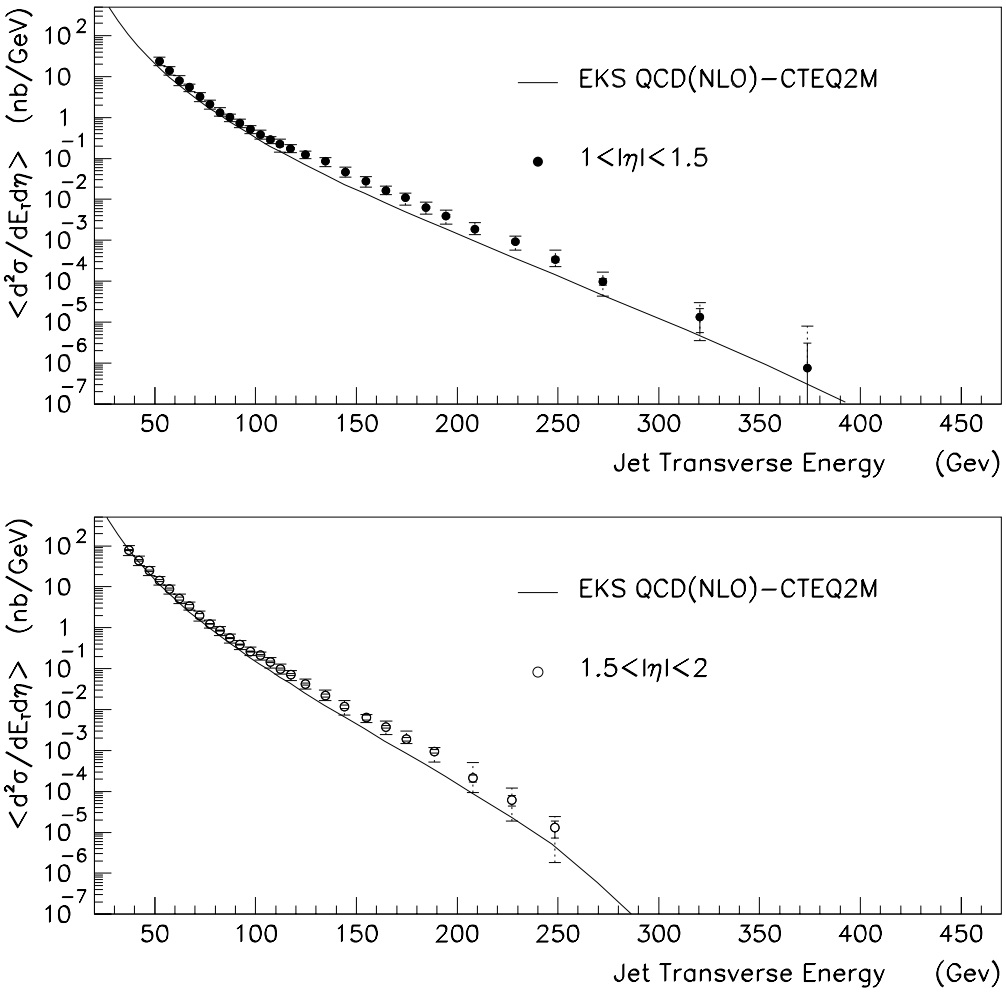

Figure 7.8: DØ inclusive jet cross sections as a function of the jet E_T compared with EKS QCD(NLO) predictions using CTEQ2M distribution functions.

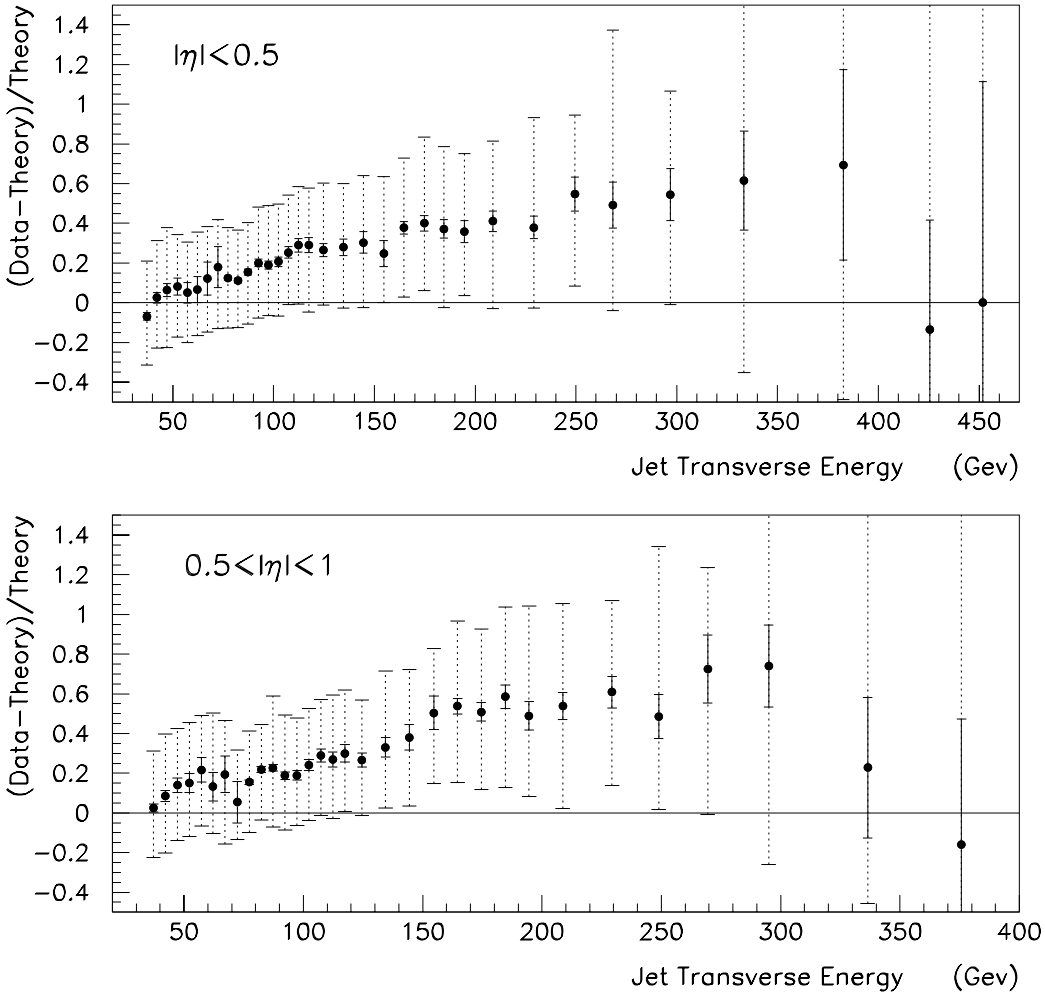

Figure 7.9: Ratios between DØ inclusive jet cross sections and EKS QCD(NLO) predictions using CTEQ2M distribution functions.

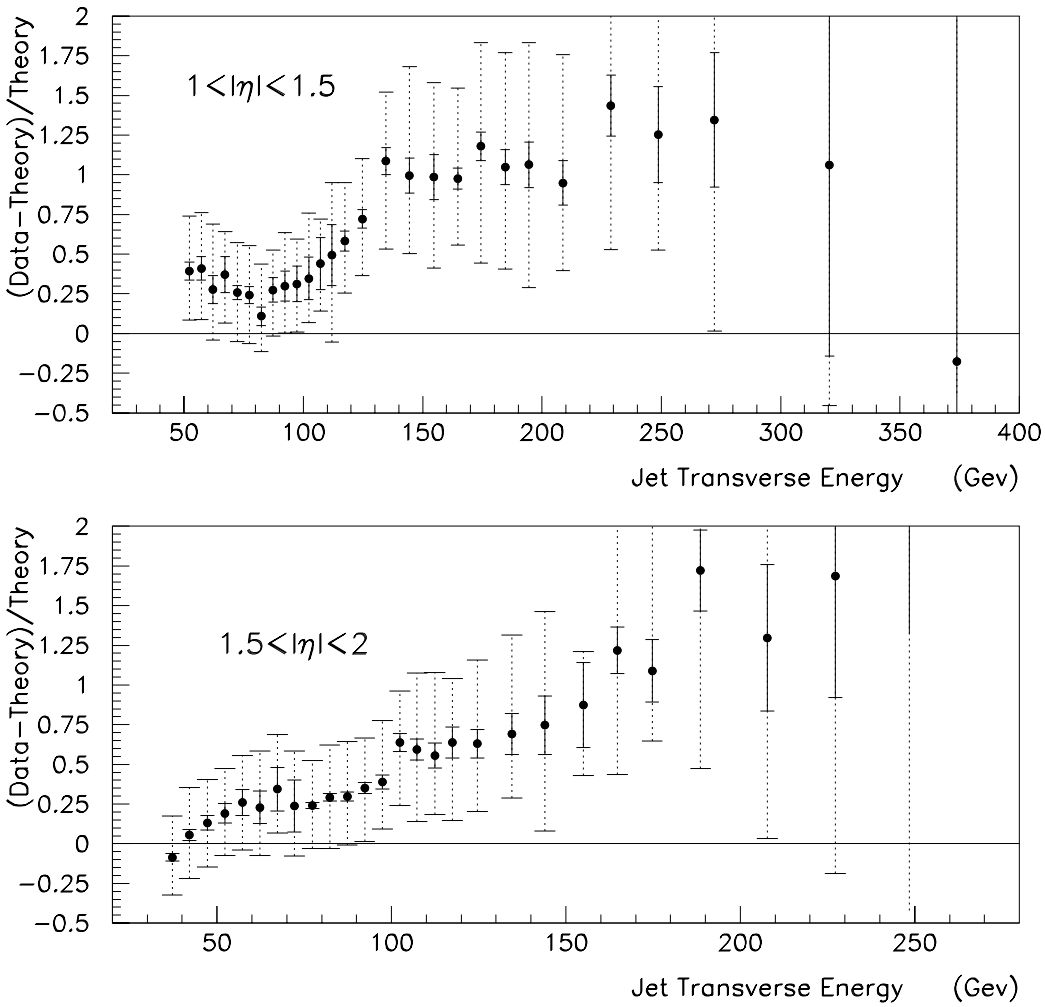

Figure 7.10: Ratios between DØ inclusive jet cross sections and EKS QCD(NLO) predictions using CTEQ2M distribution functions.

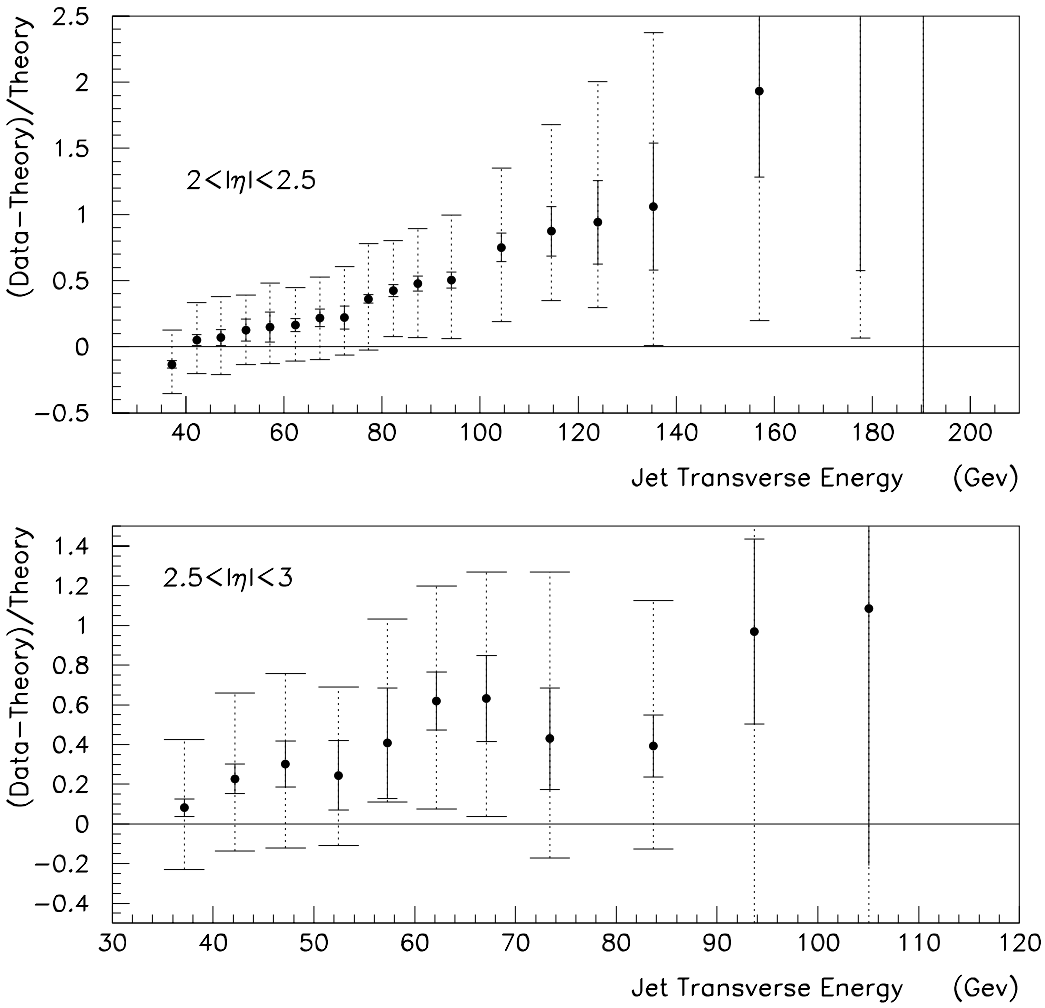

Figure 7.11: Ratios between DØ inclusive jet cross sections and EKS QCD(NLO) predictions using CTEQ2M distribution functions.

Bibliography

[1] "The Eightfold Way", M. Gell–Mann and Y. Ne'eman, New York: Benjamin, 1964.

[2] O.W.Greenberg, Am. J. Phys. 50 , 1074 (1982).

[3] J.J.Aubert et al., Phys. Rev. Lett. 33 , 1404 (1974).

[4] J.E.Augustin et al., Phys. Rev. Lett. 33 , 1406 (1974).

[5] S.W.Herb et al., Phys. Rev. Lett. 39 , 252 (1978).

[6] S.Weinberg, Phys. Rev. Lett. 19 , 1264 (1967).

[7] G.Arnison et al., Phys. Lett. 122B , 103 (1983).

[8] G.Arnison et al., Phys. Lett. 126B , 398 (1983).

[9] "Collider Physics", V.D.Barger and R.J.Philips, Frontiers in Physics (Lecture Note Series), 1987.

[10] "Introduction to Elementary Particles", D.Griffiths, John Wiley & Sons inc., 1987.

[11] "Quarks and Leptons: An Introductory Course in Modern Particle Physics", F.Halzen and A. Martin, John Wiley & Sons inc., 1984.

[12] "Introduction to High Energy Physics", D.H. Perkins, Addison Wesley, 1987.

[13] The CDF Collaboration, "Evidence for Top Quark Production in $p\overline{p}$ Collisions at $\sqrt{s} = 1.8\ TeV$", Phys. Rev. Lett., 73, 225, (1994).

[14] "Jet Production in Hadronic Collisions", L.DiLella, Ann. Rev. Nucl. Prt. Sci., 1985. $35 : 107 - 34$.

[15] B.Alper et al. Phys. Lett. B 44 , 521 (1973).

[16] M.Banner et al. Phys. Lett. B 44 , 537 (1973).

[17] F.Büsser et al. Phys. Lett. B 46 , 471 (1973).

[18] C.DeMarzo et al., Nucl. Phys. B 211 , 375 (1983).

[19] B.Brown et al., Phys. Rev. Lett. 49 , 711 (1982).

[20] M.Banner et al., Phys. Lett. B 118 , 203 (1982).

[21] G.Arnison et al., Phys. Lett. B 123 115 (1983).

[22] P.Bagnaia et al., Phys. Lett. B 138 430 (1984).

[23] J.Alitti et al., Phys. Lett. B 257 232 (1991).

[24] F.Abe et al., Phys. Rev. Lett. 62,613 (1989).

[25] F.Abe et al., Phys. Rev. Lett. 68, 1104 (1992).

[26] H.Plothow–Besch/CERN–PPE, 1993.08.30.

[27] A.Martin,R.Roberts,W.Stirling, Phys, Rev. D 43 , 3648 (1991).

[28] James Botts et al., Phys. Lett. B 304 159, (1993).

[29] "Jets and Kinematics", A.Baden and N.Hadley, DØ internal publication ♯957, 1990.

[30] R.Ellis and J.Sexton, Nucl. Phys. B 269 , 445 (1986).

[31] "Next–to–Leading Order Calculations in Jet Physics", W.Giele,E.Glover, Fermilab–Conf–92/213–T, August 4, 1992.

[32] W.Giele, E.Glover and D.Kosower, Nucl. Phys. B, 403 , 633 (1993).

[33] "Higher Order Corrections to Jet Cross Sections in e^+e^- Annihilation", W.Giele and E.Glover, Fermilab–Pub–91/100–T.

[34] E.Eichten, K.Lane and M.Peskin, Phys. Rev. Lett. 50 , 811 (1983).

[35] Focus on Fermilab, Fermilab, published by The Public Information Office, 1991.

[36] Design Report Tevatron I Project, Fermi National Accelerator Laboratory, 1984.

[37] The DØ Collaboration, "The DØ Detector", Nucl. Instr. and Methods **A 338** issue 2/3, 185–253 (1994).

[38] "Hadron and Electron Response of Uranium/Liquid Argon Calorimeter Modules for the DØ Detector", the DØ calorimeter group, Nucl. Inst. and Methods in physics Research A280, (1989).

[39] Private communication from Jeff Bantly.

[40] "The Level 0 Trigger for the DØ Detector", J. Bantly et al., submited to IEEE, Trans-Nuc-FCI, 30th Nov. 1993.

[41] "The DØ calorimeter Trigger", Jan Guida for the DØ collaboration, Fermilab-Conf-92/370, December 1992.

[42] M. Goosens et al., CERN Library Program $\sharp Q100$, Nov. 1991.

[43] Private comunication from Chris Klopfenstein.

[44] "Cone Algorithm For Jet Finding", N.J. Hadley, DØ internal publication $\sharp$904, November 29,1989.

[45] "Successive Combination Jet Algorithm for Hadron Collisions", S.D. Ellis and D.E. Soper, CERN–6860/93, April 1993.

[46] "The κ_T–clustering algorithm for jets in deep inelastic scattering and hadron collisions", S. Catani, Yu.L. Dokshitzer and B.R. Webber, Phys. Lett. B 285 (1992) 291 – 299.

[47] "Jet Size", N.J. Hadley, DØ internal publication $\sharp$1037, October 16, 1990.

[48] "One–Jet Inclusive Cross Section at Order α_s^3. Gluons Only", S.D.Ellis, Z.Kunszt, D.Soper, Phys. Rev. D, 40, 2188, (1989).

[49] 'One–Jet Inclusive Cross Section at Order α_s^3. Quarks and Gluons", S.D.Ellis, Z.Kunszt, D.Soper, Phys. Rev. Lett., 64, 2121, (1990).

[50] "A Study of Jet Merging and Splitting", K. Streets and Hadley, DØ internal publication $\sharp$1472, 1992.

[51] Private comunication from Rich Astur.

[52] "A Study of the Ability of the DØ Detector to Measure the Single Jet Inclusive Cross–Section", Phd. Thesis by Rich Astur, (1992).

[53] "Dijet Angular Distributions at $\sqrt{s} = 1800$ GeV using the DØ Detector", Phd. Thesis by Andy Milder, (1993).

[54] F. Paige, S. Protopopescu, ISAJET, BNL–31987.

[55] G.Marchesini and B.R.Webber, Nucl. Phys. B 310 (1988).

[56] R.Field and R.Feynman, Nucl. Phys. B 136, 1 (1978).

[57] R.Brun and F.Carminati, "GEANT Detector Description and Simulation Tool", CERN Program Library Long Writeup $W5013$ (1993)

[58] "The DØ Shower Library- Version 2.0", W. Dharmaratna, R. Raja, C. Stewart, DØ internal publication ♯1730, 1993.

[59] "Shower Libraries for DØ GEANT Monte Carlo", W. Womersley, R. Raja, A. Jonckheere, DØ internal publication ♯650, 1987.

[60] "PJET–Parton Jets in the Monte Carlo", Boaz Klima and Chip Stewart, DØ internal publication ♯905, 1989.

[61] "Optimization of Energy Resolution and Response of the DØ Detector", Phd. Thesis by John Borders, (1994).

[62] N.A. Amos et al., Phys. Lett. 243B , 158 (1990).

[63] F. Abe et al., "Measurement of Small Angle $p\overline{p}$ Elastic Scattering at $\sqrt{s} =$ 546 and 1800 GeV", FERMILAB-Pub-93/232-E (1993), submitted to Phys Rev D.

[64] F. Abe et al., "Measurement of $p\overline{p}$ Single Diffractive Dissociation at $\sqrt{s}$ = 546 and 1800 GeV", FERMILAB-Pub-93/233-E (1993), submitted to Phys Rev D.

[65] F. Abe et al., "Measurement of the $p\overline{p}$ Total Cross Section at $\sqrt{s} = 546$ and 1800 GeV", FERMILAB-Pub-93/234-E (1993), submitted to Phys Rev D.

[66] "Main Ring Deadtime", John Butler, DØ internal publication ♯682, February 28,1993.

[67] "Luminosity Calculations for DØ", N.Amos et al., DØ internal publication ♯2031, January,1994.

[68] Richard V. Astur, "Study of Fake Jets in the DØ Detector", DØ internal publication ♯ 1662, March 20, 1993.

[69] Brad Abbot and J. Blazey, "Effects of Hot Cells on the Inclusive Jet Cross Sections", DØ internal publication ♯ 1845, September 9, 1993.

[70] V.D.Elvira, "Contamination in QDC-MDST Files Version 10", DØ internal publication ♯ 2058, February 17, 1994.

[71] G. Dissertori and J. Blazey, "Results of a Scanning of Events with High E_T Jets from the Inclusive Jet Analysis", DØ internal publication ♯ 1817, July 19, 1993.

[72] Private comunication from J.Blazey.

[73] R.Astur and A.Milder, "Jet Trigger Efficiency in the DØ Detector", DØ internal publication ♯ 1663, March 8, 1993.

[74] V.D.Elvira, J.Blazey and R.Astur, "A Study of Standard Jet Cuts and their Efficiencies Using DØ Collider Data", DØ internal publication ♯ 1763, June 21, 1993.

[75] M.Bhattacharjee, V.D.Elvira and J.Blazey, "Efficiencies of the Standard Jet Cuts for cone sizes: 0.3, 0.5,0.7", DØ internal publication ♯ 2197, July 15, 1994.

[76] "A Search for Squarks and Gluinos in $p\overline{p}$ Collisions at $\sqrt{1.8}$ TeV with the DØ Detector", Phd. Thesis by Marc Paterno, (1994).

[77] F.Abe et al., Phys. Rev. Lett. 69, 2896 (1992).

[78] B.Kehoe, "Resolution Bias in Jet Response Measurement", DØ internal publication ♯ 2052, February 8, 1994.

[79] V.D.Elvira, "Jet η bias and Resolution", DØ internal publication ♯ 2173, June 8, 1994.

[80] Private comunication from Bob Hirosky.

[81] Brad Abbott for the DØ collaboration, "Measurement of Jet Shapes in $p\overline{p}$ Collisions at DØ", 8th Meeting of the Division of Particles and Fields of the American Physical Society, Albuquerque, New Mexico, August $2-6$, 1994.

[82] D.May and J.Blazey, "The Dependence of Jet Energy Scale on Fragmentation Functions" DØ internal publication ♯ 1173, August 8, 1991.

[83] Private comunication from Freedy Nang.